# A path integral Monte Carlo method for obtaining thermodynamic properties of nonadiabatic systems

by

Neil George Raymond

A thesis
presented to the University of Waterloo
in fulfillment of the
thesis requirement for the degree of
Master of Science
in
Chemistry

Waterloo, Ontario, Canada, 2017

I hereby declare that I am the sole author of this thesis. This is a true copy of the thesis, including any required final revisions, as accepted by my examiners. I understand that my thesis may be made electronically available to the public.

# Abstract

The calculation of thermochemical properties is an important goal of quantum chemistry. Calculation techniques are well established for stable molecules. They are used routinely to calculate Gibbs energy ($G$) for stable isomers, Gibbs energy difference ($\Delta G$) for reactions and also to obtain activation energies in the context of transition state theory. Practical calculations use harmonic oscillator (H.O.), Rigid Rotor (RR) and ideal gas approximations to obtain thermodynamic contributions. This approach works well for many systems, but breaks down for systems with multiple low-lying electronic states. Examples of such systems are found among radicals, systems containing transition metal atoms, and open-shell states when spin-orbit coupling is considered. Systems of this type are better described by vibronic models acting through a small manifold of electronic states.

In this work we describe a path integral Monte Carlo (PIMC) approach that, for vibronic models, will obtain the partition function ($Z$) and thermodynamic properties as a function of temperature. Investigation of model systems demonstrates that the partition function and internal energy can be obtained in an efficient manner.

# Acknowledgements

I would like to thank my supervisors Dr. Marcel Nooijen and Dr. Pierre-Nicholas Roy for their support and encouragement. Their open door policy and availability has been extremely helpful. I am grateful for the opportunities they have provided to me. They have helped me challenge myself and push my limits.

My appreciation is due to the research group as a whole for making my academic experience extremely enjoyable and motivating me to come to the office every day. I am thankful for and amazed at the patience of Dmitri Iouchtchenko who providied guidance and support during my Master's, as well as answering my multitude of questions.

I would also like to thank my committee members, Dr. Scott Hopkins and Dr. Roger Melko, for taking the time to read my thesis and attend my presentation.

# Dedication

To my parents: all of my achievements are their achievements.

# Table of Contents

# List of Figures

# List of Tables

# List of Abbreviations

**BO** Born-Oppenheimer. 3, 5

$C_v$ heat capacity. 7, 15, 17, 18, 21, 22

**DNA** deoxyribonucleic acid. 5

**DoF** Degrees of Freedom. 5, 7, 8, 13, 27, 94

$G$ Gibbs energy. iii, 2, 3

**GPU** Graphics Processing Unit. 94

**H.O.** harmonic oscillator. iii, vi, vii, 3, 5, 27, 44, 57, 66, 78, 102, 103

$k$ rate constant. 3

$K_{eq}$ equilibrium constant. 3

**PDF** probability density function. 10–13

**PES** potential energy surface. vii, 3–6, 19, 20, 23, 40, 57, 61, 94

**PI** path integral. 6–8, 11, 13, 15, 27, 94

**PIMC** path integral Monte Carlo. iii, 6, 14, 16–21, 23, 27, 32, 44, 49, 61, 66, 78, 83, 93, 94

**QM** Quantum Mechanical. 1, 2, 6

**RR** Rigid Rotor. iii, 3, 5

**SE** Schrodinger Equation. 3

**SOS** sum-over-states. 19, 21, 27, 44, 61, 78, 94

$U$ internal energy. 7, 11, 15–18, 20, 32, 49, 61, 66, 93

$Z$ partition function. iii, 1, 3, 7–9, 11–13, 15–18, 20, 21, 32, 49, 66, 93

# Chapter 1

# Introduction

## 1.1 Motivation

Determining the properties of Quantum Mechanical (QM) systems is well understood in theory

1. Express the Hamiltonian ($\hat{H}$) of a system in its eigenbasis $\Psi$

$$\hat{H}\Psi = \boldsymbol{E}\Psi \tag{1.1}$$

2. Calculate the partition function ($Z$) by tracing over the eigenvalues $E_i$

$$Z = \sum_i e^{-\beta E_i} \tag{1.2}$$

The macroscopic properties of a QM system can be expressed in terms of the partition function ($Z$). The microscopic properties of a QM system can be expressed in terms of the system's eigenvalues [1, p. 693]. In practice, however, calculating these functions is impossible for sizable systems.

> "Consider for example mapping the PES by calculating $E_e$ for every $0.1$ Å over say a $1$ Å range (a very coarse mapping). With three atoms there are three internal coordinates, giving $10^3$ points to be calculated. Already four atoms produces six internal coordinates, giving $10^6$ points, which only can be done by a very determined effort. Larger systems are out of reach. Constructing global PESs for all but the smallest molecules is thus impossible." ([2, p. 4])

The space necessary to store a Hamiltonian for QM systems of interest grows exponentially proportional to the number of modes as showen in Figure 1.1. This mathematical constraint is commonly referred to as the *curse of dimensionality*.

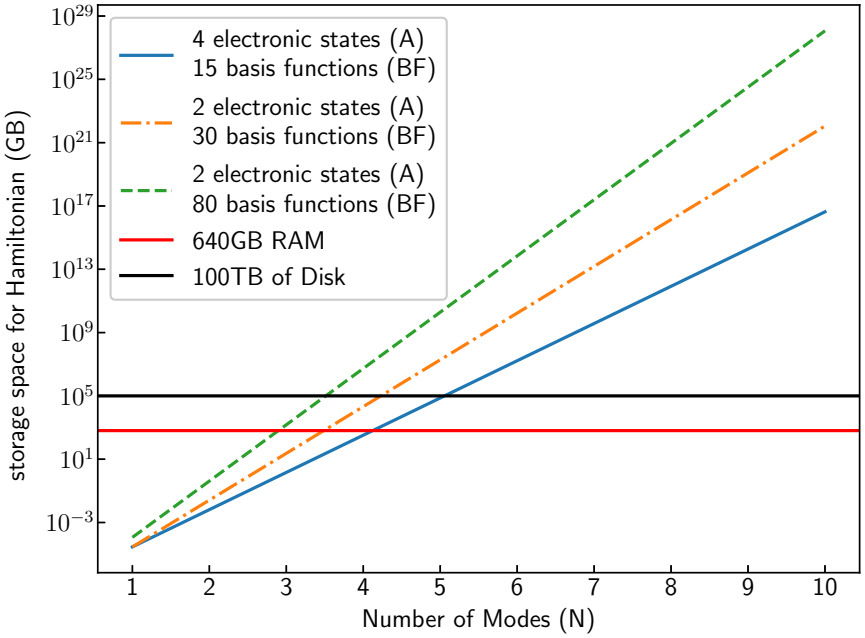


Figure 1.1: Storage requirement of Hamiltonian for SOS

If one is interested in solving practical systems, it is clear that there is a need for a more efficient approach. There is a real-world need to calculate properties of physical materials and systems, on human time scales and with an everyday amount of computational power. *Computational chemistry* is the study of practical computation of just this type of problem. Efficient computation of chemical properties can provide researchers with data from which they can gain insight and understand the behaviour of a large class of molecules and systems. A key aspect of computational chemistry is validating the use of a method for a particular system or model. The choice of a method may depend on the properties to be calculated. The choice of computational methods, must therefore be examined with respect to the desired properties.

## 1.2 Macroscopic properties

We are interested in calculating macroscopic properties of QM systems in thermal equilibrium. In particular, we would like to accurately calculate the Gibbs energy ($G$), a thermodynamic potential that is minimized when a system under constant pressure and temperature reaches chemical

equilibrium. From $G$ a number of system properties such as equilibrium constants ($K_{eq}$), and rate constants ($k$) can be obtained. Understanding $G$ and reaction pathways is important in a diverse range of fields such as the petrochemical industry [3], synthetic chemistry [4], and hydrogen energy storage [5].

The Gibbs energy difference ($\Delta G$) determines the preference of reaction pathways due to their spontaneity and therefore it determines the feasibility of prospective catalysts. Reaction pathway preference and speed are important in the research and development of high-tech materials for products such as solar cells, catalysts, and batteries. The development of alternative catalysts is important because of the scarcity of rare metal complexes commonly used as catalysts, as well as their unwanted byproducts [6, 7].

## 1.3 Nonadiabatic systems

In theory, macroscopic properties can be obtained by solving the Schrodinger Equation (SE) eq. (1.1) and directly calculating $Z$. This approach is not feasible in practice. Several approximations have been employed to overcome this difficulty: Born-Oppenheimer (BO), harmonic oscillator (H.O.), Rigid Rotor (RR), and ideal gas approximation. These are standard approaches to thermochemistry and are widely used because they are very accurate in describing single surface systems.

The standard approach breaks down when there are multiple low-lying electronic states that are very close in energy. Consider the example in Figure 1.2, which shows two close-lying states that can be fairly well approximated by harmonic oscillators. Approximating these surfaces using only harmonic oscillators may be a reasonable approximation in the case of Figure 1.2, but a more accurate and flexible method is desirable. Our systems of interest are more complex, having multiple surfaces with large anharmonicities. Systems that contain radicals

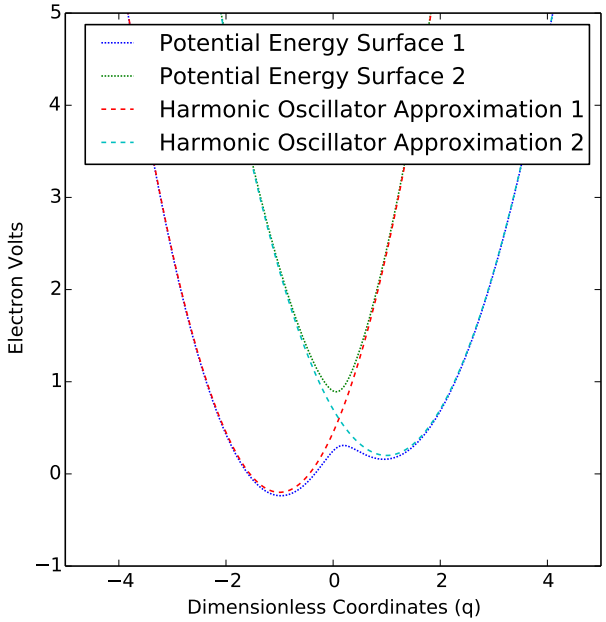

Figure 1.2: Approximating a PES with two H.O.s

and those containing transition metal atoms are two examples. In addition, these surfaces can be multidimensional and can interact, sometimes crossing, in many different planes [8]. This is evident from the system in Figure 1.3.

Figure 1.3 illustrates the complexity present in just a single subregion. Surfaces can have drastically different curvature, intersect other surfaces, and may be absent in our defined regions. The complexity of describing these surfaces with a computational model arises from the mixing of different electronic states as a result of small vibrations. This effect is called vibronic coupling, and models that describe such systems are thus called vibronic models. Modeling these complex potential energy surfaces (PESs) is commonly done within adiabatic or diabatic representations [9, p. 2].

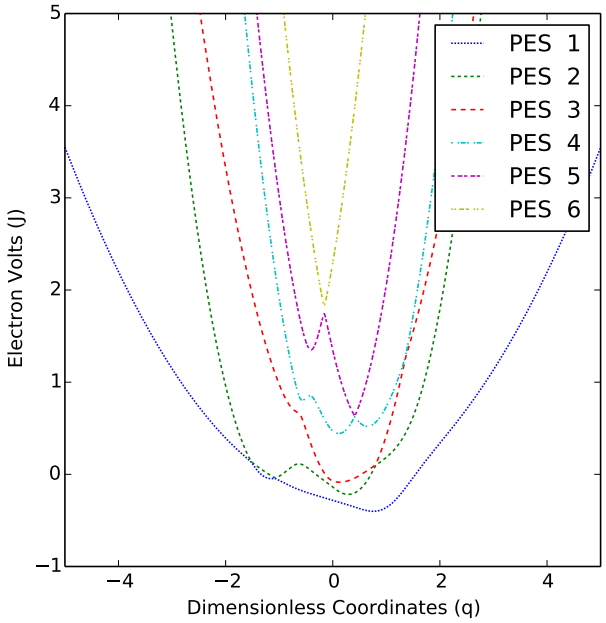


Figure 1.3: Representative PES

The general form of a system with two electronic surfaces ($a$) in the adiabatic representation is

$$\hat{H} = \begin{bmatrix} \hat{T}_{11} & \hat{T}_{12} \\ \hat{T}_{21} & \hat{T}_{22} \end{bmatrix} + \begin{bmatrix} U_{11}(\mathbf{R}) & U_{12}(\mathbf{R}) \\ U_{21}(\mathbf{R}) & U_{22}(\mathbf{R}) \end{bmatrix} \tag{1.3}$$

where $\mathbf{R}$ represents the nuclear positions. In eq. (1.3) $\underline{\boldsymbol{T}}$ is a dense matrix and $\underline{\boldsymbol{U}}$ is a matrix that is diagonal in the electronic surfaces. The off-diagonal components of $\underline{\boldsymbol{T}}$ are the vibronic coupling terms. In the adiabatic representation, calculation of these terms is computationally expensive. They are commonly treated as zero under the assumption that they are small enough to be neglected. In systems where surfaces are very close or intersect, this approximation is not valid.

An alternative representation is the diabatic representation whose general form is

$$\hat{H} = \begin{bmatrix} \hat{T}_{11} & \\ & \hat{T}_{22} \end{bmatrix} + \begin{bmatrix} U_{11}(\mathbf{R}) & U_{12}(\mathbf{R}) \\ U_{21}(\mathbf{R}) & U_{22}(\mathbf{R}) \end{bmatrix} \tag{1.4}$$

In eq. (1.4) $\underline{\boldsymbol{T}}$ is a matrix that is diagonal in the electronic surfaces, and $\underline{\boldsymbol{U}}$ is a dense matrix. In the diabatic representation, the off-diagonal components of $\underline{\boldsymbol{U}}$ are the vibronic coupling terms. The calculation of the vibronic coupling terms in the diabatic representation is preferable to those in the adiabatic representation for two reasons. First, in the adiabatic representation, the off-diagonal terms $\hat{T}_{12}$, $\hat{T}_{21}$ contain first and second derivatives in both the nuclear and electronic Degrees of Freedom (DoF), while in the diabatic representation these terms are zero. Second, the PES in the diabatic representation is smooth and is easily represented by a Taylor series, while the PES in the adiabatic representation can have irregularities, such as cusps, which pose numerical difficulties.

Systems with strong vibronic coupling are commonly termed nonadiabatic systems. The approximations in Figure 1.2 are not sufficient to describe nonadiabatic systems. Nonadiabatic systems and their effects are of interest in many different areas of science such as photo-chemistry, biology, quantum information processing, and electro-chemistry. For example, the primary photochemical event in human vision is the photoisomerization of retinal in the protein rhodopsin: this conformational change can only be described through nonadiabatic effects [10]. A second example, the stability of deoxyribonucleic acid (DNA) under ultraviolet photon bombardment, commonly from exposure to the sun, is also a nonadiabatic effect. After being electronically excited, DNA undergoes thermal relaxation; this nonadiabatic process does not emit photons, which would otherwise be harmful to surrounding DNA molecules [11]. Nonadiabatic effects can both promote and prevent photo-chemistry, and are important to the survival and propagation of life.

Vibronic models are widely used in computational studies. Most often they are used to model dynamical phenomena or spectroscopy. In this thesis we will use similar vibronic models, but our goal is to model thermal properties of systems with multiple low-lying electronic states. For our purpose, the use of quadratic potentials will be adequate to describe systems of interest. Because common approximations such as BO, H.O., and RR break down in nonadiabatic systems, other methods are required to obtain our desired macroscopic properties.

## 1.4 Path Integrals

Path integral (PI) methods are commonly used to investigate large systems or systems with complex PESs, such as protonated methane $CH_5^+$[12]. Recently there has been much interest in the application of PI methods to nonadiabatic systems[13–16]. PI methods involve discretizing the continuous quantum problem such that classical equations can be solved to obtain exact QM properties in the limit of infinite partitionings.

A natural extension of PI is path integral Monte Carlo (PIMC). Given some distribution $\varrho$ we can find the expectation value of a QM operator $\langle \hat{A} \rangle$ by sampling from the distribution $\varrho$. This process is straightforward if $\varrho$ is a simple distribution; however the distribution is not simple for most systems. In cases where sampling from $\varrho$ is computationally expensive, more intelligent approaches are required. A few examples include partial chain movement, importance sampling [17], and rejection sampling [18, 19]. Our methodology makes use of importance sampling, which will be discussed in further detail in Section 2.2.2. The use of PI methods allows us to study nonadiabatic systems otherwise considered too expensive to explore.

## 1.5 Scope & organization of the thesis

In this thesis we present a PIMC method for calculating thermodynamic properties. Our path integral Monte Carlo (PIMC) method can be applied to nonadiabatic systems possessing regions with well-defined neighbourhoods. In Chapter 2 we derive a PI expression for Z. We introduce the concept of importance sampling, and derive thermodynamic estimators using a finite difference approach. In Chapter 3, four model systems are used to test the limits of our PIMC method.

# Chapter 2

# Theory & Methods

Our overall goal is to obtain thermodynamic properties for nonadiabatic systems. In order to achieve this we will derive an expression for the partition function ($Z$), given a vibronic model describing these systems. The vibronic model used by our method is assumed to have been previously obtained from electronic structure calculations [20]. We do not further address these electronic structure calculations in this thesis.

We derive a path integral expression for the partition function in a product basis of nuclear and electronic Degrees of Freedom (DoF). Acting with our Hamiltonian is computationally prohibitive, so we use the Trotter theorem [21] to factorize our Hamiltonian into two partitions $\hat{h}_o$ and $\hat{V}$. Directly evaluating the integrals in our PI expression is computational expensive for sizeable systems; to overcome this we approximate these integrals using a statistical technique, Monte Carlo Integration [22]. The mathematical forms we used to calculate the path integral are described later in this thesis. Estimators for the internal energy ($U$) and heat capacity ($C_v$) will also be derived.

## 2.1 Path Integral formulation

The canonical partition function is obtained from the trace of the Boltzmann operator

$$Z = \mathrm{Tr}\left[e^{-\beta\hat{H}}\right] \tag{2.1}$$

where $\beta = (k_B T)^{-1}$ is the reciprocal temperature and the trace is taken over the states that span the electronic and nuclear DoF. We define $N$ to be the number of nuclear DoF. The resolution of the identity for this space can be expressed as

$$\boldsymbol{I} = \int \mathrm{d}\mathbf{R} \sum_{a=1}^{A} |\mathbf{R}, a\rangle \langle \mathbf{R}, a| \tag{2.2}$$

where $\mathbf{R}$ is a vector of length $N$ representing the nuclear positions, and $a$ represents the electronic surfaces. Repeated insertion of this completeness relation yields a PI discretization of $Z$ [1]

$$Z = \int \mathrm{d}\mathbf{R}^P \sum_{\mathbf{a}}^{A} \prod_{i=1}^{P} \langle \mathbf{R}_i, a_i | \, e^{-\tau \hat{H}} \, |\mathbf{R}_{i+1}, a_{i+1}\rangle \tag{2.3}$$

where $P$ is the number of imaginary time-slices, also known as "beads", and $\tau = \beta/P$.
We make use of the compact notation

$$\sum_{\mathbf{a}}^{A} = \sum_{a_1=1}^{A} \sum_{a_2=1}^{A} \cdots \sum_{a_P=1}^{A} \tag{2.4}$$

and

$$\int \mathrm{d}\mathbf{R}^P = \int \mathrm{d}\mathbf{R}_1 \int \mathrm{d}\mathbf{R}_2 \cdots \int \mathrm{d}\mathbf{R}_P \tag{2.5}$$

### 2.1.1 Structure of Hamiltonian

The structure of a vibronic Hamiltonian in the diabatic representation is

$$\hat{H} = \hat{T} + \hat{U} \tag{2.6}$$

We partition our Hamiltonian operator into a harmonic operator $\hat{h}_o$ and a coupling operator $\hat{V}$:

$$\hat{H} = \hat{h}_o + \hat{V} \tag{2.7}$$

[1] For the derivation of the path integral discretization of the partition function, see Appendix A.

We define $\hat{V}^{ho}$ through its matrix representation, which is diagonal in the electronic surfaces and can be modeled by harmonic oscillators.

$$V^{ho}_{aa'} = U^{ho}_{aa'}\delta_{aa'} \tag{2.8}$$

We define the harmonic operator $\hat{h}_o$ as all terms in $\hat{H}$ that can be modeled by harmonic oscillators. Note the exact composition of $\hat{h}_o$ is flexible, based on the form of the harmonic oscillators, allowing for optimizations to specific implementations.

$$\hat{h}_o = \hat{T}\mathbb{1} + \hat{V}^{ho} \tag{2.9}$$

By construction $\hat{h}_o$ is diagonal in the electronic surfaces $a$.

$$\langle \mathbf{R}, a|\hat{h}_o|\mathbf{R}^{'}, a'\rangle = \langle \mathbf{R}, a|\hat{h}_o|\mathbf{R}^{'}, a\rangle\, \delta_{a,a'} \tag{2.10}$$

We define the coupling operator $\hat{V}$ as the remaining components of $\hat{U}$.

$$\hat{V} = \hat{U} - \hat{V}^{ho} \tag{2.11}$$

By construction $\hat{V}$ is diagonal in the nuclear positions $\mathbf{R}$.

$$\langle \mathbf{R}, a|\hat{V}|\mathbf{R}^{'}, a'\rangle = \langle \mathbf{R}, a|\hat{V}|\mathbf{R}, a'\rangle\, \delta(\mathbf{R} - \mathbf{R}^{'}) \tag{2.12}$$

Next we use the Trotter theorem to factorize our Hamiltonian into $\hat{h}_o$ and $\hat{V}$ [21].

### 2.1.2 Trotter factorization

Inserting our Hamiltonian from eq. (2.7) into our expression for $Z$ from eq. (2.3)

$$Z = \int \mathrm{d}\mathbf{R}^P \sum_{\mathbf{a}}^{A} \prod_{i=1}^{P} \langle \mathbf{R}_i, a_i|\, e^{-\tau\left(\hat{h}_o + \hat{V}\right)} \left|\mathbf{R}_{i+1}, a_{i+1}\right\rangle \tag{2.13}$$

We choose a symmetric splitting of the Hamiltonian:

$$Z = \lim_{P\to\infty} \int \mathrm{d}\mathbf{R}^P \sum_{\mathbf{a}}^{A} \prod_{i=1}^{P} \langle \mathbf{R}_i, a_i | \, e^{-\frac{\tau}{2}\hat{h}_o} e^{-\tau\hat{V}} e^{-\frac{\tau}{2}\hat{h}_o} \left| \mathbf{R}_{i+1}, a_{i+1} \right\rangle \tag{2.14}$$

Applying the symmetric Trotter factorization gives us: [23] [2]

$$Z = \lim_{P\to\infty} \int \mathrm{d}\mathbf{R}^P \sum_{\mathbf{a}}^{A} \prod_{i=1}^{P} \langle \mathbf{R}_i, a_i | \, e^{-\tau\hat{h}_o} \left| \mathbf{R}_{i+1}, a_i \right\rangle \left\langle \mathbf{R}_{i+1}, a_i \right| e^{-\tau\hat{V}} \left| \mathbf{R}_{i+1}, a_{i+1} \right\rangle \tag{2.15}$$

We can clearly see that the harmonic operator $\hat{h}_o$ links different nuclear positions $\mathbf{R}$, and the coupling operator $\hat{V}$ links different electronic surfaces $a$. By factoring our Hamiltonian we can evaluate the harmonic operator $\hat{h}_o$ independently of the coupling operator $\hat{V}$. We will show later that this can be done analytically.

Note that a finite choice of $P$ results in a systematic error in the Trotter approximation. For readability, we suppress this approximation for the remainder of this thesis as follows:

$$Z = \int \mathrm{d}\mathbf{R}^P \sum_{\mathbf{a}}^{A} \prod_{i=1}^{P} \langle \mathbf{R}_i, a_i | \, e^{-\tau\hat{h}_o} \left| \mathbf{R}_{i+1}, a_i \right\rangle \left\langle \mathbf{R}_{i+1}, a_i \right| e^{-\tau\hat{V}} \left| \mathbf{R}_{i+1}, a_{i+1} \right\rangle \tag{2.16}$$

As our calculations use finite values for $P$, this error is present in all of the work that follows. This approximation is acceptable because the error becomes negligble for sufficiently large $P$ values. Additionally we define $g(\mathbf{R})$ as the probability density function (PDF) for our system:

$$g(\mathbf{R}) = \sum_{\mathbf{a}}^{A} \prod_{i=1}^{P} \langle \mathbf{R}_i, a_i | \, e^{-\tau\hat{h}_o} \left| \mathbf{R}_{i+1}, a_i \right\rangle \left\langle \mathbf{R}_{i+1}, a_i \right| e^{-\tau\hat{V}} \left| \mathbf{R}_{i+1}, a_{i+1} \right\rangle \tag{2.17}$$

such that

$$Z = \int \mathrm{d}\mathbf{R}^P \, g(\mathbf{R}) \tag{2.18}$$

[2] For the derivation of the Trotter factorization, see Appendix B.

## 2.2 Evaluating the partition function

We have derived a general PI expression for $Z$ in nuclear coordinates $\mathbf{R}$ and electronic surfaces $a$. However we don't want to directly evaluate the integrals over $\mathbf{R}$ due to the computational cost; we will use a stochastic method, Monte Carlo Integration, to approximate the integral.

### 2.2.1 Monte Carlo Integration

For a continuous random variable $X$ having a probability density function (PDF), $p(x)$, the expected value of a function $f(x)$ is:

$$\Big\langle f(x) \Big\rangle_p = \frac{\int p(x) f(x)\,\mathrm{d}x}{\int p(x)\,\mathrm{d}x} \tag{2.19}$$

We define a Monte Carlo estimator as the mean of $f(x)$ over $N$ samples from $p(x)$, $(x_1, \ldots, x_N)$.

$$\tilde{f}(x) = \frac{1}{N} \sum_{i=1}^{N} f(x_i) \tag{2.20}$$

This ratio of integrals can be approximated using the Central Limit Theorem [24, pp. 278-281]

$$\frac{\int p(x) f(x)\,\mathrm{d}x}{\int p(x)\,\mathrm{d}x} = \frac{1}{N} \sum_{i=1}^{N} f(x_i) \pm \left(\frac{\sigma^2}{N}\right)^{\frac{1}{2}} \tag{2.21}$$

$$\Big\langle f(x) \Big\rangle_p = \lim_{N\to\infty} \frac{1}{N} \sum_{i=1}^{N} f(x_i) \tag{2.22}$$

Note that the second term in eq. (2.21) is inversely proportional to $\sqrt{N}$. Therefore to obtain an effective estimate, a small variance $\sigma^2$ or a large sample size is required. A reduction in the variance of a sample distribution is computationally advantageous as smaller sample sizes result in shorter run times.

Using Monte Carlo Integration we can obtain properties of our system, such as $U$:

$$\Big\langle U(\mathbf{R}) \Big\rangle_g = \frac{\int \mathrm{d}\mathbf{R}^P\, g\left(\mathbf{R}\right) U(\mathbf{R})}{\int \mathrm{d}\mathbf{R}^P\, g\left(\mathbf{R}\right)} \approx \frac{1}{N} \sum_{i=1}^{N} U(\mathbf{R}_i) \tag{2.23}$$

However we are not yet able to obtain $Z$ without directly evaluating the integrals. Importance sampling will allow us to calculate $Z$ and reduce our variance.

### 2.2.2 Importance sampling

Importance sampling is a statistical method that can reduce the variance $\sigma^2$ of sampling. Certain values of the input random variables in a simulation have more impact on the parameters being estimated than others. If these *important contributions* are emphasized by sampling more frequently, then the estimator variance is reduced. The principle of importance sampling is that sampling from a new distribution $\varrho$ is equivalent to sampling with weight $\frac{\varrho}{g}$ from our original distribution $g$, biasing the sample obtained towards $g$ [24, pp. 284-286]. The reduction in variance leads to more efficient calculation of parameters of interest, since fewer samples are needed for convergence. In addition, we can choose the new distribution $\varrho$ so that it is more efficient to sample from.

We use importance sampling to define an expression for the partition function of the Hamiltonian of our system ($Z_H$) in terms of the distribution $\varrho$:

$$Z_H = \int \mathrm{d}\mathbf{R}^P \, g\left(\mathbf{R}\right) \tag{2.24}$$

$$Z_H = \int \mathrm{d}\mathbf{R}^P \, \varrho\left(\mathbf{R}\right) \frac{g\left(\mathbf{R}\right)}{\varrho\left(\mathbf{R}\right)} \tag{2.25}$$

$$\frac{Z_H}{\int \mathrm{d}\mathbf{R}^P \, \varrho\left(\mathbf{R}\right)} = \frac{\int \mathrm{d}\mathbf{R}^P \, \varrho\left(\mathbf{R}\right) \frac{g(\mathbf{R})}{\varrho(\mathbf{R})}}{\int \mathrm{d}\mathbf{R}^P \, \varrho\left(\mathbf{R}\right)} \tag{2.26}$$

$$\frac{Z_H}{\int \mathrm{d}\mathbf{R}^P \, \varrho\left(\mathbf{R}\right)} = \left\langle \frac{g\left(\mathbf{R}\right)}{\varrho\left(\mathbf{R}\right)} \right\rangle_{\varrho} \tag{2.27}$$

$$Z_H = \left\langle \frac{g\left(\mathbf{R}\right)}{\varrho\left(\mathbf{R}\right)} \right\rangle_{\varrho} \left( \int \mathrm{d}\mathbf{R}^P \, \varrho\left(\mathbf{R}\right) \right) \tag{2.28}$$

We define the partition function of a system with the PDF $\varrho\left(\mathbf{R}\right)$:

$$Z_\varrho = \int \mathrm{d}\mathbf{R}^P \, \varrho\left(\mathbf{R}\right) \tag{2.29}$$

We define $Z_f$ as the estimate of the coupling contribution to $Z_H$

$$Z_f = \left\langle \frac{g\left(\mathbf{R}\right)}{\varrho\left(\mathbf{R}\right)} \right\rangle_{\varrho} \tag{2.30}$$

Resulting in a more compact representation for the partition function of our Hamiltonian

$$Z_H = Z_f Z_\varrho \tag{2.31}$$

We will show that our choice of the distribution $\varrho$ can be sampled without rejection and can be analytically evaluated. Calculating $Z_H$ is therefore the product of an estimator obtained using Monte Carlo Integration, $Z_f$, and an analytical term $Z_\varrho$. Next we will derive the matrix representations for $g(\mathbf{R})$ and $\varrho(\mathbf{R})$.

### 2.2.3 Propagator forms

Given our PI formulation of $Z$:

$$Z = \int \mathrm{d}\mathbf{R}^P \sum_{\mathbf{a}}^{A} \prod_{i=1}^{P} \langle \mathbf{R}_i, a_i | \, e^{-\tau \hat{h}_o} \left| \mathbf{R}_{i+1}, a_i \right\rangle \left\langle \mathbf{R}_{i+1}, a_i \right| e^{-\tau \hat{V}} \left| \mathbf{R}_{i+1}, a_{i+1} \right\rangle \tag{2.32}$$

We introduce the following notation for the matrix representation of the harmonic and coupling propagators. We define the matrices through their individual matrix elements

$$\mathbb{O}\left(\mathbf{R}_i, \mathbf{R}_{i+1}\right)_{a,a'} = \left\langle \mathbf{R}_i, a \middle| e^{-\tau \hat{h}_o} \middle| \mathbf{R}_{i+1}, a' \right\rangle \delta_{a,a'} \tag{2.33}$$

$$\mathbb{M}\left(\mathbf{R}_i\right)_{a,a'} = \left\langle \mathbf{R}_i, a \middle| e^{-\tau \hat{V}} \middle| \mathbf{R}_i, a' \right\rangle \tag{2.34}$$

We can express $g(\mathbf{R})$, eq. (2.17), in terms of the matrices $\mathbb{O}$ and $\mathbb{M}$

$$g(\mathbf{R}) = \sum_{\mathbf{a}}^{A} \prod_{i=1}^{P} \langle \mathbf{R}_i, a_i | \, e^{-\tau \hat{h}_o} \left| \mathbf{R}_{i+1}, a_i \right\rangle \left\langle \mathbf{R}_{i+1}, a_i \right| e^{-\tau \hat{V}} \left| \mathbf{R}_{i+1}, a_{i+1} \right\rangle \tag{2.35}$$

$$= \mathrm{Tr}_{\mathrm{A}} \left[ \prod_{i=1}^{P} \mathbb{O}(\mathbf{R}_i, \mathbf{R}_{i+1}) \mathbb{M}(\mathbf{R}_i) \right] \tag{2.36}$$

where the trace is over the electronic DoF. The PDF $g(\mathbf{R})$ represents a system with surface coupling. For most systems this PDF is computationally difficult to evaluate. We define our PDF $\varrho(\mathbf{R})$ for a system with no surface coupling and therefore $\mathbb{M}(\mathbf{R}_i) = \mathbb{1}$

$$\varrho(\mathbf{R}) = \mathrm{Tr}_{\mathrm{A}} \left[ \prod_{i=1}^{P} \mathbb{O}(\mathbf{R}_i, \mathbf{R}_{i+1}) \right] \tag{2.37}$$

In general this PDF will be less complex than $g(\mathbf{R})$ and will be computationally efficient to evaluate. It also has the important property of being a Gaussian mixture distribution [25]. In essence, this

means that $g(\mathbf{R})$ can be represented by $A$ multi-dimensional harmonic oscillators, and sampling from $g(\mathbf{R})$ is as simple as sampling from the Gaussians representing these harmonic oscillators. This property of $\varrho(\mathbf{R})$ is key to our PIMC method.

We proceed by outlining our method for calculating $\mathbb{O}$ and $\mathbb{M}$.

### 2.2.4 H.O. propagator

Consider a propagator $\langle x_1 | \, e^{-\tau \hat{h}_o} \, | x_2 \rangle$ where $\hat{h}_o$ has the form of a one-dimensional quantum harmonic oscillator in natural length coordinates. [3] The time-independent form of the Mehler Kernel [26] is an analytical expression for this propagator

$$K(x_1, x_2, \hbar\omega) = \left( \frac{1}{\sqrt{2\pi \sinh(\hbar\omega\tau)}} \right) \exp\left( \frac{-1}{2} \Big[ \left(x_1^2 + x_2^2\right) \cosh(\hbar\omega\tau) - 2\,\mathrm{csch}(\hbar\omega\tau) x_1 x_2 \Big] \right) \tag{2.38}$$

Using this form we can define an analytical expression for the matrix element $\mathbb{O}(\mathbf{R}_i, \mathbf{R}_{i+1})_{a,a}$

$$\mathbb{O}(\mathbf{R}_i, \mathbf{R}_{i+1})_{a,a} = \prod_j^N K_j^a(\mathrm{R}_i, \mathrm{R}_{i+1}, \hbar\omega) \tag{2.39}$$

$$= K_N^a(\mathbf{R}_i, \mathbf{R}_{i+1}, \hbar\boldsymbol{\omega}) \tag{2.40}$$

and then the matrix $\mathbb{O}$

$$\mathbb{O}(\mathbf{R}_i, \mathbf{R}_{i+1}) = \begin{bmatrix} K_N^1(\mathbf{R}_i, \mathbf{R}_{i+1}, \hbar\boldsymbol{\omega}) & & \\ & \ddots & \\ & & K_N^A(\mathbf{R}_i, \mathbf{R}_{i+1}, \hbar\boldsymbol{\omega}) \end{bmatrix} \tag{2.41}$$

### 2.2.5 Coupling propagator matrix form

We define the matrix form $\underline{\boldsymbol{V}}$ of the coupling operator $\hat{V}$ with eigenvalues $\epsilon_a$ and eigenvectors $U_a$

$$\underline{\boldsymbol{V}}(\mathbf{R}_i) = U_a(\mathbf{R}_i) \epsilon_a(\mathbf{R}_i) U_a^\intercal(\mathbf{R}_i) \tag{2.42}$$

[3] Nondimensionalization of the quantum harmonic oscillator is shown in Appendix C.

Giving us the expression for $\mathbb{M}$:

$$\mathbb{M}(\mathbf{R}_i) = \boldsymbol{U}(\mathbf{R}_i) \begin{pmatrix} e^{-\tau\epsilon_1(\mathbf{R}_i)} & & \\ & \ddots & \\ & & e^{-\tau\epsilon_A(\mathbf{R}_i)} \end{pmatrix} \boldsymbol{U}^{\intercal}(\mathbf{R}_i) \tag{2.43}$$

We have dervied a PI expression for $Z$ eq. (2.31) as the product of two terms $Z_f$ and $Z_\varrho$ which can be expressed in terms of matricies $\mathbb{O}$ and $\mathbb{M}$.

Next we outline our approach for calculating thermodynamic properties, such as the internal energy ($U$), and heat capacity ($C_v$).

## 2.3 Obtaining thermodynamic properties

To obtain thermodynamic properties, we derive expressions for the first and second $\beta$ derivatives of $Z_H$. The structure of our vibronic Hamiltonian makes the coupling operator $\hat{V}$ complicated, and consequently the direct computation of the $\beta$ derivatives of $\hat{V}$ is one we would like to avoid; hence the first and second $\beta$ derivatives are obtained using finite difference. Starting with $Z$ from eq. (2.24), evaluated at a temperature $\beta$

$$Z(\beta) = \int \mathrm{d}\mathbf{R}^P \, g\left(\mathbf{R}, \beta\right) \tag{2.44}$$

$$\frac{\partial Z(\beta)}{\partial \beta} = \int \mathrm{d}\mathbf{R}^P \, \frac{\partial}{\partial \beta} g\left(\mathbf{R}, \beta\right) \tag{2.45}$$

$$= \int \mathrm{d}\mathbf{R}^P \, \varrho(\mathbf{R}, \beta) \left(\frac{1}{\varrho(\mathbf{R}, \beta)}\right) \frac{\partial}{\partial \beta} g\left(\mathbf{R}, \beta\right) \tag{2.46}$$

We evaluate the $\beta$ derivative by finite difference

$$\frac{\partial}{\partial \beta} g\left(\mathbf{R}, \beta\right) \approx \left(\frac{1}{2\Delta\beta}\right) \Big[ g(\mathbf{R}, \beta + \Delta\beta) - g(\mathbf{R}, \beta - \Delta\beta) \Big] \tag{2.47}$$

$$= \left(\frac{1}{2\Delta\beta}\right) \Big[ \delta_{\Delta\beta}\left[g\right]\left(\mathbf{R}, \beta\right) \Big] \tag{2.48}$$

Obtaining the first symmetric derivative of $Z(\beta)$

$$\frac{\partial Z(\beta)}{\partial \beta} \approx \int \mathrm{d}\mathbf{R}^P \, \varrho(\mathbf{R}, \beta) \left( \frac{1}{2\Delta\beta} \right) \frac{\delta_{\Delta\beta} \left[ g \right] (\mathbf{R}, \beta)}{\varrho(\mathbf{R}, \beta)} \tag{2.49}$$

In the same fashion we obtain the second symmetric derivative of $Z(\beta)$

$$\frac{\partial^2 Z(\beta)}{\partial \beta^2} \approx \int \mathrm{d}\mathbf{R}^P \, \varrho(\mathbf{R}, \beta) \left( \frac{1}{\Delta\beta^2} \right) \left[ \frac{g\left(\mathbf{R}, \beta + \Delta\beta\right) - 2g\left(\mathbf{R}, \beta\right) + g\left(\mathbf{R}, \beta - \Delta\beta\right)}{\varrho(\mathbf{R}, \beta)} \right] \tag{2.50}$$

$$= \int \mathrm{d}\mathbf{R}^P \, \varrho(\mathbf{R}, \beta) \left( \frac{1}{\Delta\beta^2} \right) \frac{\delta^2_{\Delta\beta} \left[ g \right] (\mathbf{R}, \beta)}{\varrho(\mathbf{R}, \beta)} \tag{2.51}$$

It is important to note that $g\left(\mathbf{R}, \beta + \Delta\beta\right)$ and $g\left(\mathbf{R}, \beta - \Delta\beta\right)$ are present in both eq. (2.50) and eq. (2.47). During a PIMC simulation these terms are only calculated once *per sample point*, because they are equivalent given a fixed $\Delta\beta$. The second derivative can be obtained for no additional computational cost after calculating the first derivative. The finite difference method is therefore computationally advantageous.

### 2.3.1 Thermodynamic estimators

The internal energy of our system defined in terms of the partition function is

$$U_H = -\frac{\partial}{\partial \beta} \ln(Z_H) \tag{2.52}$$

Expanding $Z_H$ eq. (2.31) and using the properties of the natural logarithm we can show

$$U_H = U_f + U_\varrho \tag{2.53}$$

The internal energy of our system is therefore the internal energy obtained from our PIMC sampling, $U_f$, plus $\varrho$'s internal energy $U_\varrho$, which is calculated analytically. The $U_f$ can be considered the correction term for a coupled system, as $U_f = 0$ for a purely harmonic system.

To obtain $U_f$

$$U_f = \left( \frac{-1}{Z_f} \right) \frac{\partial}{\partial \beta} Z_f \tag{2.54}$$

We evaluate the first $\beta$ derivative of the partition function by finite difference [4]

$$\frac{\partial}{\partial\beta}Z_f \approx \left(\frac{Z_f^+ - Z_f^-}{2\Delta\beta}\right) \tag{2.55}$$

Giving us the estimator for $U_H$

$$U_H \approx U_\varrho + \left(\frac{-1}{Z_f}\right)\left(\frac{Z_f^+ - Z_f^-}{2\Delta\beta}\right) \tag{2.56}$$

The heat capacity of our system defined in terms of the partition function is

$$C_v^H = \left(\frac{1}{k_B T^2}\right)\frac{\partial^2}{\partial\beta^2}\ln(Z_H) \tag{2.57}$$

Expanding $Z_H$ eq. (2.31) and using the properties of the natural logarithm we can show

$$C_v^H = C_v^f + C_v^\varrho \tag{2.58}$$

The heat capacity of our system is therefore the heat capacity obtained from our PIMC sampling, $C_v^f$, plus $\varrho$'s heat capacity, $C_v^\varrho$, which is calculated analytically. The $C_v^f$ can be considered the correction term for a coupled system, as $C_v^f = 0$ for a fully harmonic system.
Given the form of $C_v^f$

$$C_v^f = \frac{1}{k_B T^2}\left[\left(\frac{1}{Z_f}\right)\frac{\partial^2}{\partial\beta^2}Z_f - (U_f)^2\right] \tag{2.59}$$

We evaluate the second $\beta$ derivative of the partition function by finite difference [5]

$$\frac{\partial^2}{\partial\beta^2}Z_f \approx \left(\frac{Z_f^+ - 2Z_f + Z_f^-}{\Delta\beta^2}\right) \tag{2.60}$$

Giving us the $C_v$ estimator

$$C_v^H \approx C_v^\varrho + \left[\frac{1}{k_B T^2}\right]\left[\left(\frac{1}{Z_f}\right)\left(\frac{Z_f^+ - 2Z_f + Z_f^-}{\Delta\beta^2}\right) - (U_f)^2\right] \tag{2.61}$$

[4] For the full derivation of the internal energy estimator see Appendix D.
[5] For the full derivation of the heat capacity estimator see Appendix E.

## 2.4 Implementation

In Chapter 3, PIMC results are plotted with standard error bars. Calculating $U$ and its standard error requires a statistical technique known as Jackknife [27]. Jackknife allows us to estimate averages of *non-linear* functions of averages. It also corrects for the (relatively small) sampling bias. Understanding our results and overall methodology does not require an understanding of Jackknife. The essential difference is that a small amount of post-processing is performed on the expectation values resulting from a PIMC calculation. The computational cost of this post-processing is negligible. The derivation of the Jackknife estimators is listed in the appendix. [6]

### 2.4.1 Additional Details

We now briefly outlineour implementation of the PIMC sampling. The basic action of the algorithm involves taking the mean of a function $f(\mathbf{R})$ over a range of values $\mathbf{R}_i \in \{\mathbf{R}_1, \cdots, \mathbf{R}_X\}$. In general this process can be grouped into three phases. Sample points $\mathbf{R}_i$ are drawn from the distribution $\varrho$. Function means $\overline{f}(\mathbf{R})$ are calculated by evaluating functions $f(\mathbf{R})$ over the sampled points. Finally, an estimate of $Z$, $U$, or $C_v$ is calculated using one or more function means.

For example if we wanted to estimate $U_H$ with sampling distribution $\varrho$, we would

- Sample $X$ points $\mathbf{R}_i$ from $\varrho$
- Evaluate $Z_f(\mathbf{R})$, $Z_f^+(\mathbf{R})$, and $Z_f^-(\mathbf{R})$ with those sampled points using eq. (D.10)
- Construct $\frac{\partial}{\partial\beta} Z_f$ from $Z_f^+(\mathbf{R})$, and $Z_f^-(\mathbf{R})$ using eq. (2.55)
- Construct $U_f$ from $\frac{\partial}{\partial\beta} Z_f$ and $Z_f(\mathbf{R})$
- Calculate $U_\varrho$ analytically

Giving us $U_H$ as the sum of $U_f$ and $U_\varrho$

[6] For the derivation of the Jackknife estimators see Appendix F.

# Chapter 3

# Challenging Model Systems

To investigate the effectiveness of our PIMC method, four systems were constructed: Superimposed, Displaced, Elevated, and Jahn-Teller. The nuclear coordinates for these systems are normal mode coordinates. To allow for numerical analysis such as sum-over-states (SOS), each system was restricted to two normal modes and two electronic surfaces. Each system has a single tunable parameter with a range of six values. PES plots and simulation results are presented over this range to demonstrate the behaviour of our PIMC method in different extremes. Note that all graphics are labelled with the associated tunable parameter in the upper right hand corner, and PIMC results are labelled with the associated choice of $\varrho$ in the top left hand corner. A consistent colour scheme is used to denote the two adiabatic PES and the harmonic oscillators comprising $\varrho$, as seen in Figures 3.2 to 3.5. In this chapter the two properties of interest are: $\tau$ convergence of PIMC results relative to the Trotter results, and suitability of $\varrho\left(\mathbf{R}\right)$ as a sampling distribution for $g\left(\mathbf{R}\right)$.

For each system the Hamiltonian is shown, followed by the system's parameter values, a paragraph describing the behaviour of the system over the range of the tunable parameter, and a static 3D plot of the system's two adiabatic PESs. This is followed by three 2D projections of the system over the tunable parameter range. The first plot is an elevation map of the lower PES: this plot uses a colour gradient to represent elevation of the PES in $\mathrm{eV}$. The minima of the harmonic oscillators comprising $\varrho$ are represented by a diamond ($\diamond$) and a cross ($+$). Around each minima is a circle of radius $6\sigma$, where $\sigma$ is the standard deviation of its respective harmonic oscillator. All PIMC calculations were carried out with one million samples. Therefore we expect all but 3.4 of these samples to be located inside the circle. This 2D visual representation of the harmonic oscillator can

be used to reason about the suitability of the distribution $\varrho$; these circles represent the limit from within which all samples are drawn.

The second and third 2D projections of each system show the behaviour of all PESs along the first and second normal mode dimension. The grid used to plot the PESs has an odd number of points: both 2D normal mode slices are located at the origin of this grid, $q_1 = 0$ for the $q_2$ slice and $q_2 = 0$ for the $q_1$ slice. A summary of the PIMC results is followed by $\tau$ convergence plots of $Z$ and $U$ for the simplest choice of $\varrho$ as $h_o$. Then we discuss an alternate choice of $\varrho$ and reason about its validity using three 2D projections of the system for both choices of $\varrho$. Finally we compare $\tau$ convergence plots of $Z$ and $U$ for both choices of $\varrho$.

Using Figure 3.1 as an example we will highlight the information present in the $\tau$ convergence plots.

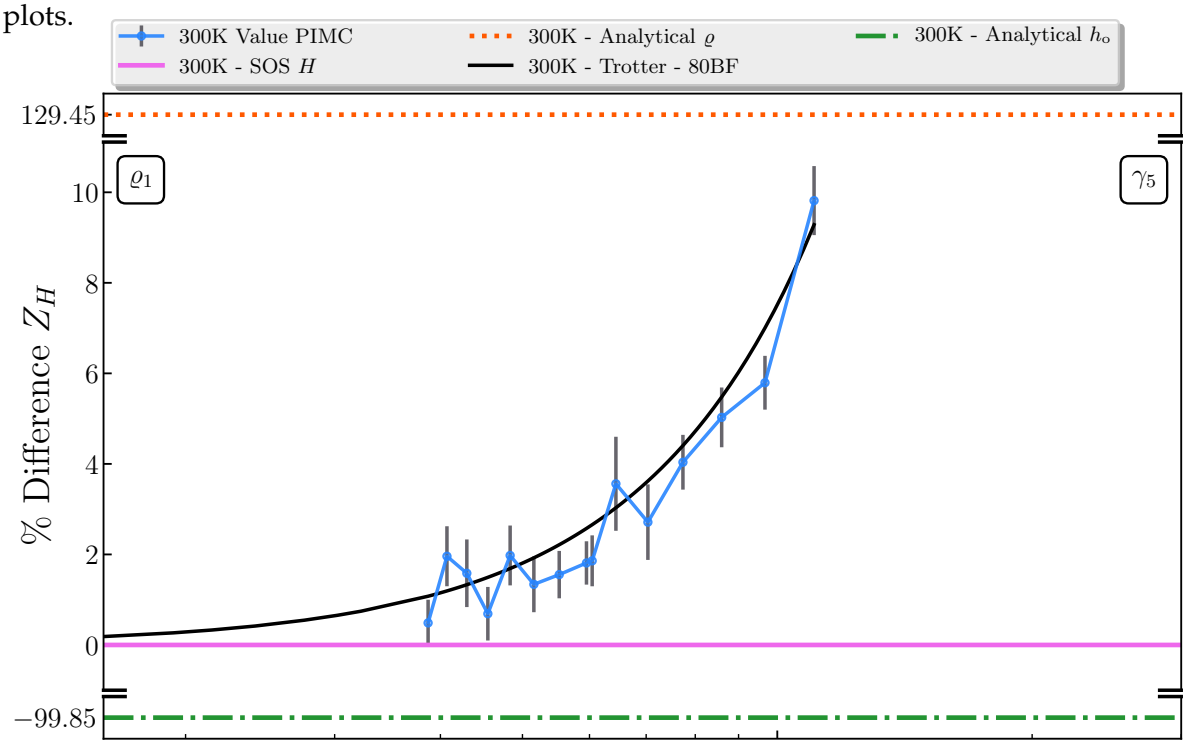


Figure 3.1: Example plot of $\tau$ convergence

We begin with the choice of our $y$ axis, which is defined as

$$y(x) = \left(\frac{x - Z_H}{Z_H}\right)(100) \tag{3.1}$$

$Z_H$ is calculated by SOS using 80 harmonic oscillator basis functions, for both normal modes, in the

second quantization formalism. Immediately a few important details are evident. If $\varrho$ is chosen to be $h_o$ then both analytical results will lie on top of each other. Conversely when an alternative $\varrho$ is chosen, as is the case in Figure 3.1, they will be distinct lines and one can make inferences about the suitability of $\varrho$ based on the relative distance from our SOS result and analytical $h_o$ result. Additionally it is important to realize that the sign in these plots is only representative of which parameter, $(x, Z_H)$, is larger.

Some plots have discontinuous axes. Figure 3.1 has two discontinuities, one above $\approx 11\%$ and one below $\approx -1\%$. They are indicated by pairs of black lines which extend into the graph. These discontinuities were added to preserve the $y$ scaling that presents useful information about the behaviour of the PIMC results near the Trotter results, and yet keep the graphs at a reasonable size. Without them the $y$ scale would be too coarse and remove detail from the associated plots.

Our PIMC method has four sources of error, not including the inevitable floating-point error associated with carrying out real-number calculations on a computer.

i) The choice of a finite $P$ introduces systematic error due to the Trotter factorization,eq. (2.16)

ii) The choice of a sampling distribution $\varrho(\mathbf{R})$ that is different from the true distribution $g(\mathbf{R})$

iii) Drawing a finite number of samples $X$ from $\varrho$ with which we evaluate our estimators

iv) The choice of a non-zero $\Delta\beta$ when evaluating the first and second $\beta$ derivatives of $Z$

The most accurate estimate of a property that we can calculate for a fixed choice of $P$ includes the error from the Trotter factorization (i). This is a formal error that we cannot eliminate. However, the other three sources of error ii, iii, iv can be mitigated and reduced. We can differentiate between these sources of error by comparing our PIMC results to SOS calculations that include the Trotter error, which are represented by black lines in the $\tau$ convergence plots. This is the key information that $\tau$ convergence plots provide. The Trotter result is the most accurate result we can obtain. Our goal is to minimize the difference between our PIMC results and the Trotter results.

All temperature dependent results were calculated at $300\mathrm{K}$ and the finite difference calculations were performed with $\Delta\beta = 2.0 \times 10^{-4}$. The symbol $\mathbf{ho} = \frac{1}{2}\sum_i \omega_i \left(\hat{q}_i^2 + \hat{p}_i^2\right)$ is used in each system's Hamiltonian. No results for $C_v$ are presented due to issues with the implementation of the estimator, and lack of confidence in the validity of plots. Results for $C_v$ require more investigation.

## 3.1 Superimposed system

This system is described by the following Hamiltonian:

$$\hat{H} = \hat{h}_o + \hat{V} \tag{3.2}$$

$$= \begin{bmatrix} E^a + \mathbf{ho} + \lambda\hat{q}_1 & 0 \\ 0 & E^b + \mathbf{ho} + \lambda\hat{q}_1 \end{bmatrix} + \begin{bmatrix} 0 & \gamma\hat{q}_2 \\ \gamma\hat{q}_2 & 0 \end{bmatrix} \tag{3.3}$$

Table 3.1: Superimposed system parameters

| Parameter | Value/eV | Parameter | Value/eV |
|---|---|---|---|
| $E^a$ | 0.0996 | $\gamma_1$ | 0.00 |
| $E^b$ | 0.1996 | $\gamma_2$ | 0.04 |
| $\omega_1$ | 0.02 | $\gamma_3$ | 0.08 |
| $\omega_2$ | 0.04 | $\gamma_4$ | 0.12 |
| $\lambda$ | 0.072 | $\gamma_5$ | 0.16 |
| | | $\gamma_6$ | 0.20 |

Results are analyzed as a function of $\gamma$, the coupling term. At $\gamma_1$ the two PESs are superimposed. As we increase $\gamma$ they are displaced along the $q_2$ axis, as shown in Figure 3.3, and Figure 3.5. There should be no change in the $q_1$ direction, which is evident in Figure 3.4. The Superimposed system is designed to show the effect of a system's coupling strength on our PIMC method.

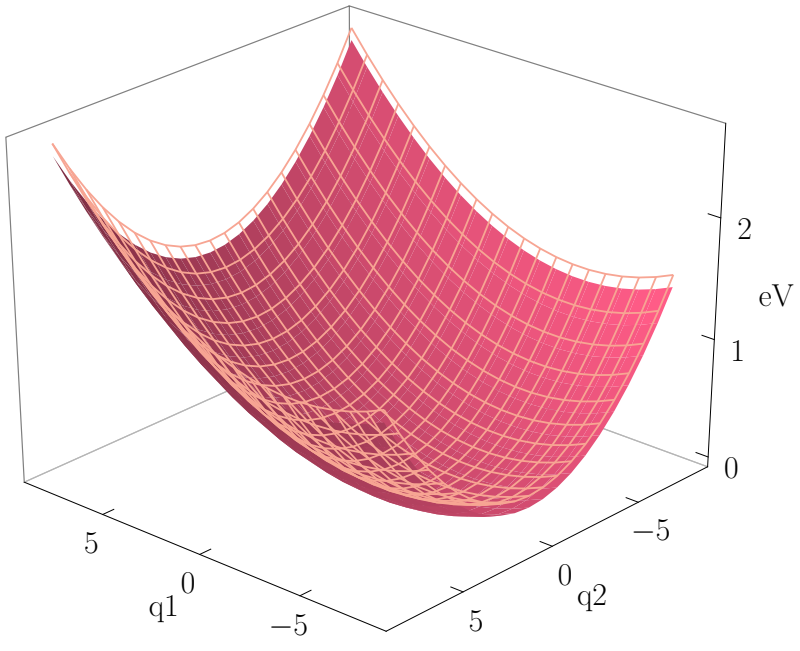


Figure 3.2: Static 3D image of Superimposed system

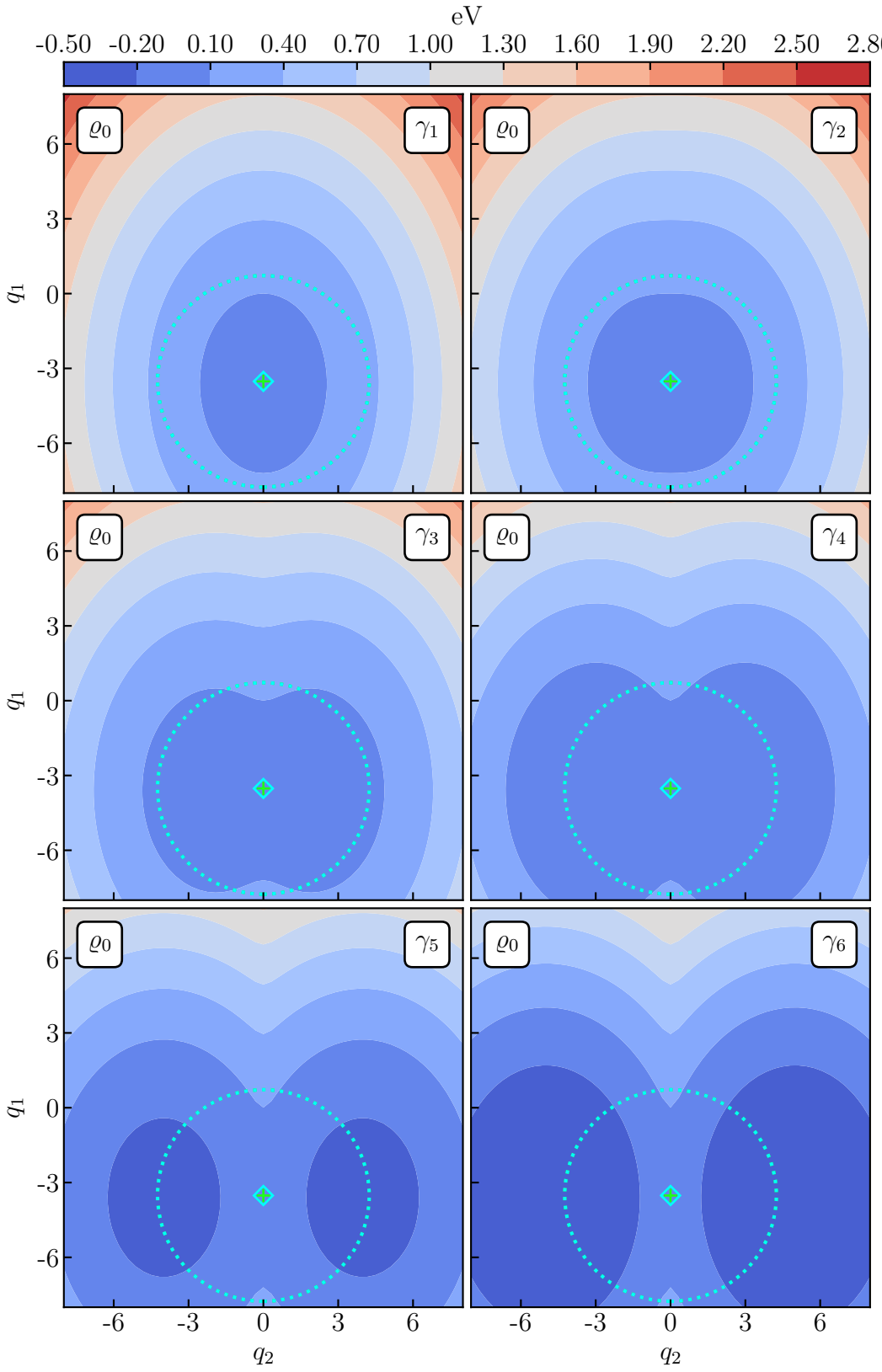


Figure 3.3: Elevation maps of lower surface for Superimposed system

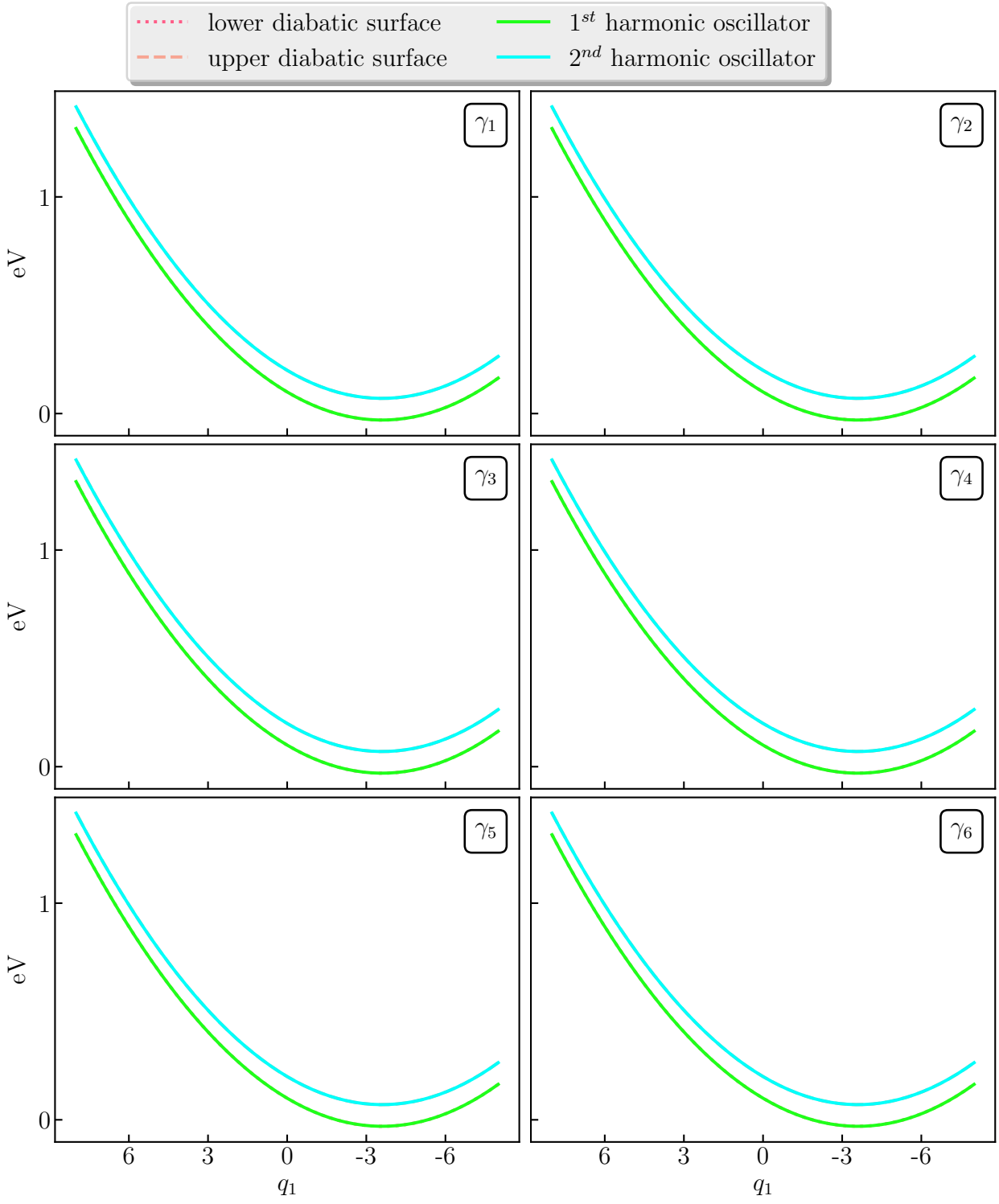


Figure 3.4: $q_1$ slices of Superimposed system

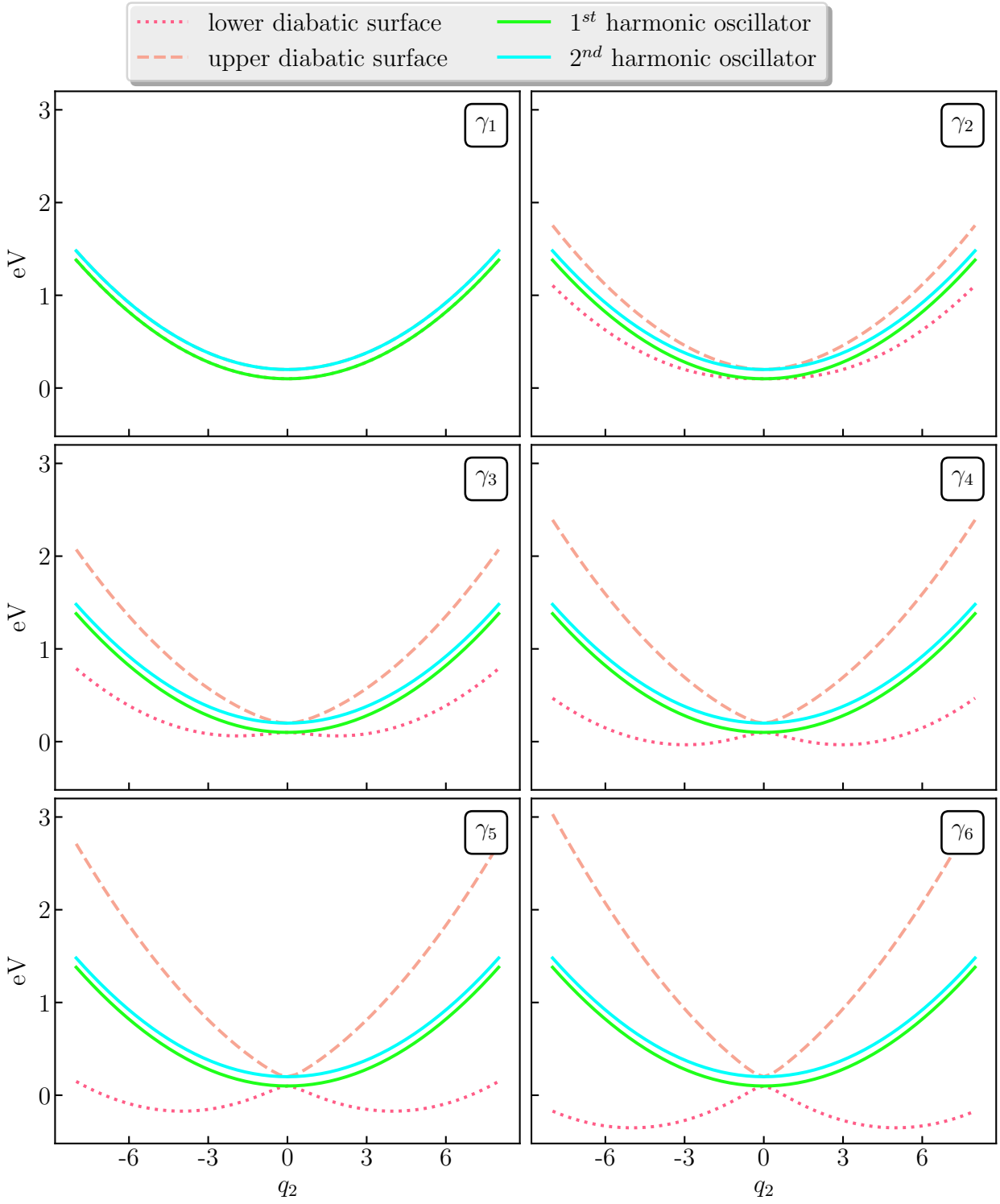


Figure 3.5: $q_2$ slices of Superimposed system

### PIMC results

The Superimposed system is purely harmonic for $\gamma_1$, therefore the analytical, SOS, and Trotter results should be equal. This is what we observe in Figure 3.6. Note that there is a non-zero difference due to floating point error; this difference is on the order of $10^{-15}$ and has no noticeable effect. The PIMC method exactly reproduces these results for all bead values.

The Trotter and PIMC results are a better approximation than the analytical results for $\gamma_2$, and their relative accuracy improves as the coupling term increases. This is shown by the discrepancy between the SOS and analytical lines. For $\gamma_2$ the analytical result is $\sim 35\%$ off, whereas for $\gamma_3$ the difference is $\sim 89\%$.

We begin to see relatively small discrepancies between the Trotter and PIMC results for $\gamma_3$ and larger discrepancies for $\gamma_4$. Looking at Figure 3.3 we see that a double well in the $q_2$ direction is slowly forming, and the H.O. description of the system is beginning to suffer in the outer $q_2$ region.

For $\gamma_5$ and $\gamma_6$ we can see a barrier is now present in Figure 3.3. The coupling in the $q_2$ direction is strong and cannot be neglected. A proper description of the full distribution requires inclusion of these effects. The choice of $\varrho$, which does not include these effects, is a poor description of the distribution, as evident in Figure 3.7. The PIMC results are no longer converging to our SOS results as $\tau \to 0$. Instead they are converging towards the analytical result for the purely harmonic portion of the system $h_o$. We can see that the choice of our distribution $\varrho$ is critical to the success of our PIMC method.

The energy is harder to analyze, which to some degree is expected as the estimator is a *non-linear* function of averages. The overall $\tau$ convergence of our PIMC results appears to follow our SOS results. However, there is a lot of noise in the low $\tau$ region. It is important to take into consideration that the standard PI energy estimator suffers from similar variance in the low $\tau$ regime [28]. Modified estimators have been used to remedy this statistical fluctuation; however adapting their form for our PIMC is complicated by our Hamiltonian's electronic DoF. At this time we have not been able to derive a modified estimator to reduce this variance. In general, we see the same effects on the energy as we did with the partition function. From $\gamma_1$ to $\gamma_4$, $\varrho(\mathbf{R})$ is a reasonable approximation to $g(\mathbf{R})$ and the PIMC results match the SOS results. For $\gamma_5$ and $\gamma_6$ the approximation is clearly poor as the error in the PIMC results is on the order of $40\ \mathrm{kJ\ mol^{-1}}$.

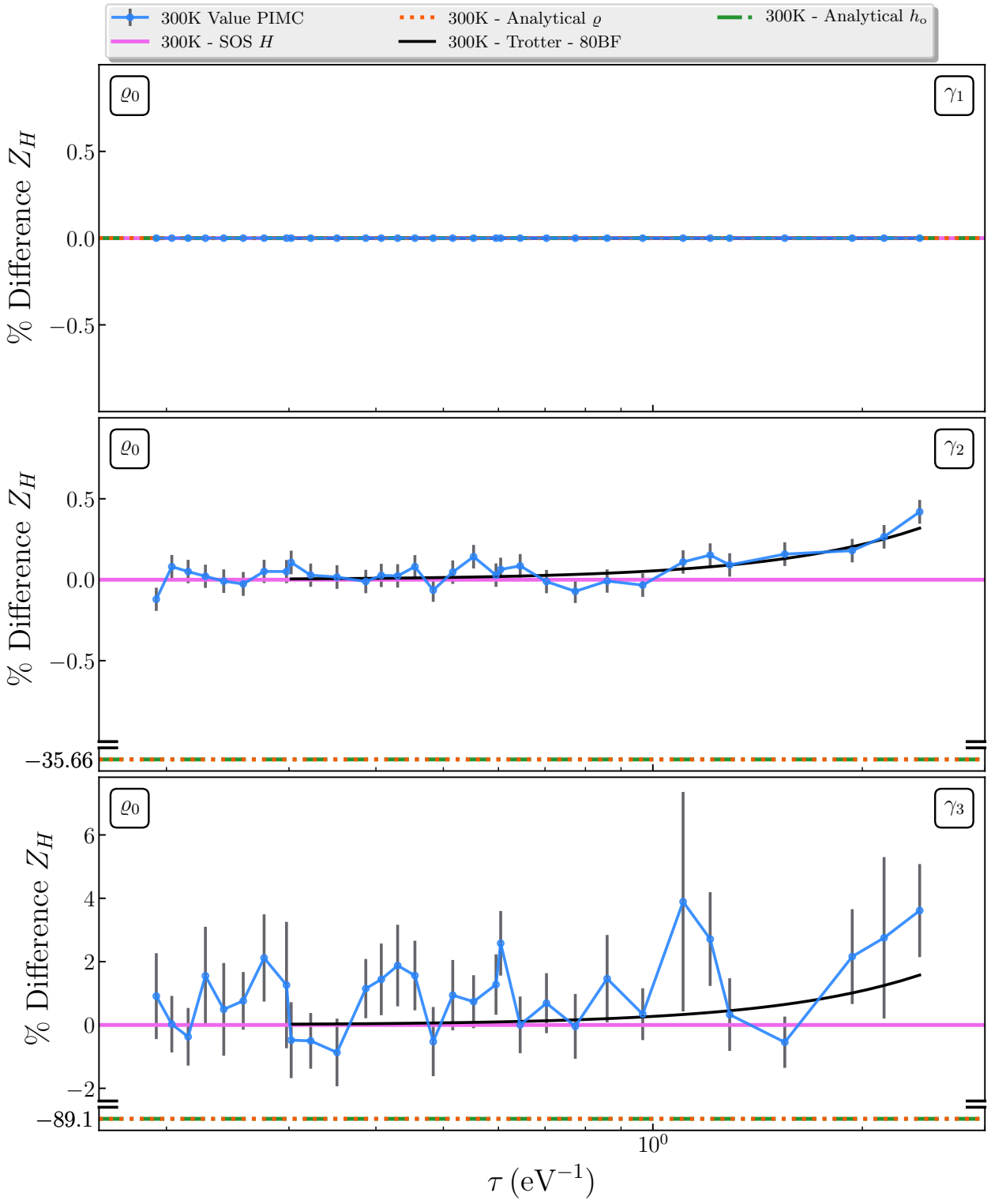


Figure 3.6: PIMC calculation of $Z$ for Superimposed system over $\gamma_1 - \gamma_3$ range

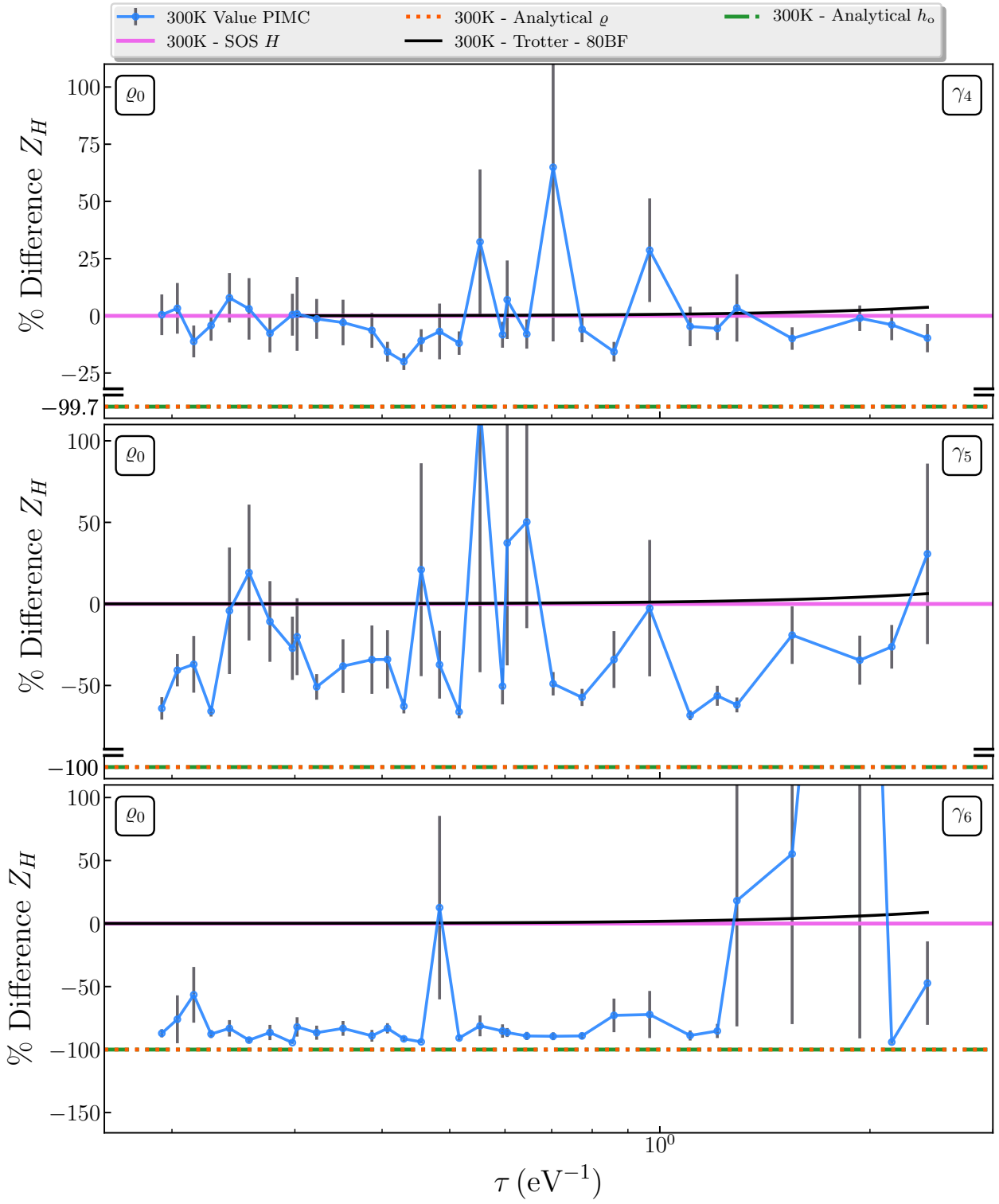


Figure 3.7: PIMC calculation of $Z$ for Superimposed system over $\gamma_4 - \gamma_6$ range

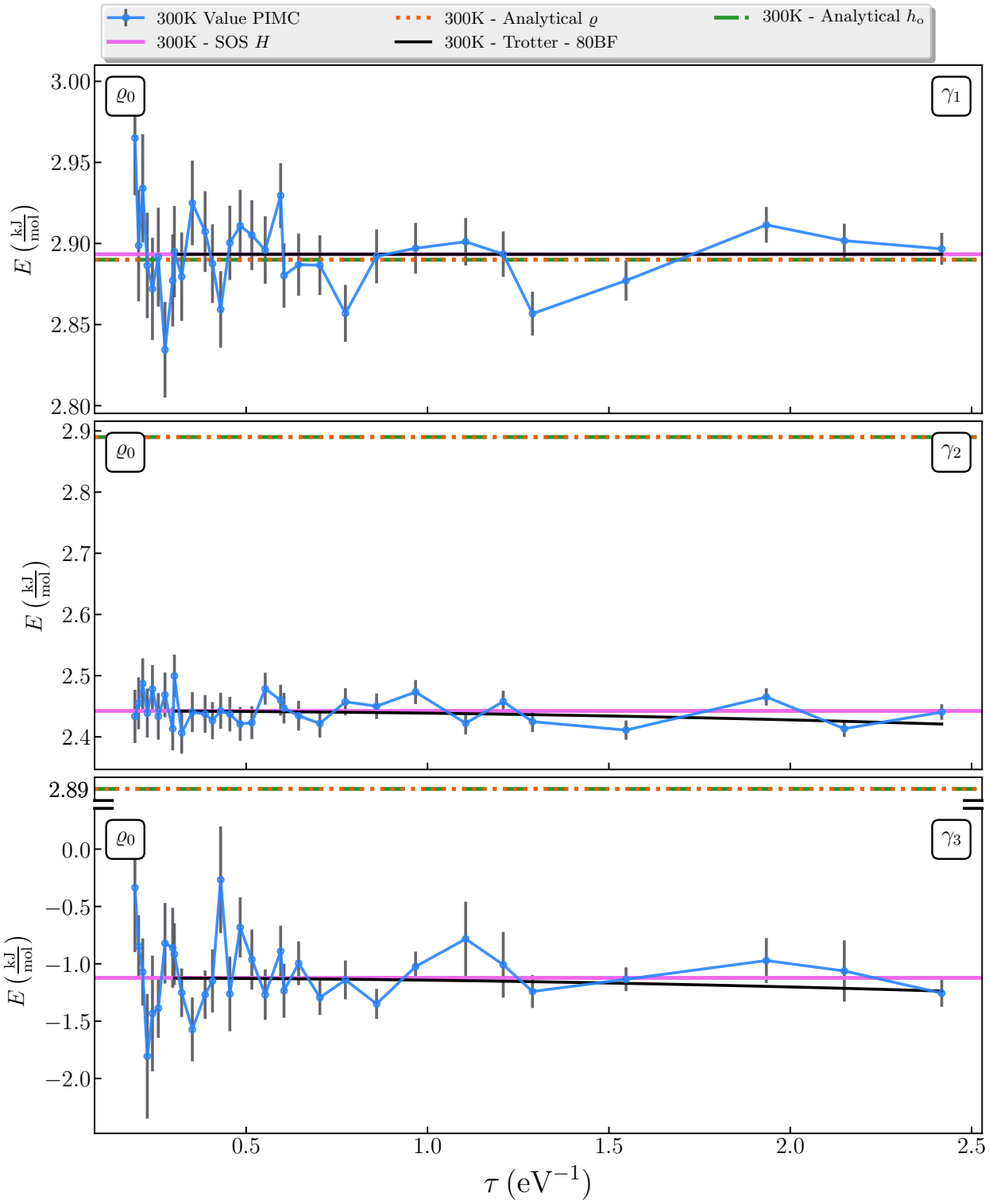


Figure 3.8: PIMC calculation of $E$ for Superimposed system over $\gamma_1 - \gamma_3$ range

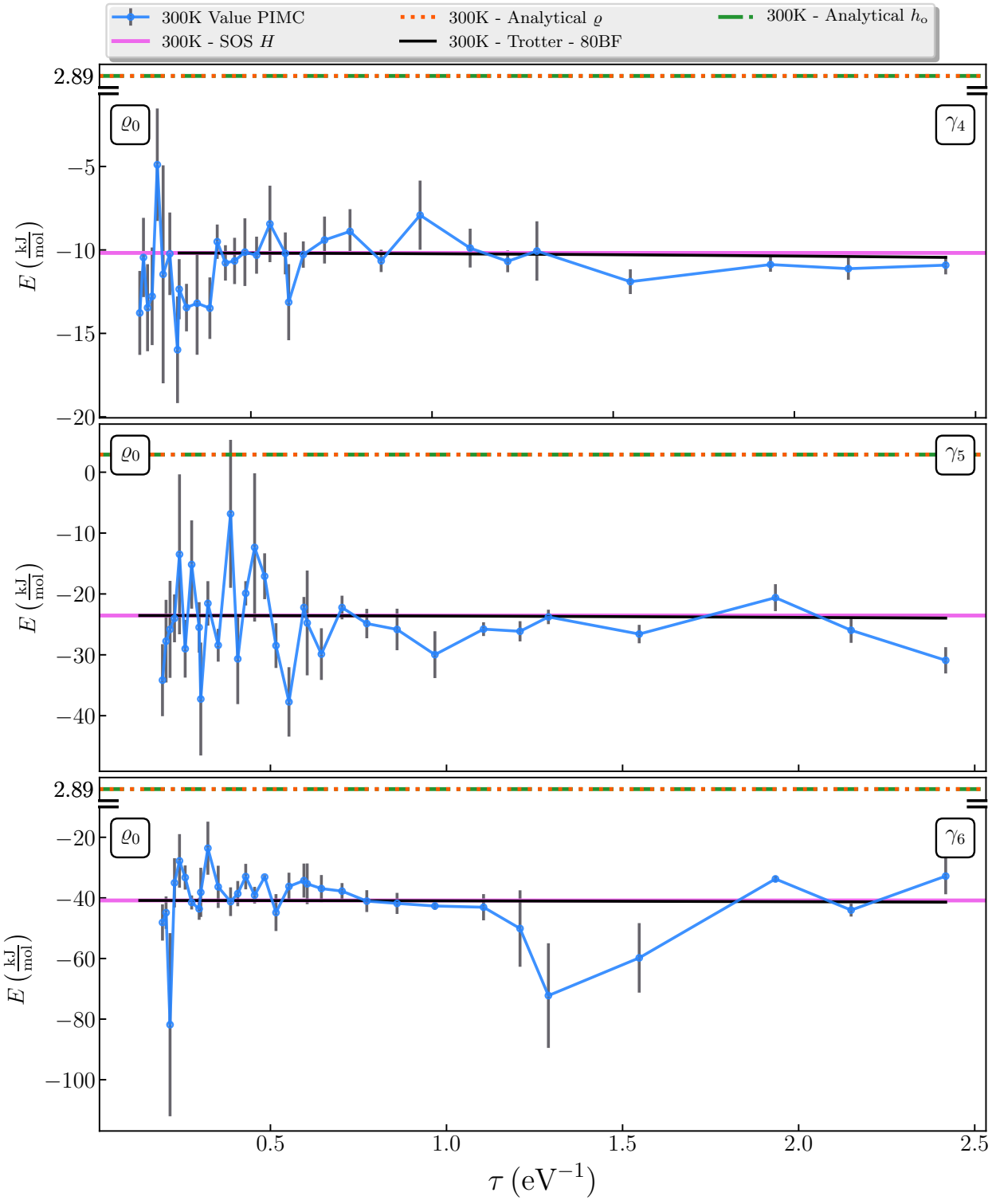


Figure 3.9: PIMC calculation of $E$ for Superimposed system over $\gamma_4 - \gamma_6$ range

### Alternative sampling distributions

It is evident that our original choice of $\varrho$

$$\begin{bmatrix} E^a + \mathbf{ho} + \lambda\hat{q}_1 & 0 \\ 0 & E^b + \mathbf{ho} + \lambda\hat{q}_1 \end{bmatrix} \tag{3.4}$$

is a poor description of the Superimposed system for $\gamma_5$ and $\gamma_6$. As we increase the coupling parameter $\gamma$, the contribution from the $q_2$ mode increases and we push the system farther into the nonadiabatic regime. The obvious modification to our distribution is to include a $q_2$ term. We choose a new distribution, using the same values, but including a $q_2$ term:

$$\begin{bmatrix} E^a + \mathbf{ho} + \lambda\hat{q}_1 + \gamma\hat{q}_2 & 0 \\ 0 & E^b + \mathbf{ho} + \lambda\hat{q}_1 - \gamma\hat{q}_2 \end{bmatrix} \tag{3.5}$$

We refer to our 2D projections of this new distribution $\varrho_1$ to analyze the effectiveness of our modification. Figure 3.10 indicates that $\varrho_1$ is a better distribution than $\varrho_0$. Very clearly we see in Figure 3.11 that we are now capturing the $q_2$ effects. This figure also shows us how $\varrho_0$ was overweighting the local maximum at $q_2 = 0$ and underweighting the local minimums at $q_2 \approx \pm 5$. In Figure 3.10 we see that our new distribution captures the $q_2$ effects for $\gamma_5$ and $\gamma_6$. We therefore expect that the PIMC results for $Z$ and $U$ will show noticeable improvement.

Figure 3.14 shows an amazing improvement of the stochastic error compared to Figure 3.13. With our improved distribution $\varrho_1$ the error has been reduced from approximately $100\%$ to $1\% \sim 2\%$. This shows that the choice of the sampling distribution dominates the statistical error present in our method. We see similar results for the energy when comparing Figure 3.16 and Figure 3.15. There is an error reduction from $50\% \sim 100\%$ to approximately $1\%$. However, along with this error reduction is an energy shift discrepency. A fit of the PIMC results follows the same trend as the Trotter results. The absolute values, however, are off by approximately $2\,\mathrm{kJ\,mol^{-1}}$. It is not certain if this is an error in our method or in our implementation at this time. More investigation of this energy shift is needed.

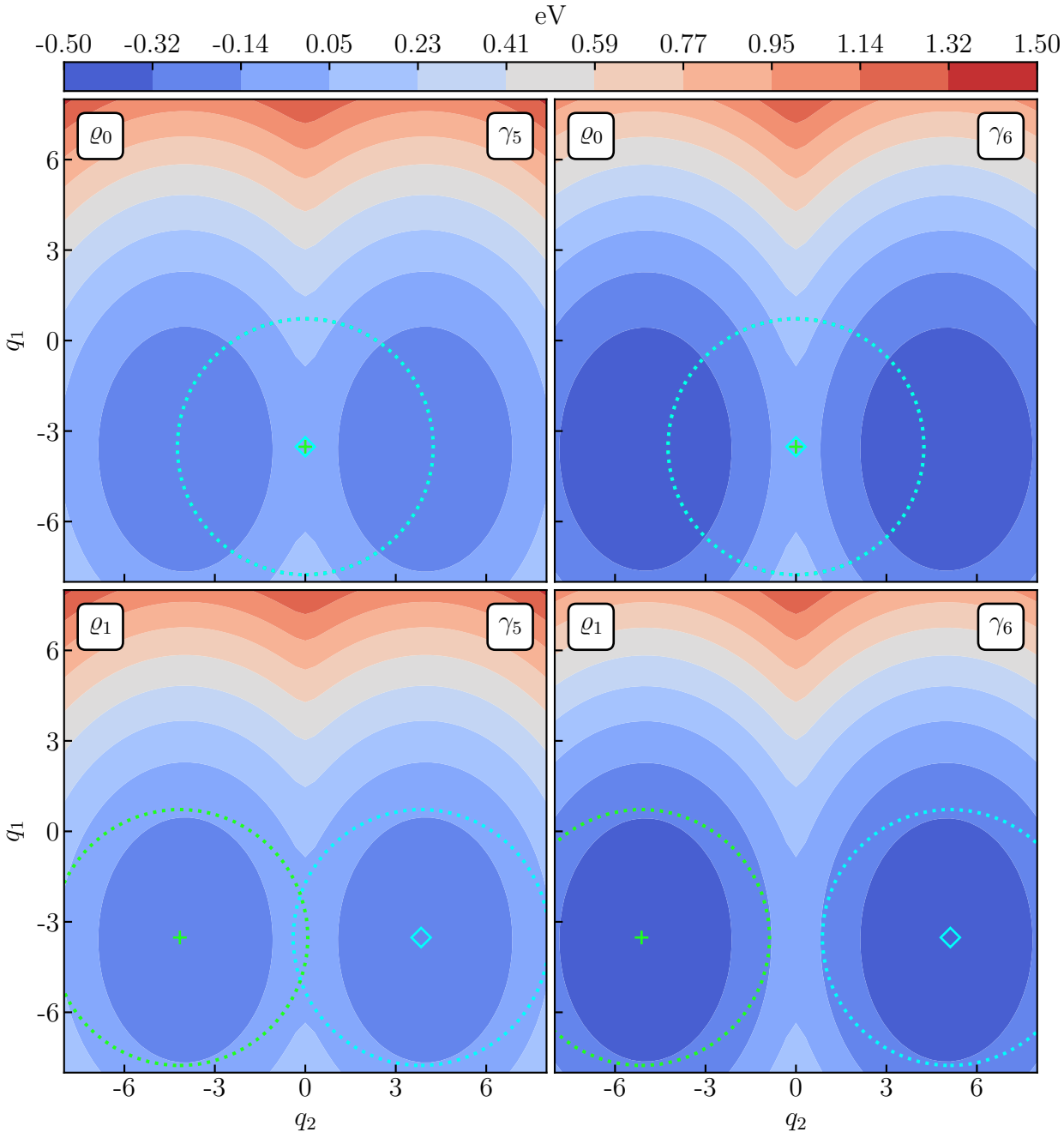


Figure 3.10: Elevation map of lower surface of Superimposed system for two choices of $\varrho$

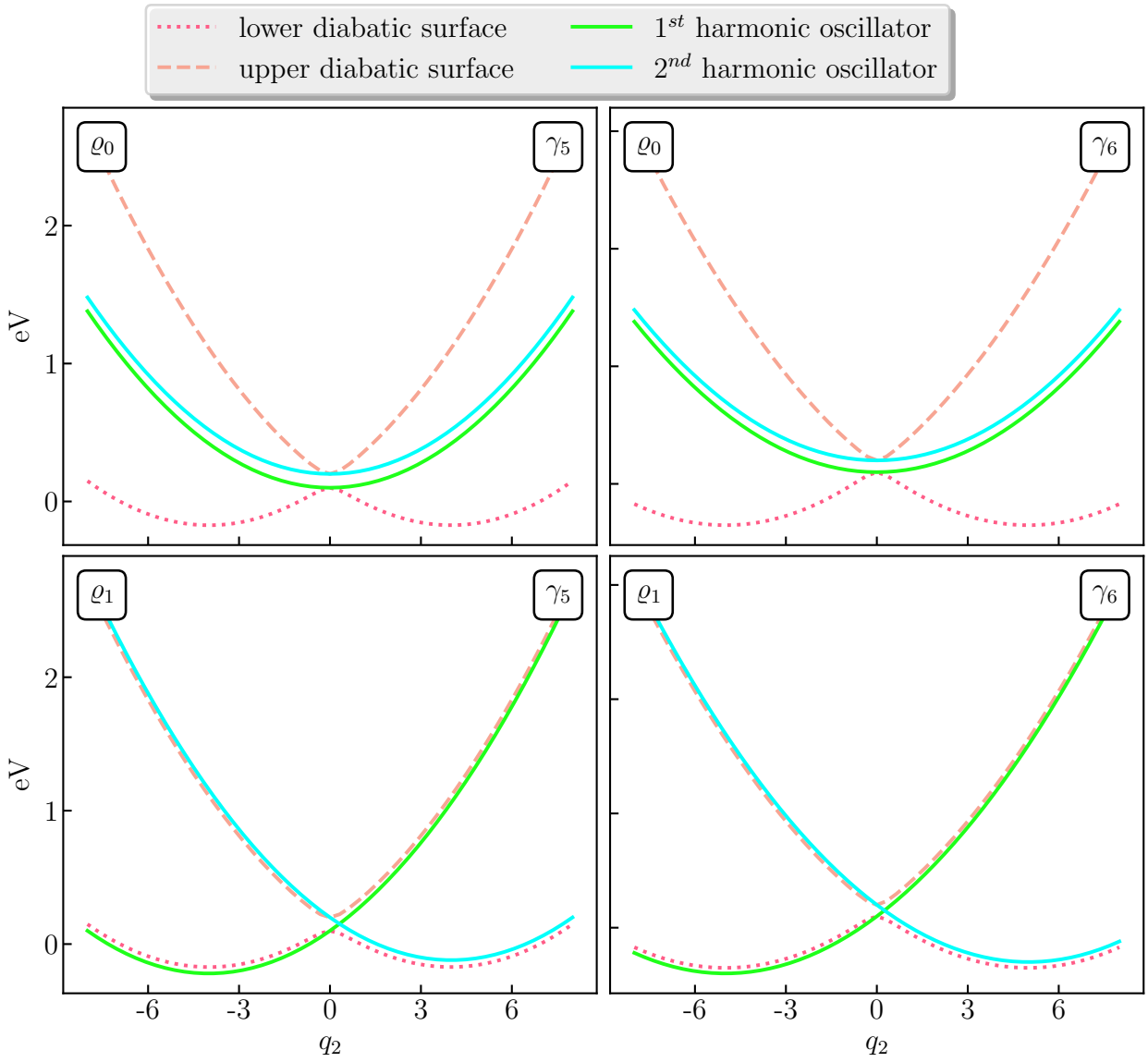


Figure 3.11: $q_2$ slices of Superimposed system for two choices of $\varrho$

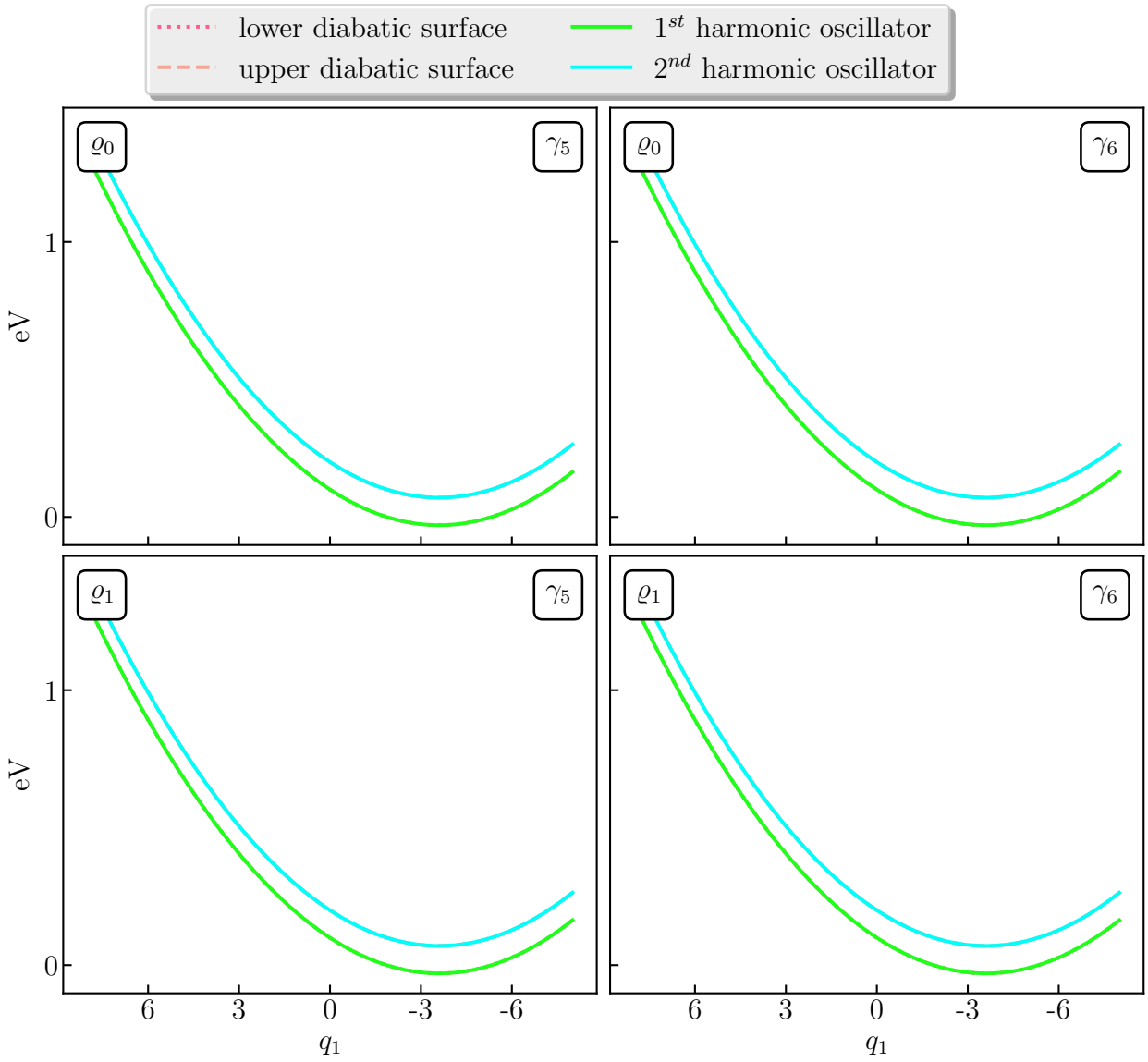


Figure 3.12: $q_1$ slices of Superimposed system for two choices of $\varrho$

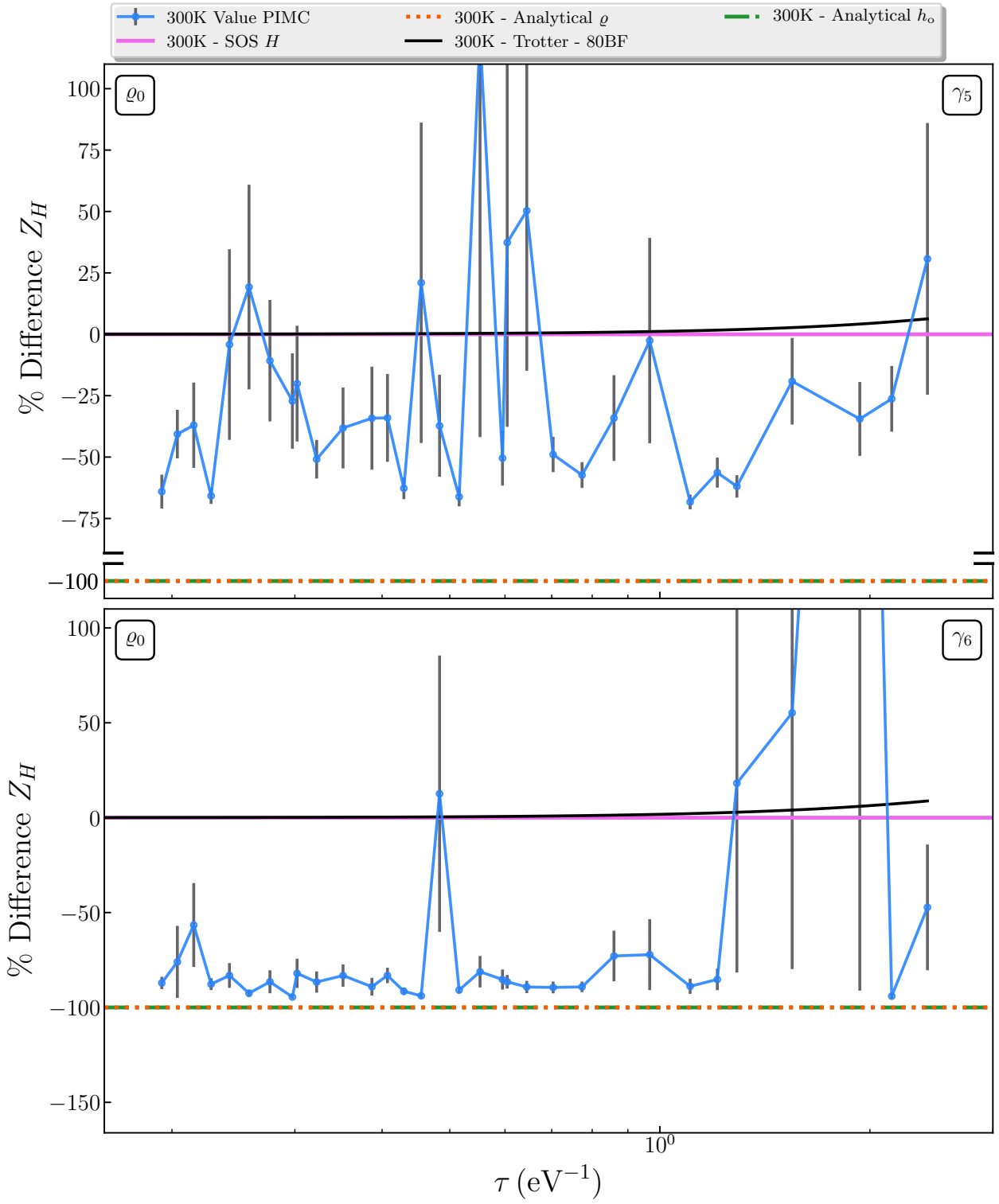


Figure 3.13: PIMC calculation of $Z$ using $\varrho_0$ for Superimposed system over $\gamma_5 - \gamma_6$ range

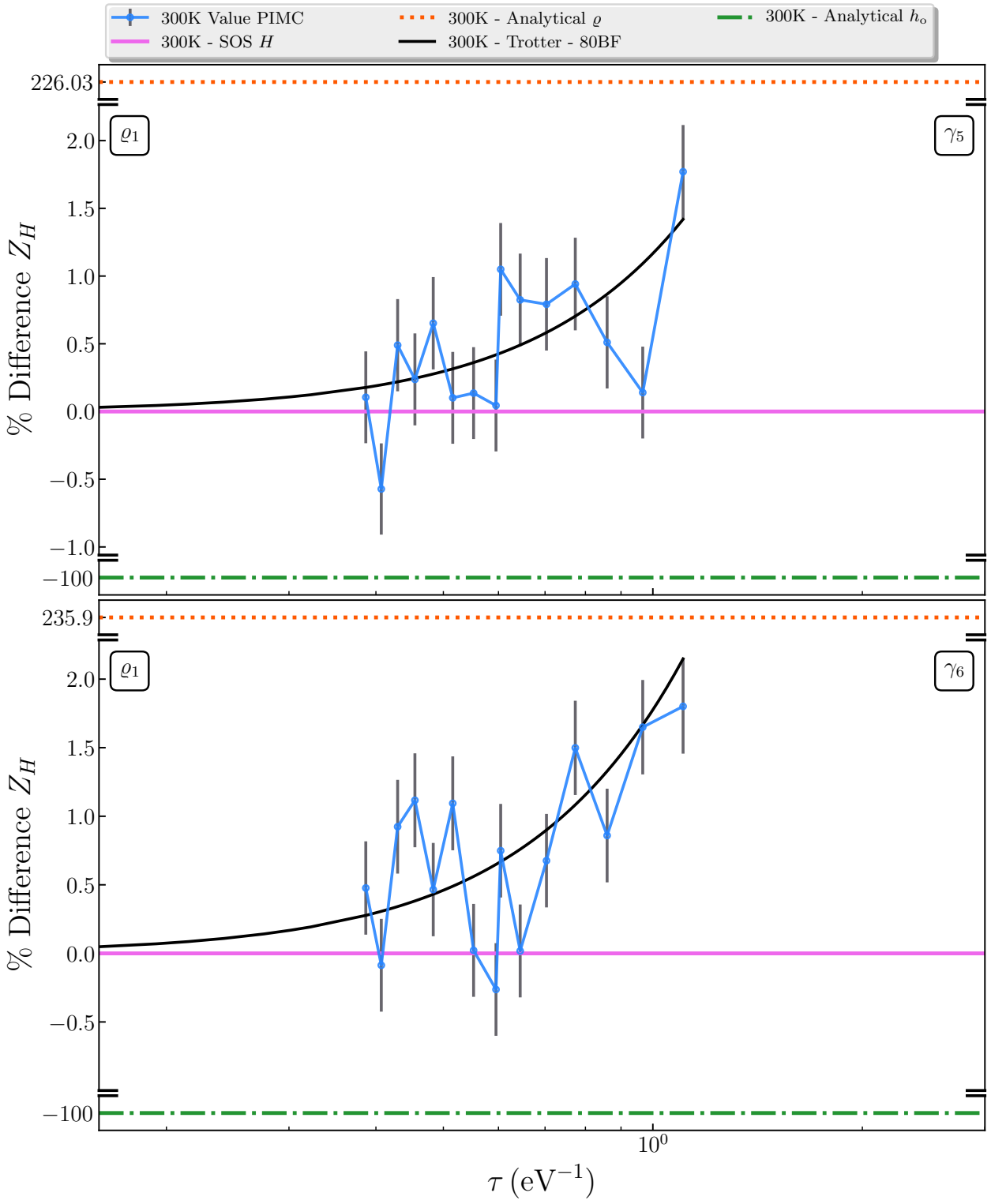


Figure 3.14: PIMC calculation of $Z$ using $\varrho_1$ for Superimposed system over $\gamma_5 - \gamma_6$ range

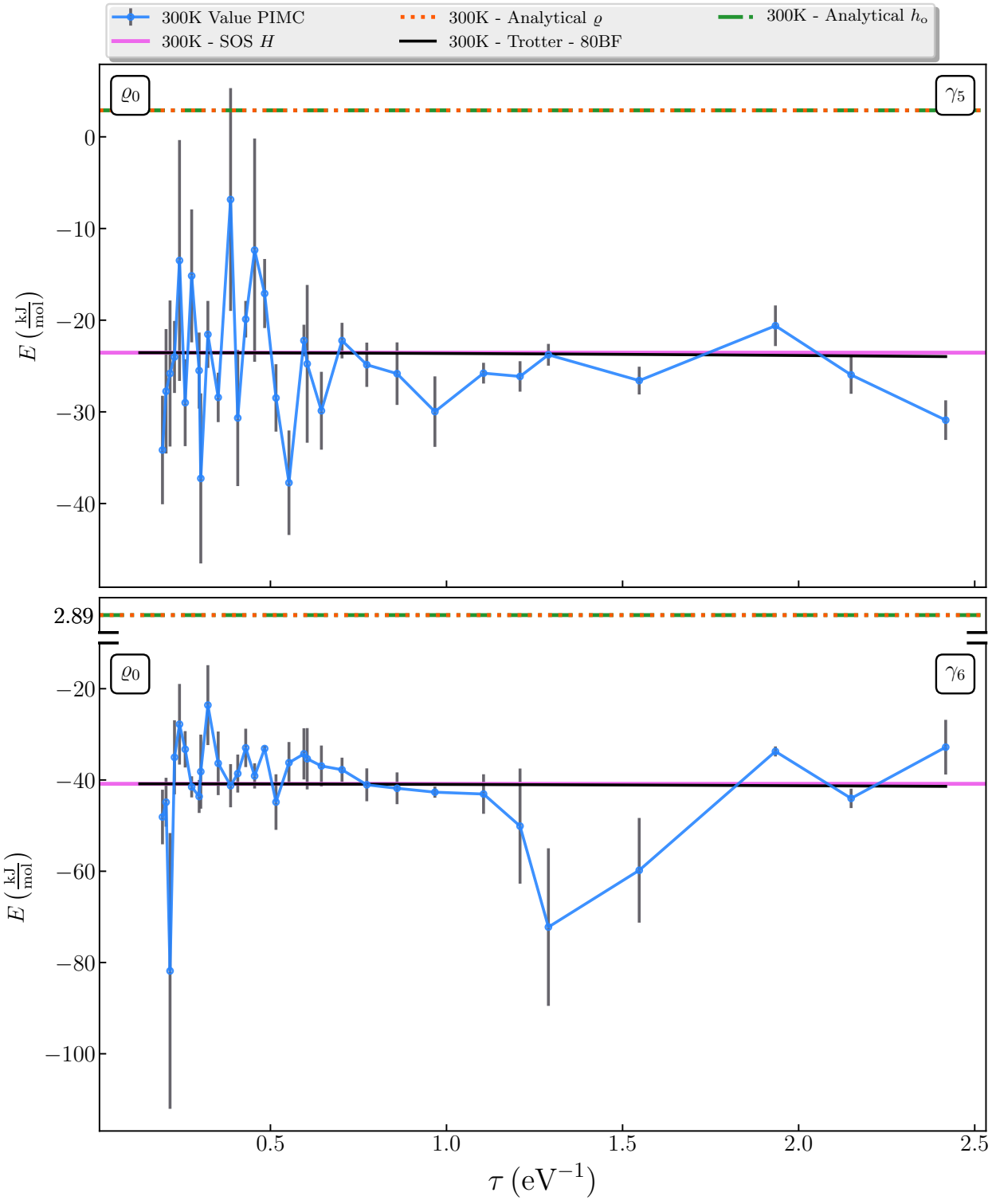


Figure 3.15: PIMC calculation of $E$ using $\varrho_0$ for Superimposed system over $\gamma_5 - \gamma_6$ range

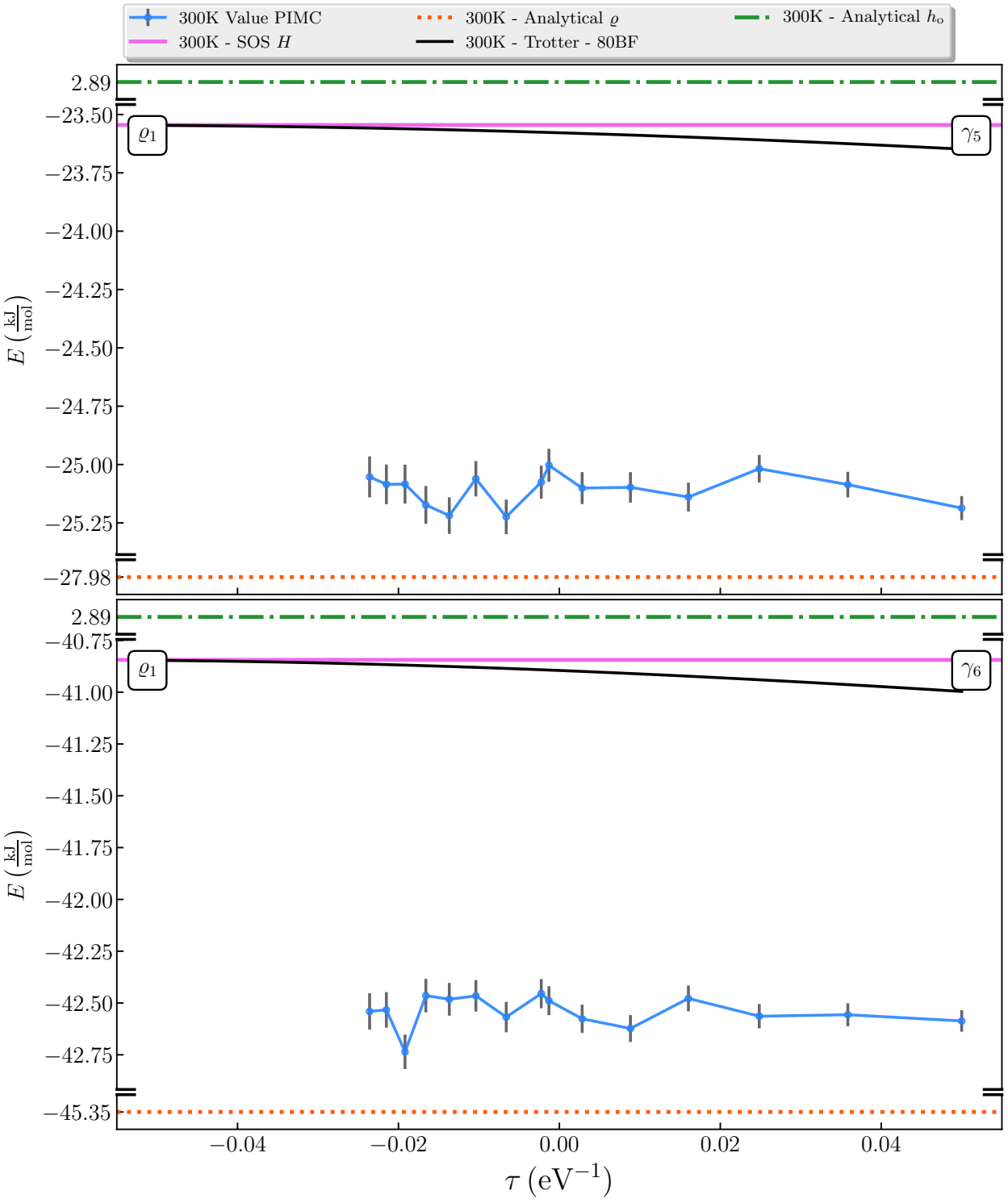


Figure 3.16: PIMC calculation of $E$ using $\varrho_1$ for Superimposed system over $\gamma_5 - \gamma_6$ range

## 3.2 Displaced system

This system is described by the following Hamiltonian:

$$\hat{H} = \hat{h}_o + \hat{V} \tag{3.6}$$

$$= \begin{bmatrix} E^a + \mathbf{ho} + \lambda\hat{q}_1 & 0 \\ 0 & E^b + \mathbf{ho} - \lambda\hat{q}_1 \end{bmatrix} + \begin{bmatrix} 0 & \gamma\hat{q}_2 \\ \gamma\hat{q}_2 & 0 \end{bmatrix} \tag{3.7}$$

Table 3.2: Displaced system parameters

| Parameter | Value/eV | Parameter | Value/eV |
|---|---|---|---|
| $E^a$ | 0.0996 | $\gamma_1$ | 0.00 |
| $E^b$ | 0.1996 | $\gamma_2$ | 0.04 |
| $\omega_1$ | 0.02 | $\gamma_3$ | 0.08 |
| $\omega_2$ | 0.04 | $\gamma_4$ | 0.12 |
| $\lambda$ | 0.072 | $\gamma_5$ | 0.16 |
| | | $\gamma_6$ | 0.20 |

Results are analyzed as a function of $\gamma$, the coupling term. At $\gamma_1$ the two PESs are displaced along the $q_1$ axis. As we increase $\gamma$ they are displaced along the $q_2$ axis, as shown in Figure 3.18, and Figure 3.20. There should be no change in the displacement along the $q_1$ direction, which is evident in Figure 3.19. The Displaced system highlights the effect on both the accuracy and efficiency of sampling when there are multi-modal displacements. It is expected that this system should be more difficult to sample than the Superimposed system at higher $\gamma$ values.

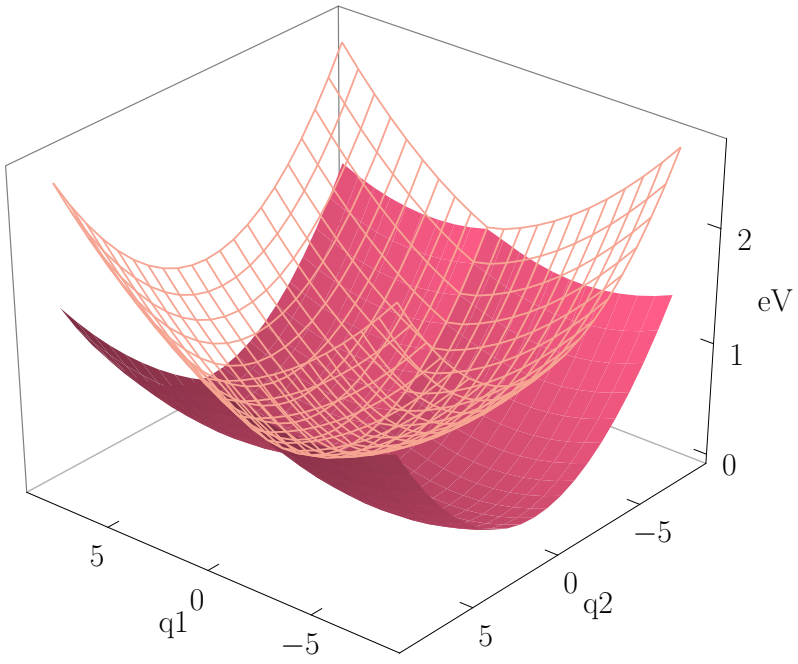


Figure 3.17: Static 3D image of Displaced system

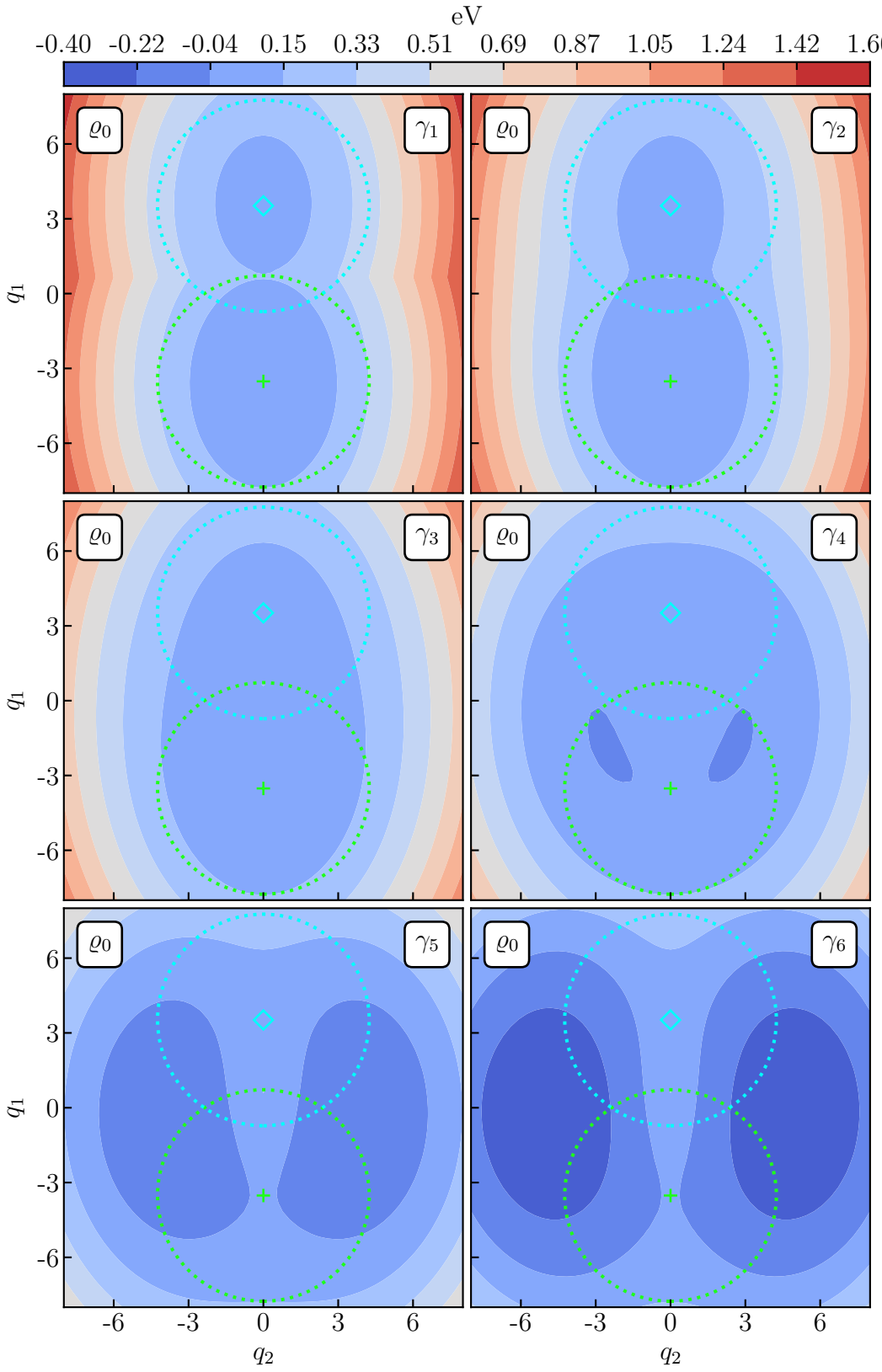


Figure 3.18: Elevation maps of lower surface for Displaced system

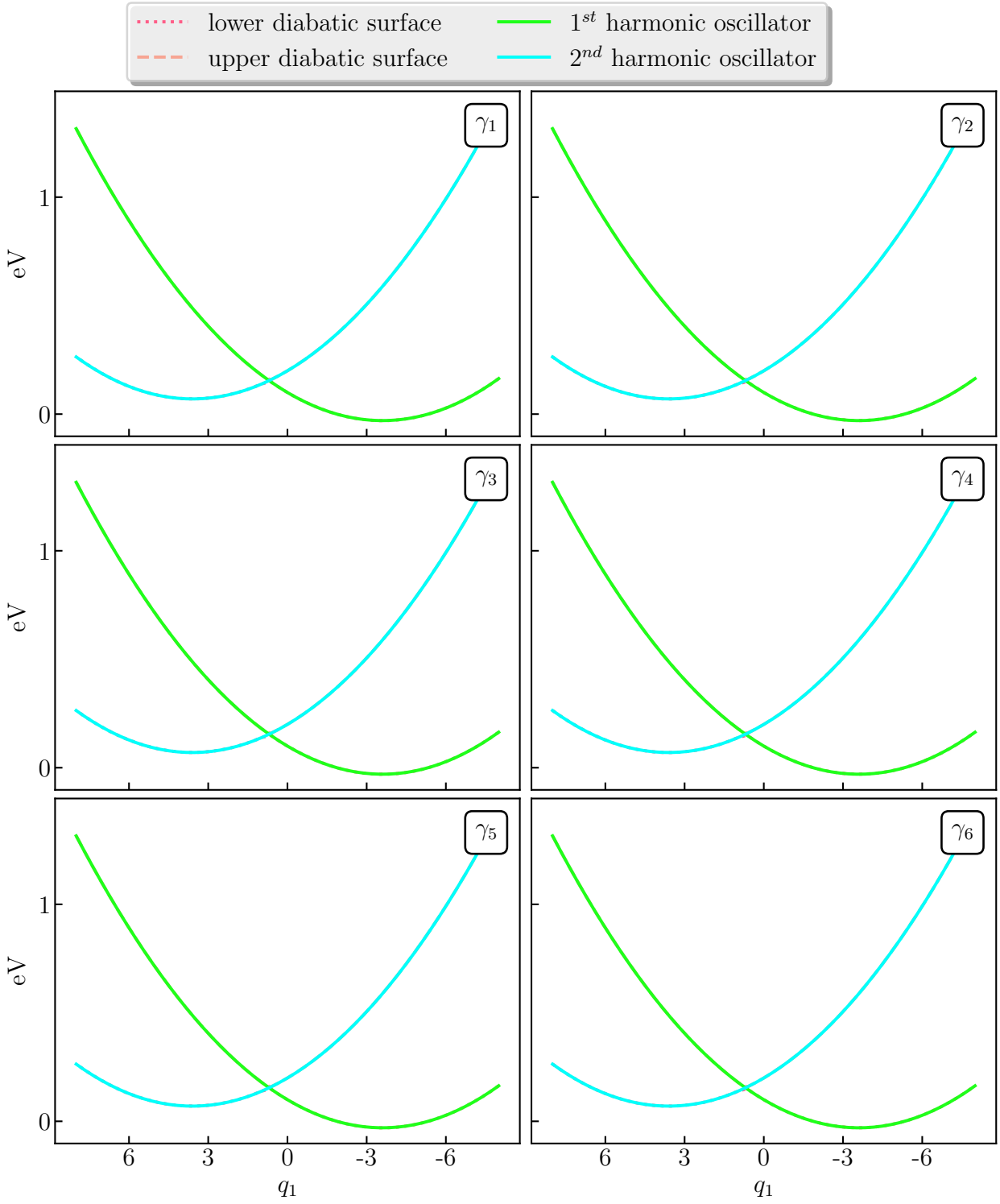


Figure 3.19: $q_1$ slices of Displaced system

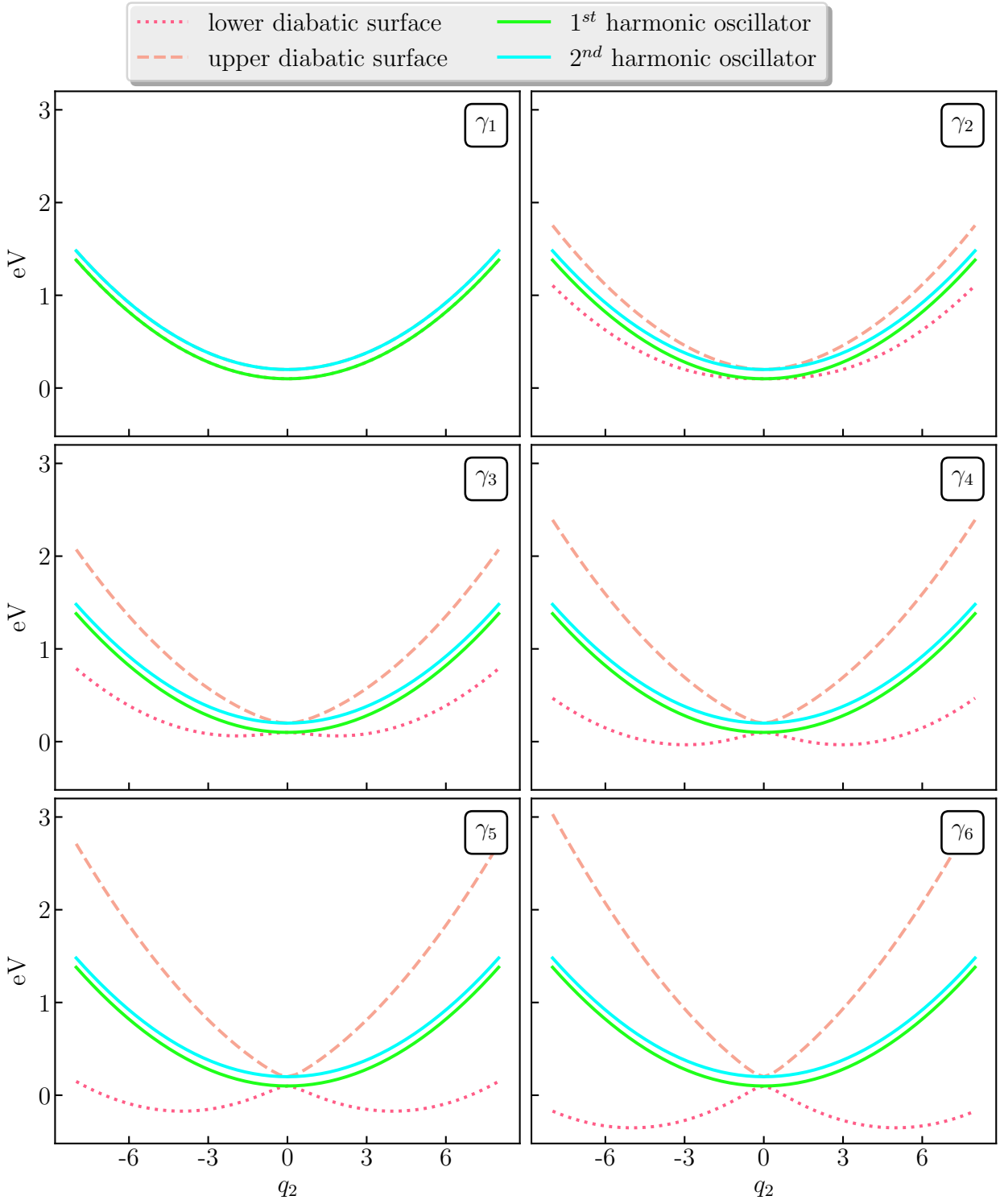


Figure 3.20: $q_2$ slices of Displaced system

### PIMC results

The Displaced system is purely harmonic for $\gamma_1$, therefore the analytical, SOS, and Trotter results should be equal in all $\tau$ regimes. This is what we observe in Figure 3.21. Again, there is a non-zero difference due to floating point error. The PIMC method exactly reproduces these results for all bead values.

The Trotter and PIMC results are better approximations than the analytical H.O. for $\gamma_2$, and their relative accuracy improves as the coupling term increases. This is shown by the discrepancy between the SOS and analytical lines. Comparing these results with the ones from the Superimposed system, we see that the analytical H.O. method is less suitable in the Superimposed model. For $\gamma_2$ the analytical result is $\sim 8\%$ off compared to $\sim 35\%$ off for the Superimposed model. For $\gamma_3$ the analytical result is $\sim 36\%$ off compared to $\sim 90\%$ off for the Superimposed model. This difference is due to the interaction between the $q_1$ and $q_2$ displacements.

We begin to see relatively small discrepancies between the Trotter and PIMC results for $\gamma_3$ and larger discrepancies for $\gamma_4$. Despite these discrepancies, the PIMC results very clearly converge to our SOS results. Looking at Figure 3.18 the H.O.s comprising $\varrho_0$ are a very good model of the system in the $\{\gamma_1, \gamma_4\}$ range. For $\gamma_5$ the $\varrho_0$ distribution is less reasonable, and only gets worse for $\gamma_6$. As we saw in the Superimposed system, a better choice of our distribution $\varrho$ is necessary in the nonadiabatic regime.

The results for the energy are very similar to the Superimposed model. The overall $\tau$ convergence of our PIMC results appears to follow our SOS results. Similar noise in the low $\tau$ regime is present. In general we see the same effects on the energy as we did with the partition function. From $\gamma_1$ to $\gamma_4$ the $\varrho_0$ distribution is a reasonable model of the system, and the PIMC results match the SOS results. For $\gamma_5$ and $\gamma_6$ the approximation is clearly poor, as the error in the PIMC results is on the order of $40\ \mathrm{kJ\,mol^{-1}}$.

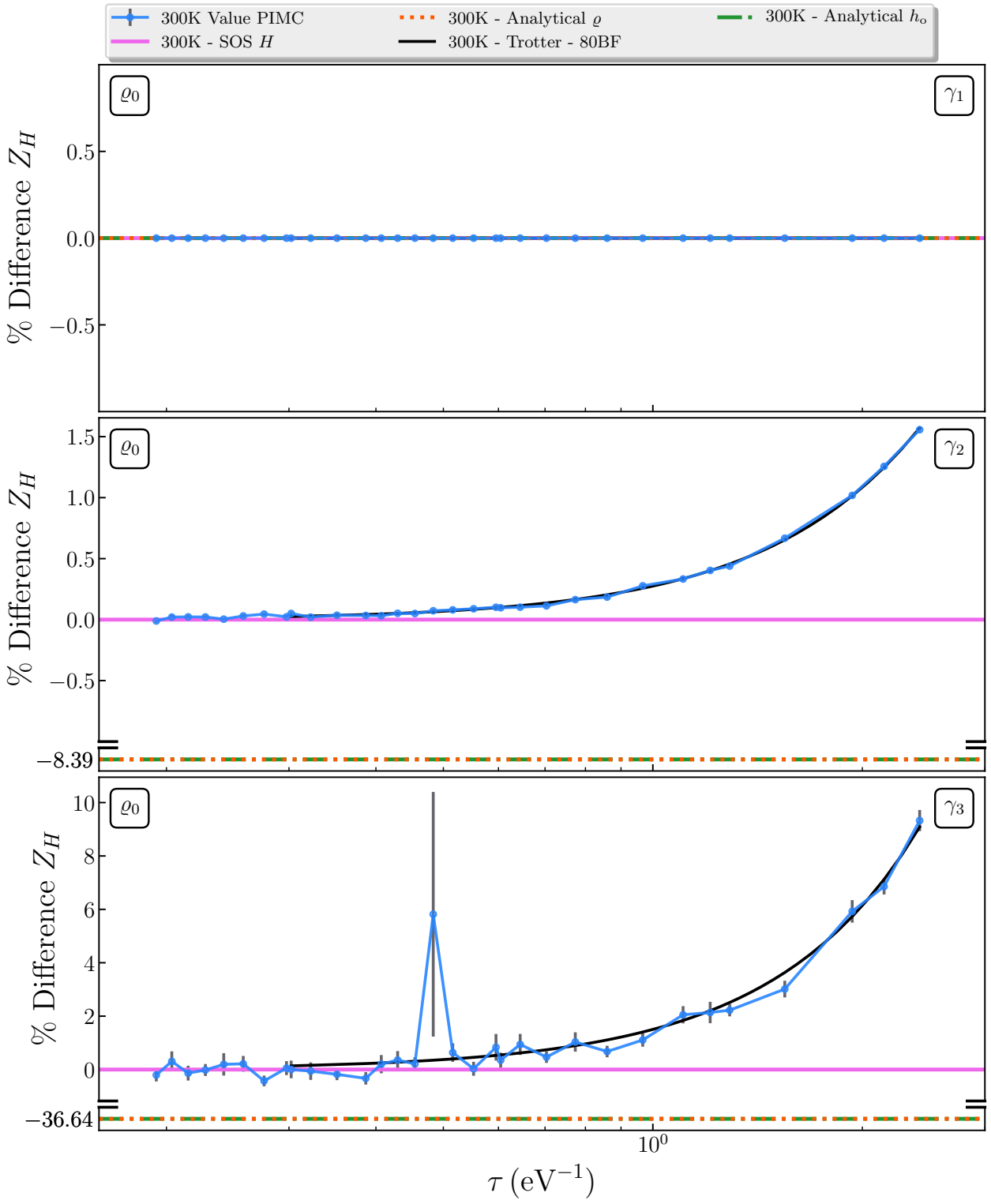


Figure 3.21: PIMC calculation of $Z$ for Displaced system over $\gamma_1 - \gamma_3$ range

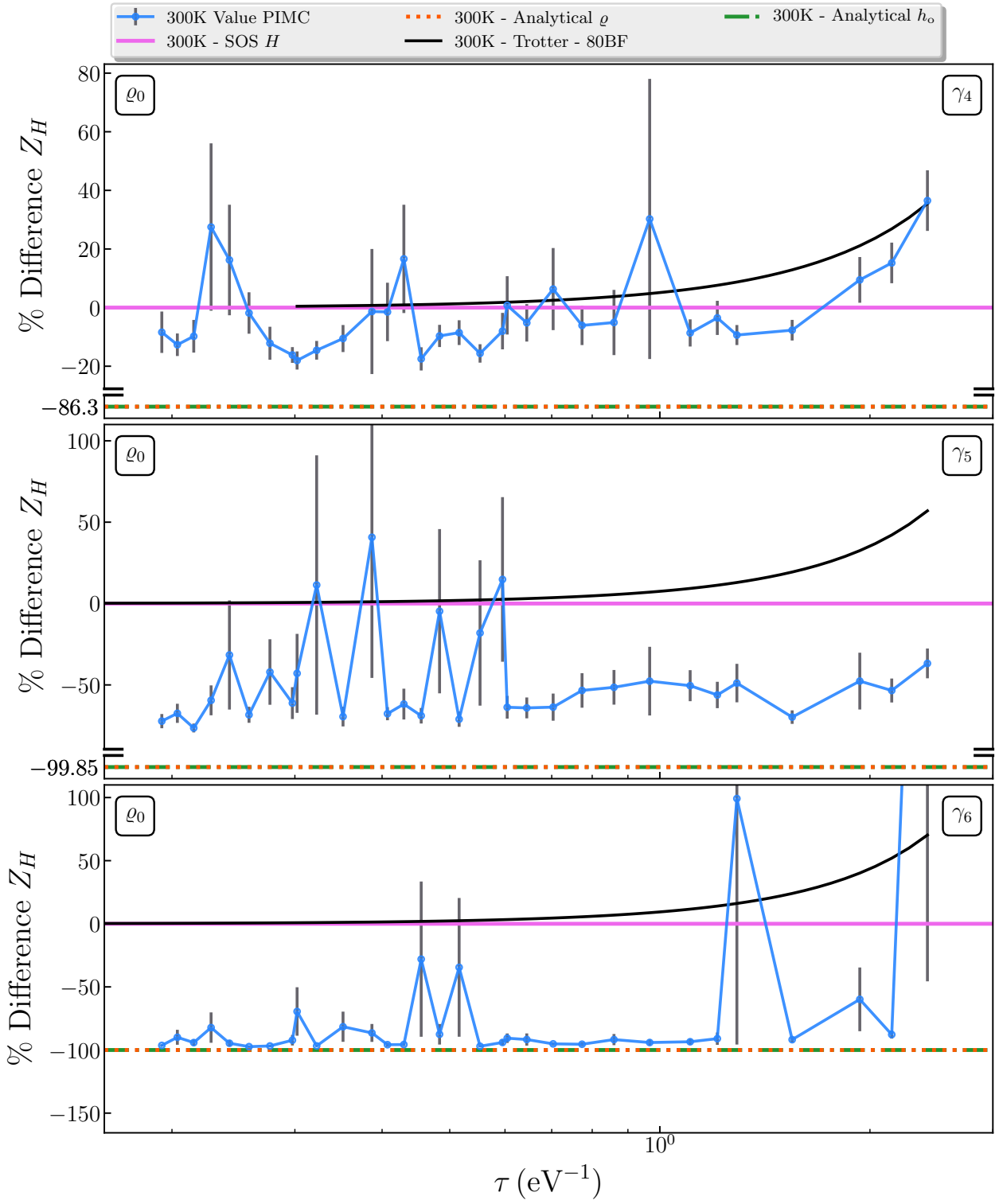


Figure 3.22: PIMC calculation of $Z$ for Displaced system over $\gamma_4 - \gamma_6$ range

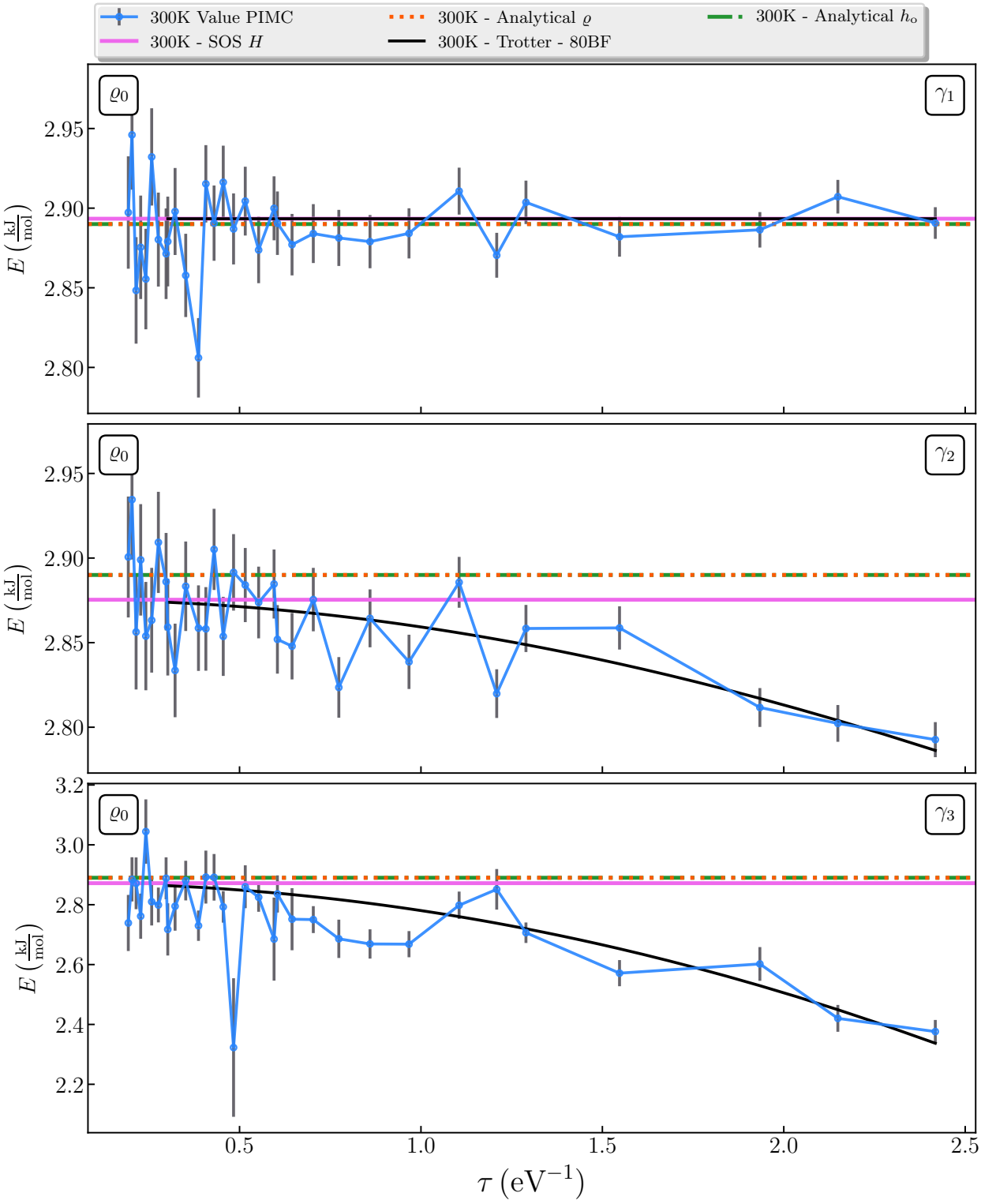


Figure 3.23: PIMC calculation of $E$ for Displaced system over $\gamma_1 - \gamma_3$ range

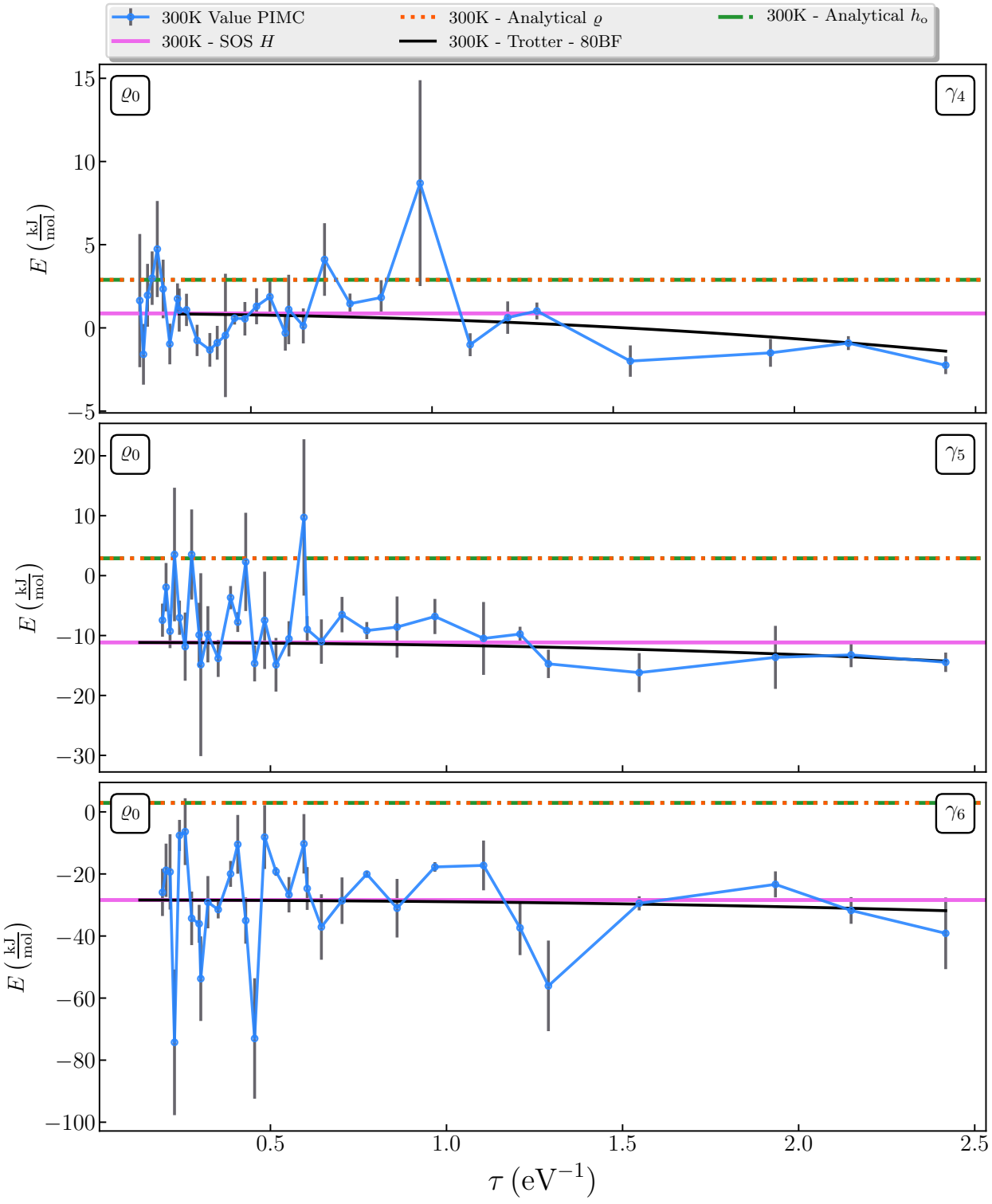


Figure 3.24: PIMC calculation of $E$ for Displaced system over $\gamma_4 - \gamma_6$ range

### Alternative sampling distributions

It is evident that our original choice of $\varrho$

$$\begin{bmatrix} E^a + \mathbf{ho} + \lambda\hat{q}_1 & 0 \\ 0 & E^b + \mathbf{ho} + \lambda\hat{q}_1 \end{bmatrix} \tag{3.8}$$

is a poor description of the Displaced system for $\gamma_5$ and $\gamma_6$. As we increase the coupling parameter $\gamma$, the contribution from the $q_2$ mode increases and we push the system farther into the nonadiabatic regime. The obvious modification to our distribution is to include a $q_2$ term. If the system is in a nonadiabatic regime, then the $q_2$ mode should be the most important contribution. However, because of the mixing of the modes, adding only a $q_2$ term is suboptimal. By looking at Figure 3.18 we can see that a $q_1$ displacement in addition to the $q_2$ displacement would not be the best model for the Displaced system in the $\gamma_5$ and $\gamma_6$ regime. We therefore choose a new distribution, replacing the $q_1$ term with a $q_2$ term:

$$\begin{bmatrix} E^a + \mathbf{ho} + \gamma\hat{q}_2 & 0 \\ 0 & E^b + \mathbf{ho} - \gamma\hat{q}_2 \end{bmatrix} \tag{3.9}$$

Figure 3.25 shows that our new distribution $\varrho_1$ captures the $q_2$ effects in the $\gamma_5$ and $\gamma_6$ regime. In Figure 3.26 we see that our new sampling distribution $\varrho_1$ is a significantly better model of the Displaced system along the $q_2$ mode. Figure 3.27 shows that along the $q_1$ mode $\varrho_0$ is a better model of the Displaced system. Due to the importance of the $q_2$ mode, the reduced accuracy in the description of the $q_1$ mode should not have a noticeable effect on our results. We predict that $\tau$ convergence of $Z$ and $U$ will be improved by using sampling distribution $\varrho_1$ instead of $\varrho_0$.

Figure 3.29 shows an amazing reduction of the stochastic error compared to Figure 3.28. With our improved distribution $\varrho_1$, the error has been reduced from approximately $100\%$ to $1\% \sim 4\%$. This shows that the choice of the sampling distribution dominates the statistical error present in our methodology. We see similar results for the energy when comparing Figure 3.31 and Figure 3.30. There is an error reduction from approximately $80\%$ to $1\% \sim 2\%$. Again we see a energy shift discrepency in out PIMC results. However, the PIMC results and the Trotter results still follow the same trend.

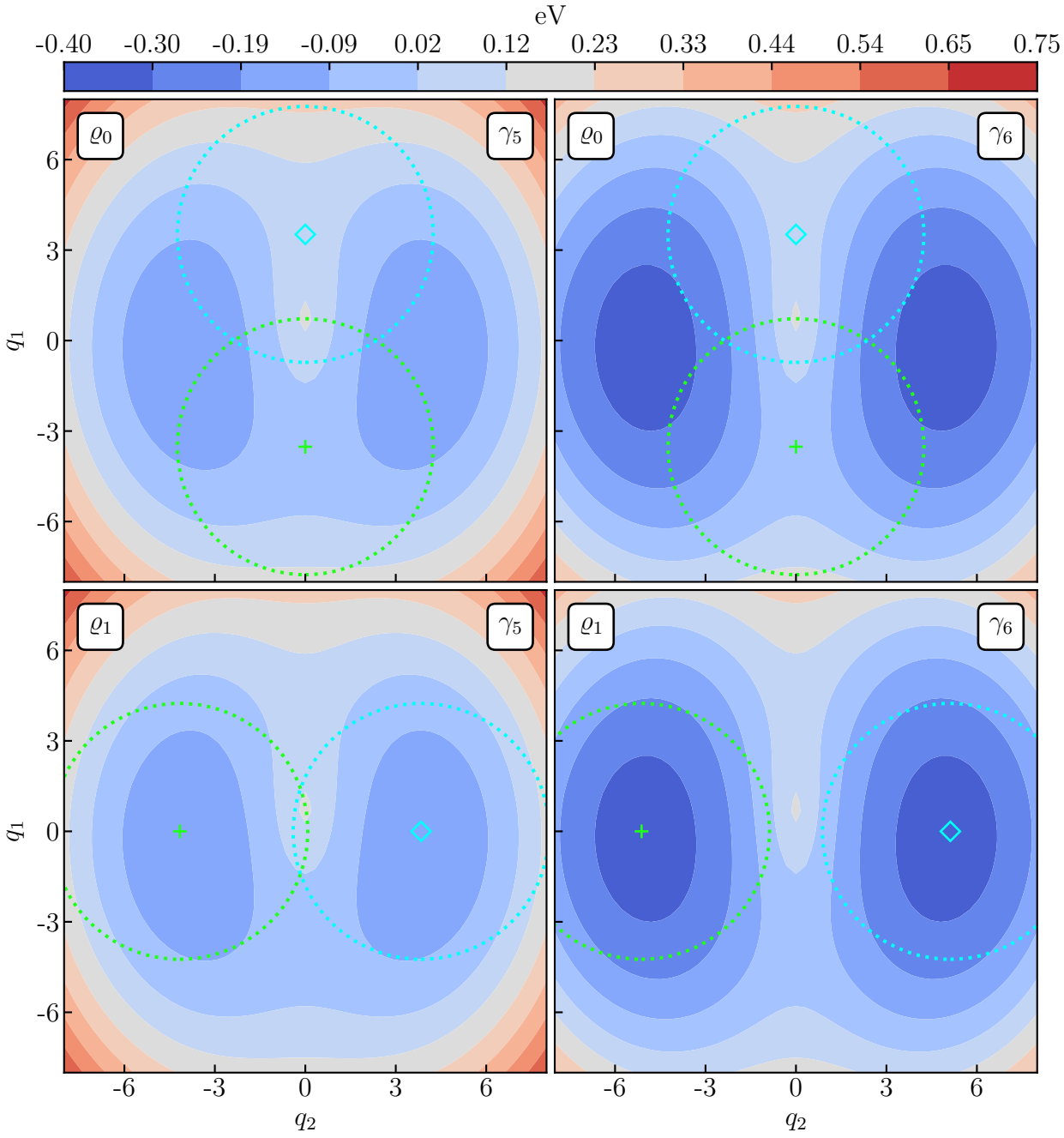


Figure 3.25: Elevation map of lower surface of Displaced system for two choices of $\varrho$

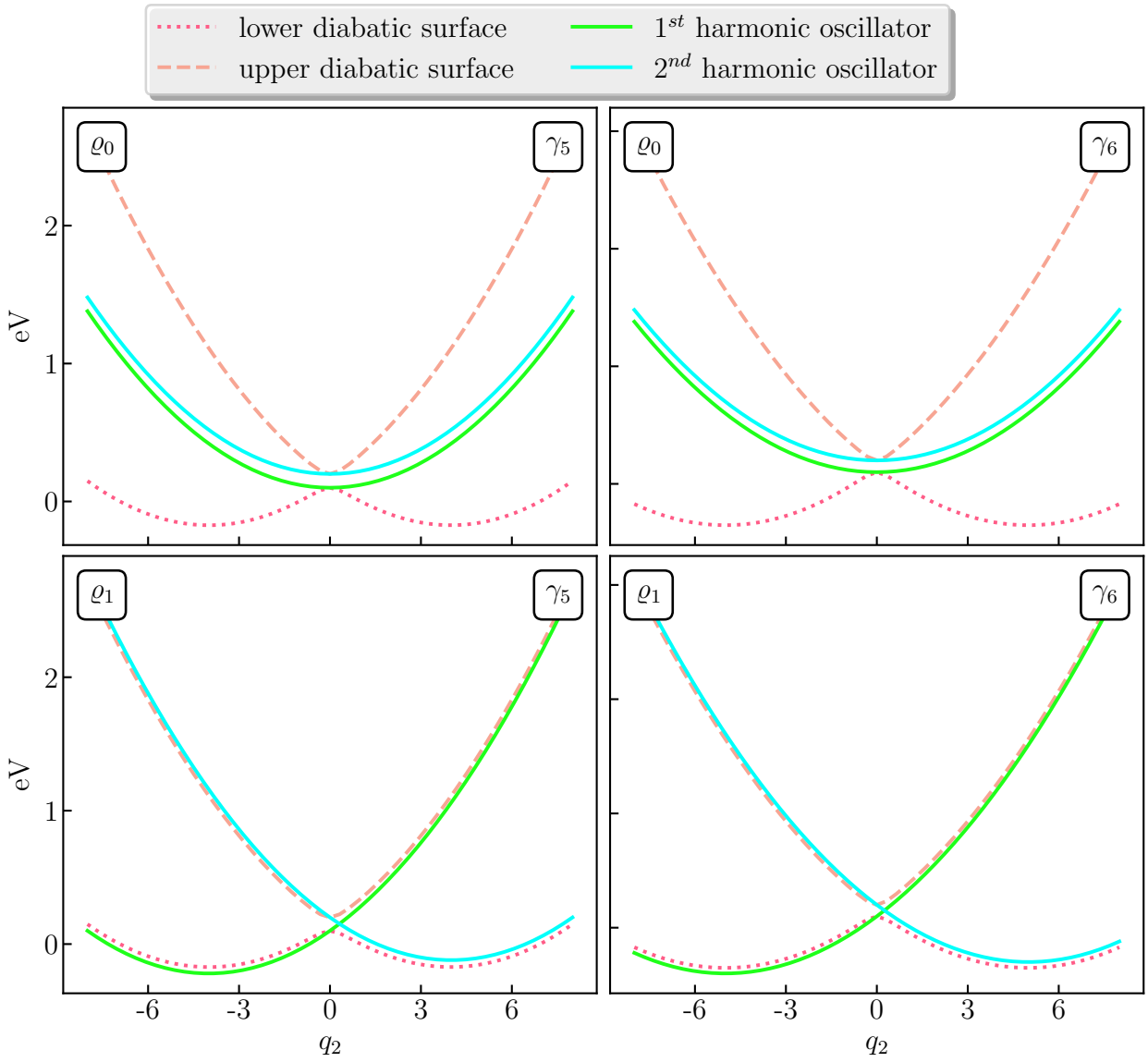


Figure 3.26: $q_2$ slices of Displaced system for two choices of $\varrho$

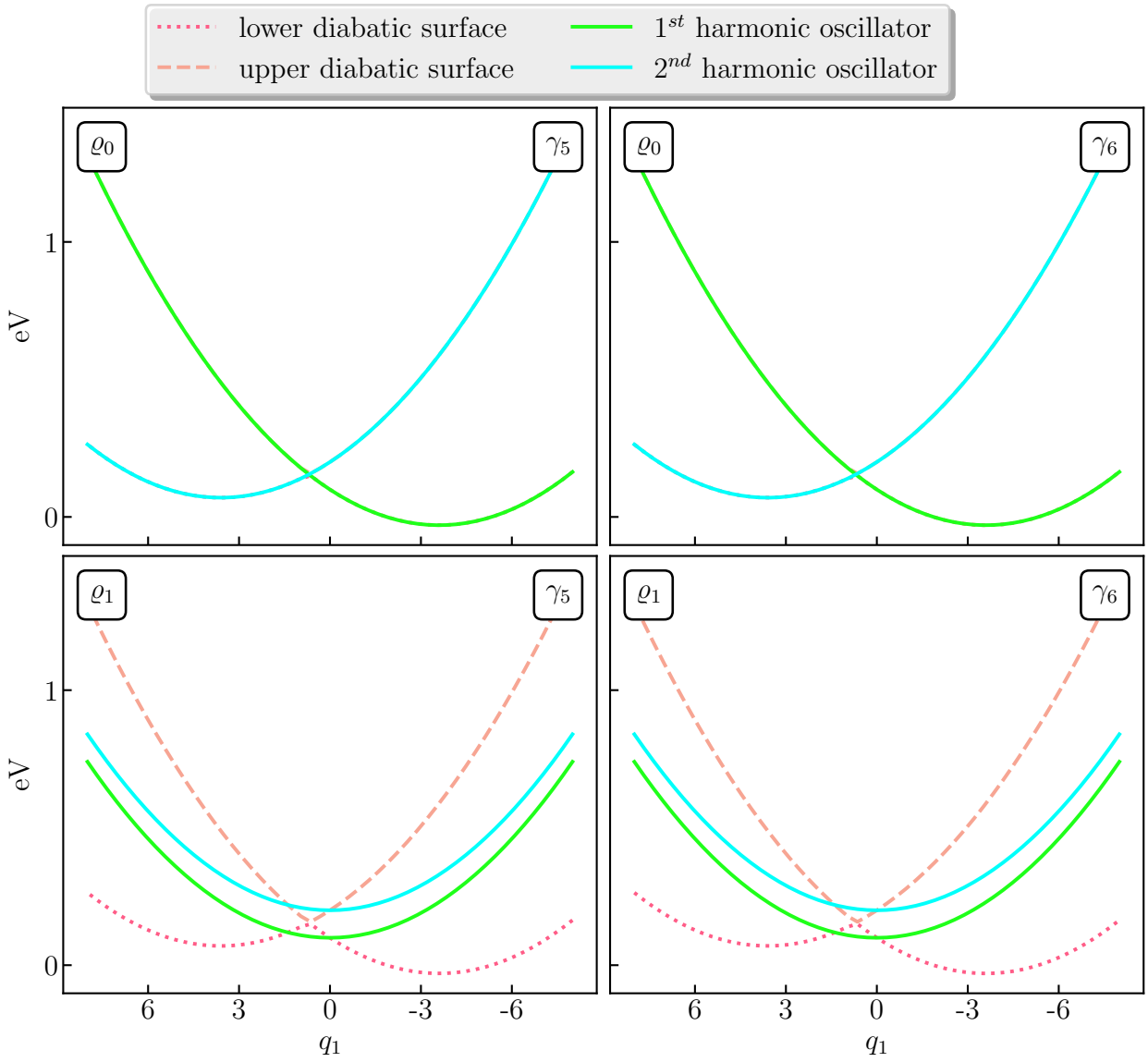


Figure 3.27: $q_1$ slices of Displaced system for two choices of $\varrho$

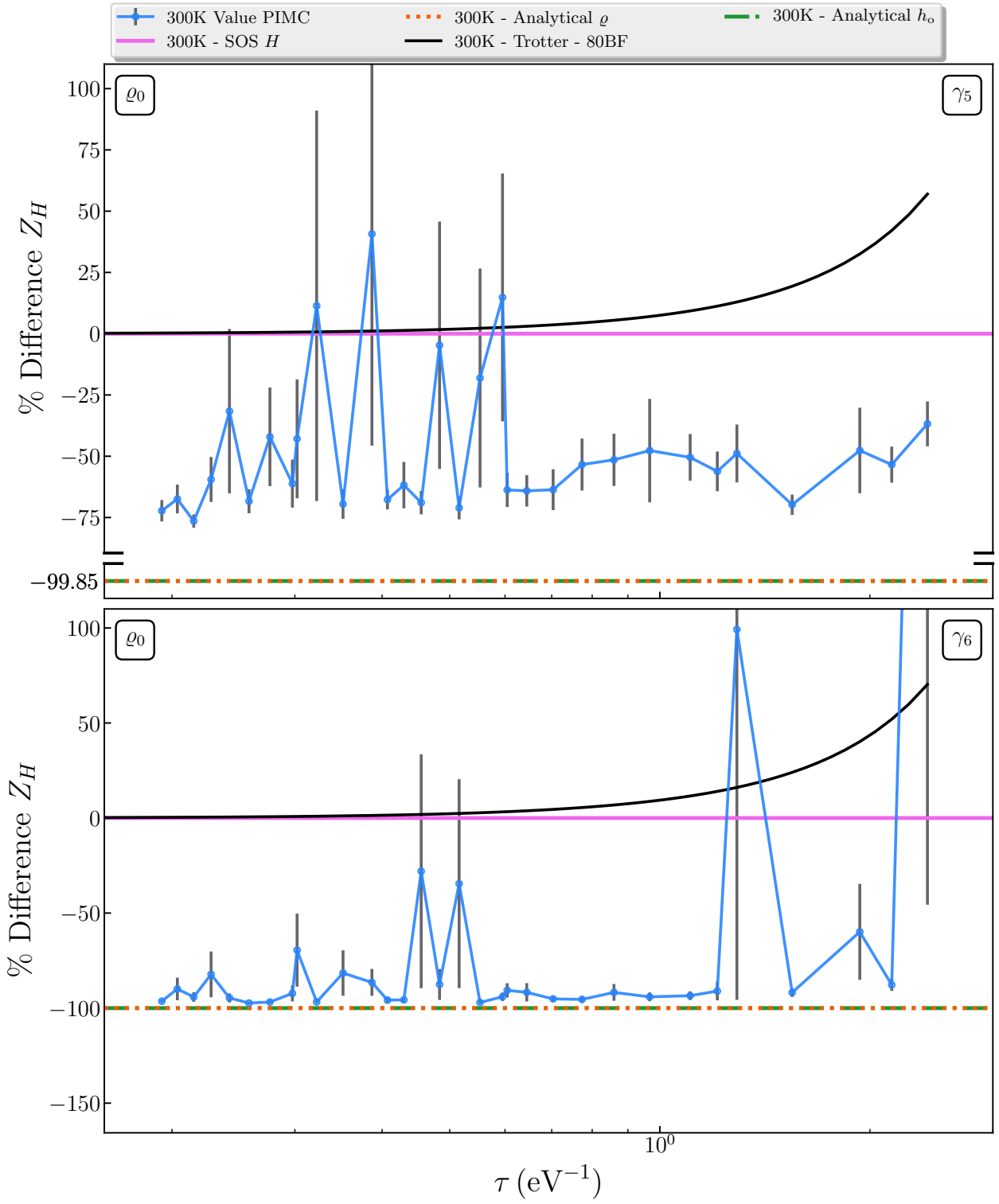


Figure 3.28: PIMC calculation of $Z$ using $\varrho_0$ for Displaced system over $\gamma_5 - \gamma_6$ range

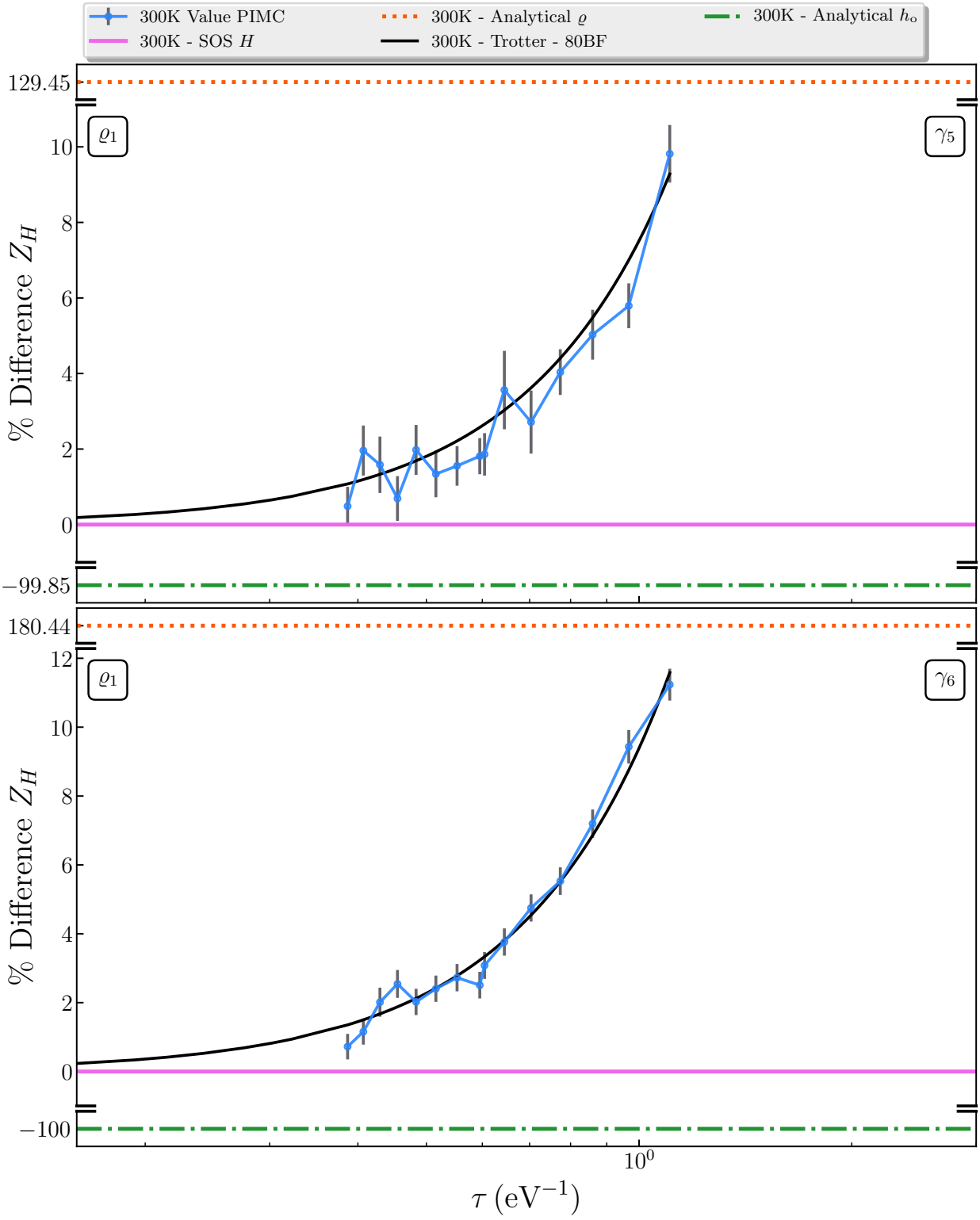


Figure 3.29: PIMC calculation of $Z$ using $\varrho_1$ for Displaced system over $\gamma_5 - \gamma_6$ range

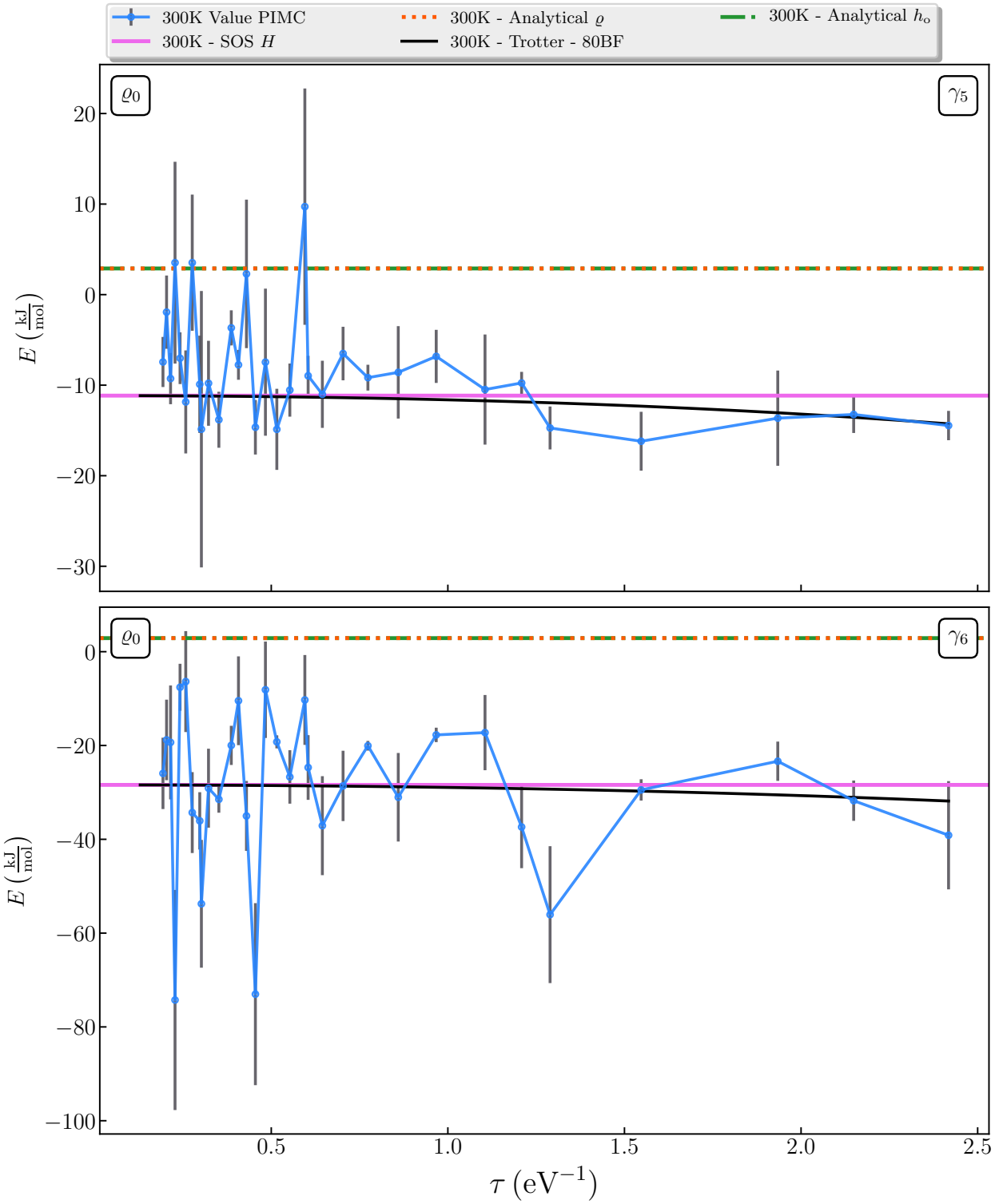


Figure 3.30: PIMC calculation of $E$ using $\varrho_0$ for Displaced system over $\gamma_5 - \gamma_6$ range

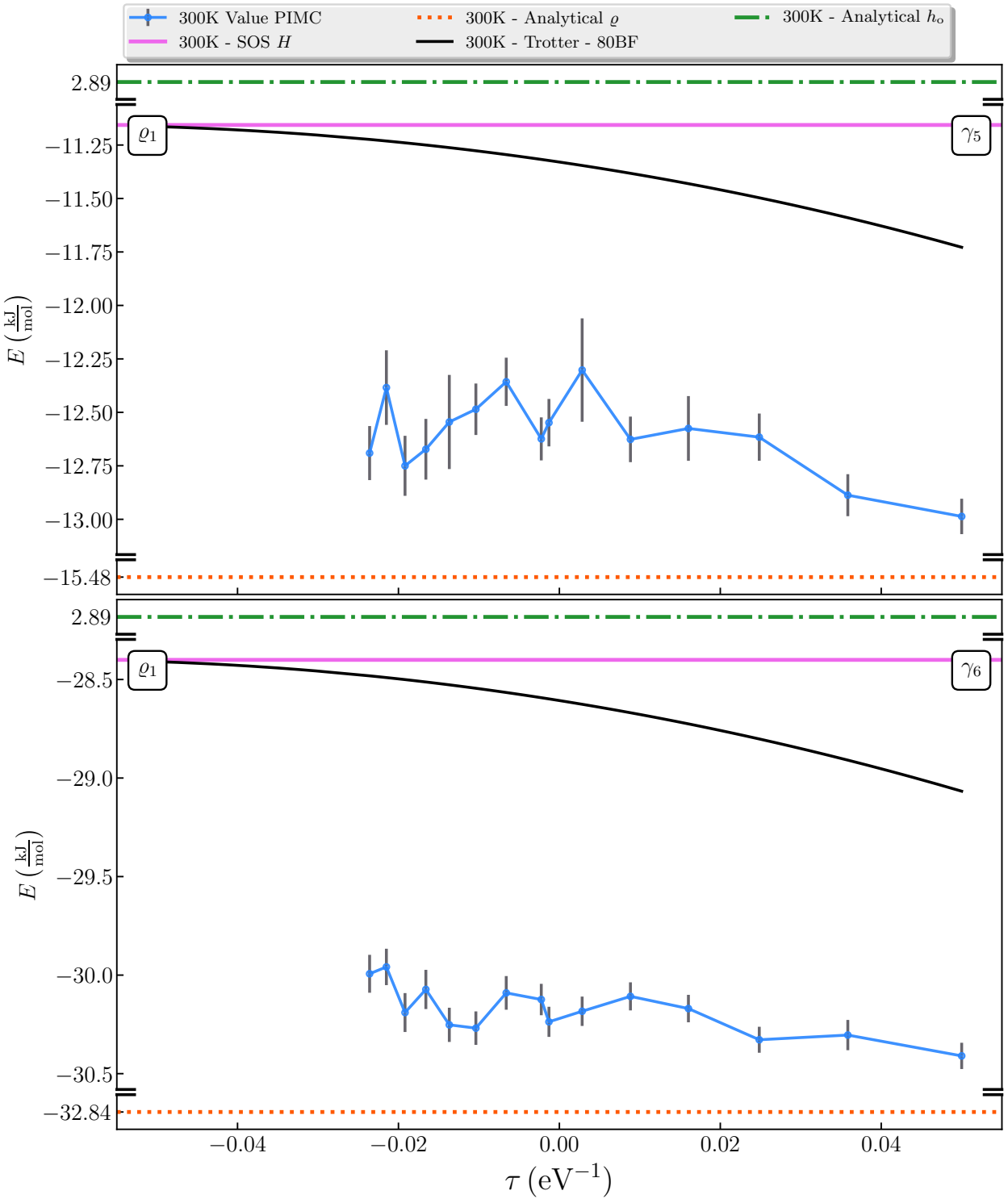


Figure 3.31: PIMC calculation of $E$ using $\varrho_1$ for Displaced system over $\gamma_5 - \gamma_6$ range

## 3.3 Elevated system

This system is described by the following Hamiltonian:

$$\hat{H} = \hat{h}_o + \hat{V} \tag{3.10}$$

$$= \begin{bmatrix} E^a + \mathbf{ho} + \lambda\hat{q}_1 & 0 \\ 0 & E^b + \mathbf{ho} - \lambda\hat{q}_1 \end{bmatrix} + \begin{bmatrix} 0 & \Delta + k\hat{q}_2 \\ \Delta + k\hat{q}_2 & 0 \end{bmatrix} \tag{3.11}$$

Table 3.3: Elevated system parameters

| Parameter | Value/eV | Parameter | Value/eV |
|---|---|---|---|
| $E^a$ | 0.416 87 | $\Delta_1$ | 0.0 |
| $E^b$ | 0.216 87 | $\Delta_2$ | 0.3 |
| $\omega_1$ | 0.02 | $\Delta_3$ | 0.6 |
| $\omega_2$ | 0.04 | $\Delta_4$ | 0.9 |
| $\lambda$ | 0.12 | $\Delta_5$ | 1.2 |
| $k$ | 0.0008 | $\Delta_6$ | 1.5 |

Results are analyzed as a function of $\Delta$, a shift in the energy. At $\Delta_1$ the two PESs are displaced along the $q_1$ axis and the $E$ axis. As we increase $\Delta$ the displacement in the $E$ axis increases, as shown in Figures 3.34 and 3.35. In the previous systems the H.O.s locations hindered sampling. The Elevated system's H.O.s are placed in favourable locations for sampling, evident in Figure 3.33, so we expect the sampling to be less hindered than we saw in the first two systems. This system highlights the effect of a local maximum on the sampling procedure.

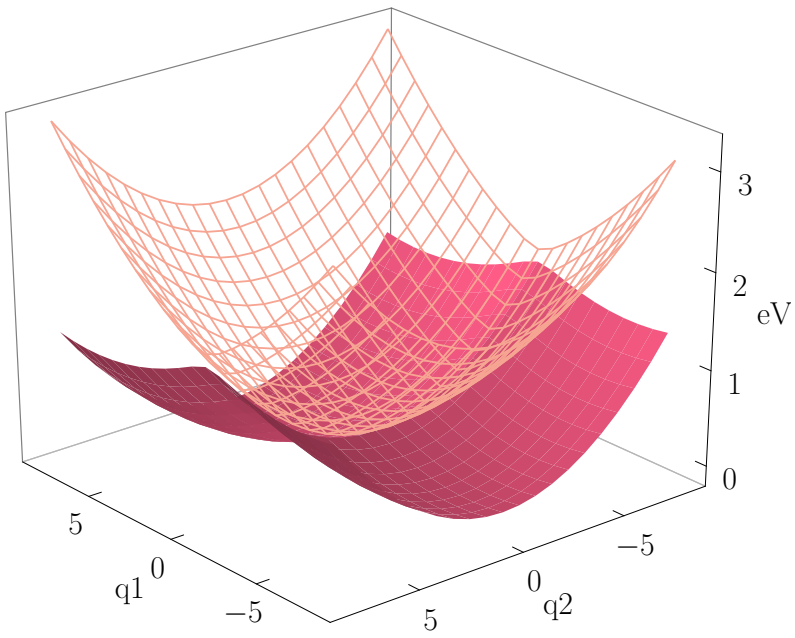


Figure 3.32: Static 3D image of Elevated system

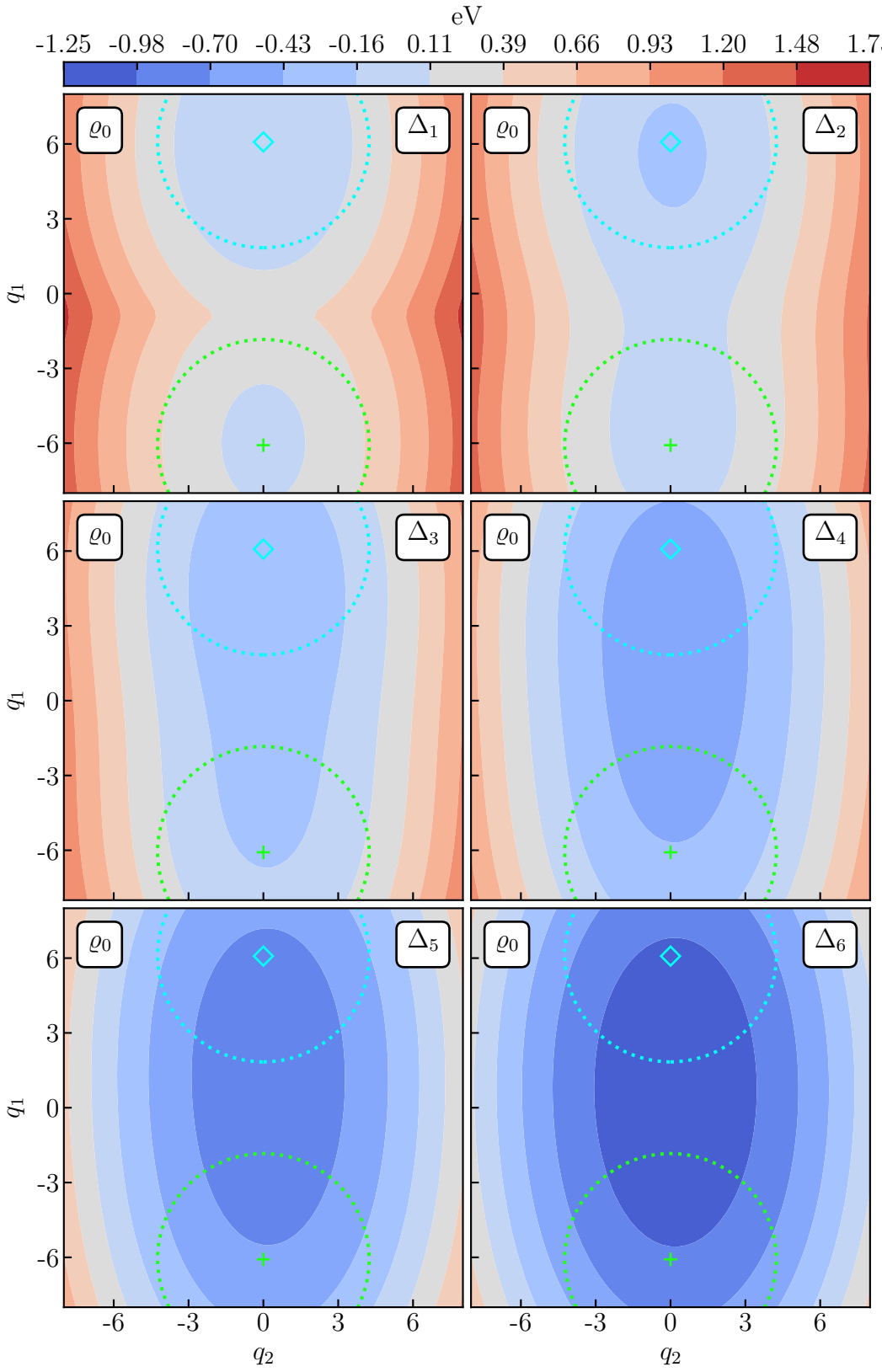


Figure 3.33: Elevation maps of lower surface for Elevated system

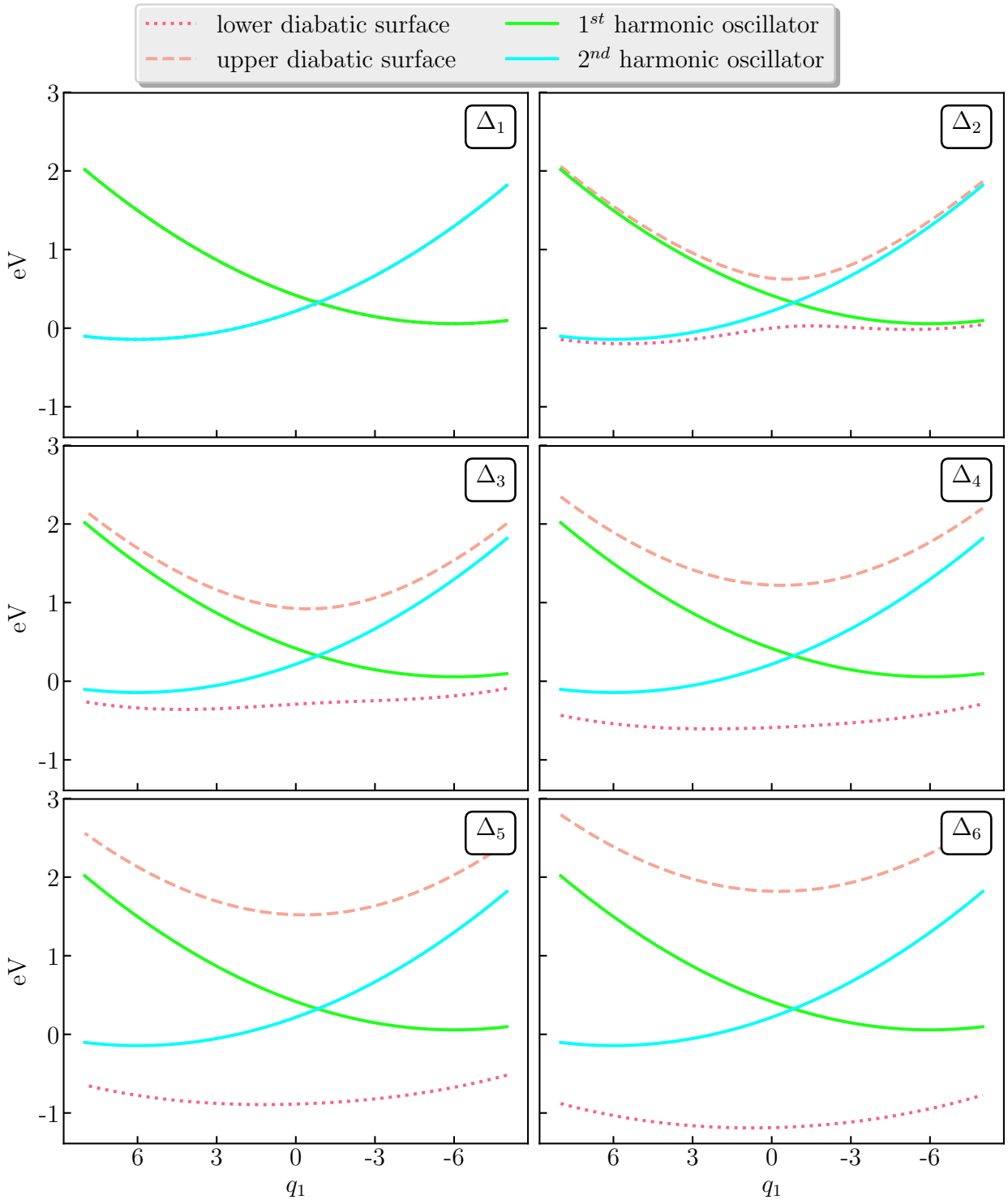


Figure 3.34: $q_1$ slices of Elevated system

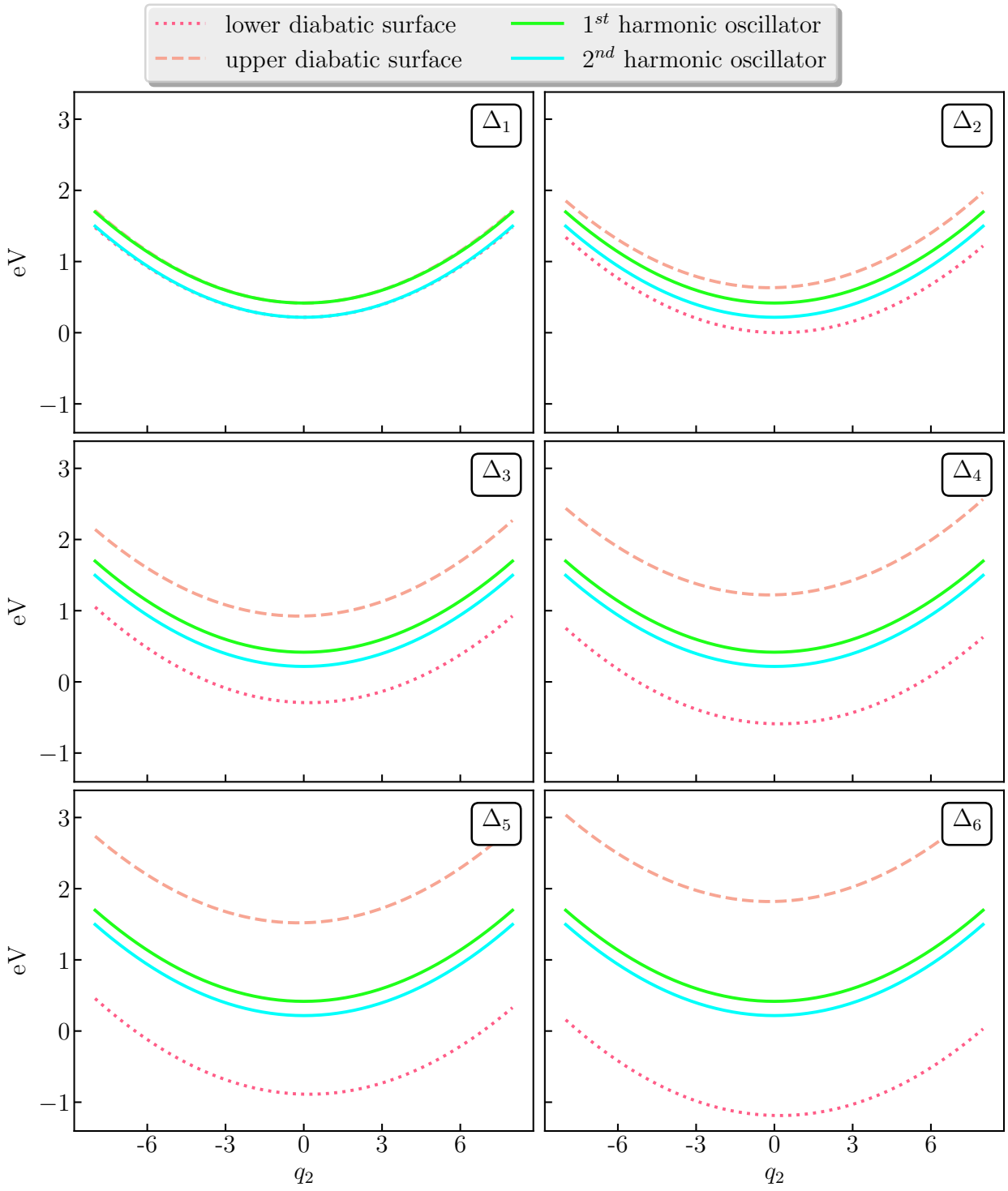


Figure 3.35: $q_2$ slices of Elevated system

### PIMC results

The Elevated system has weak coupling in $\Delta_1$ and is not purely harmonic. We expect the PIMC and Trotter results to converge to the SOS result, as well as to exhibit some difference between the analytical and SOS results. This is what we observe in Figure 3.36.

The Trotter and PIMC results are a better approximation than the analytical results for $\Delta_2$, and their relative accuracy improves as the coupling term increases. This is shown by the discrepancy between the SOS and analytical lines. The analytical system cannot describe the partition function for all non-zero values of $\Delta$.

There are some discrepancies between the Trotter and PIMC results for $\Delta_4$, but the convergence of the PIMC results is still acceptable. A simple weighted linear fit of the PIMC results would closely match the Trotter results. It appears the PIMC results begin to converge under our SOS results for $\Delta_5$ and $\Delta_6$. Looking at Figure 3.33, this trend of converging below the SOS results can be attributed to the flattening of the region between the two oscillators.

As expected, the simple choice of $\varrho$ as $\hat{h}_o$ for the Elevated system preforms much better than the respective choices for the Superimposed and Displaced models. The PIMC results converge extremely far below the target value for both the Superimposed system shown in Figure 3.7, and the Displaced system shown in Figure 3.22. In comparison the Elevated system's convergence is favourable, evident in Figure 3.37.

The results for the energy are very similar to our previous two models. The overall $\tau$ convergence of our PIMC results appears to follow our SOS results. Similar noise in the low $\tau$ regime is present. In general, we see the same effects on the energy as we did with the partition function. A key difference between the Elevated system and the the Superimposed and Displaced systems is a smaller standard error for the majority of the PIMC results for $U$. We hypothesise this reduction in error is due to the reduced complexity of the PES in the Elevated system.

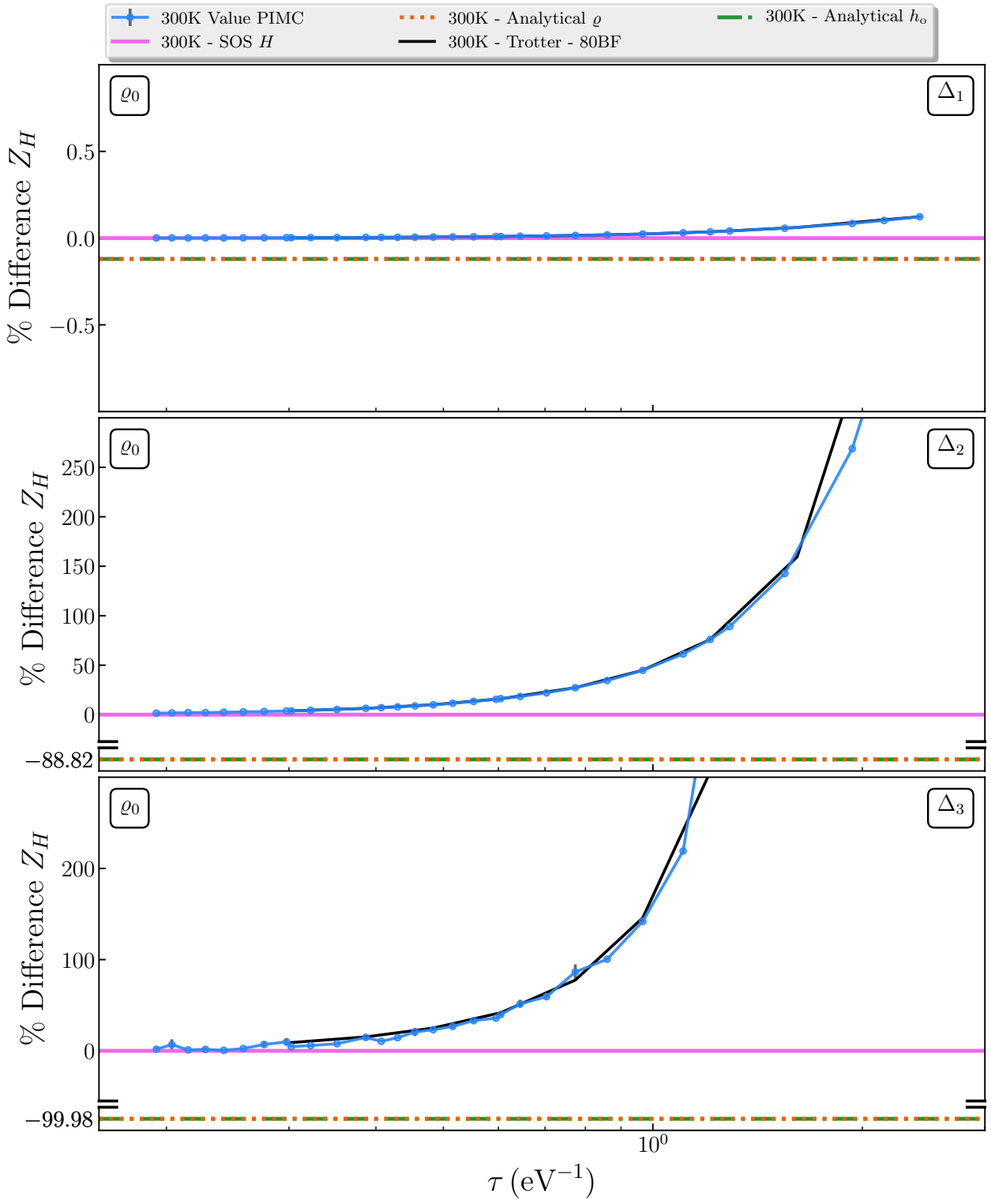


Figure 3.36: PIMC calculation of $Z$ for Elevated system over $\Delta_1 - \Delta_3$ range

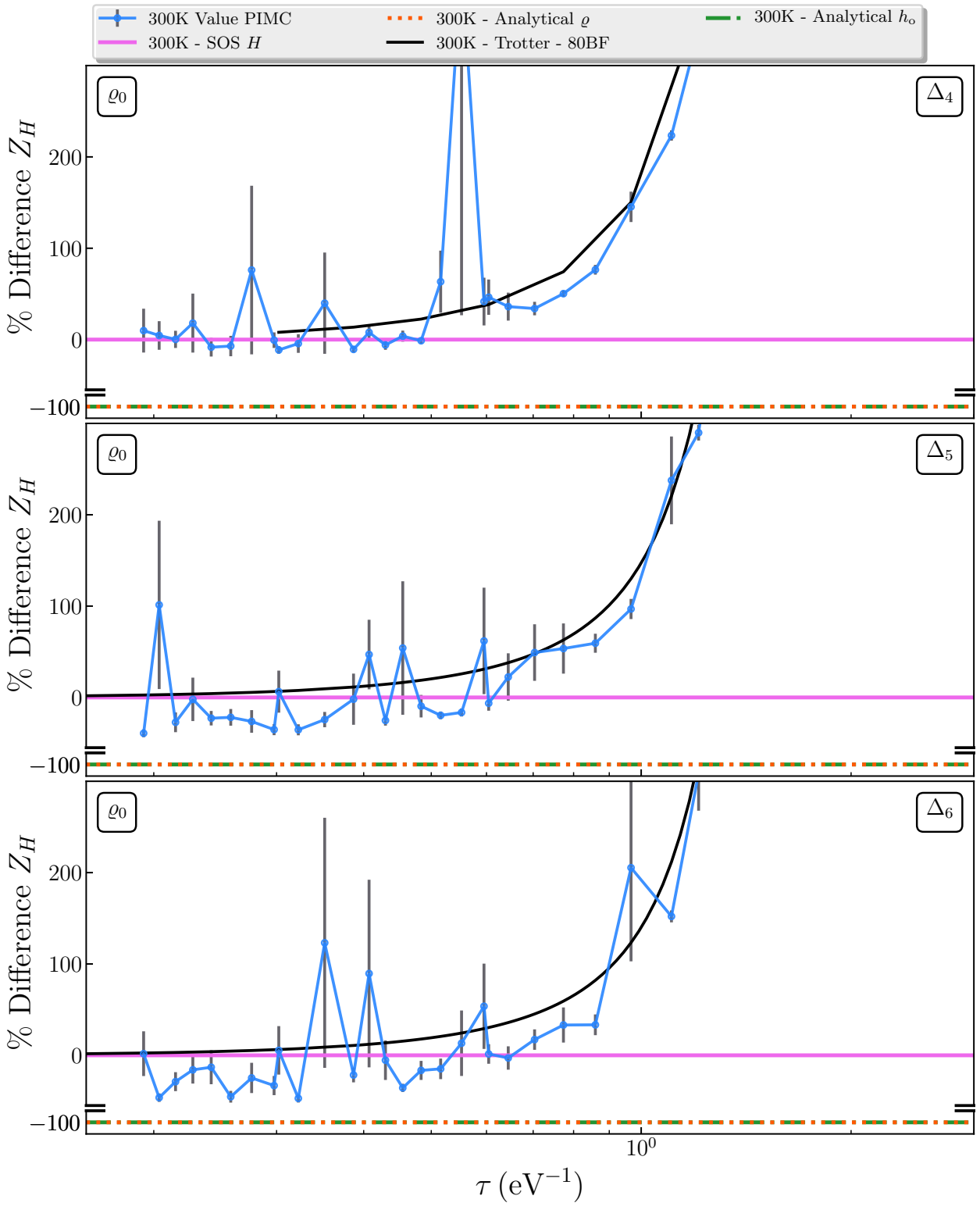


Figure 3.37: PIMC calculation of $Z$ for Elevated system over $\Delta_4 - \Delta_6$ range

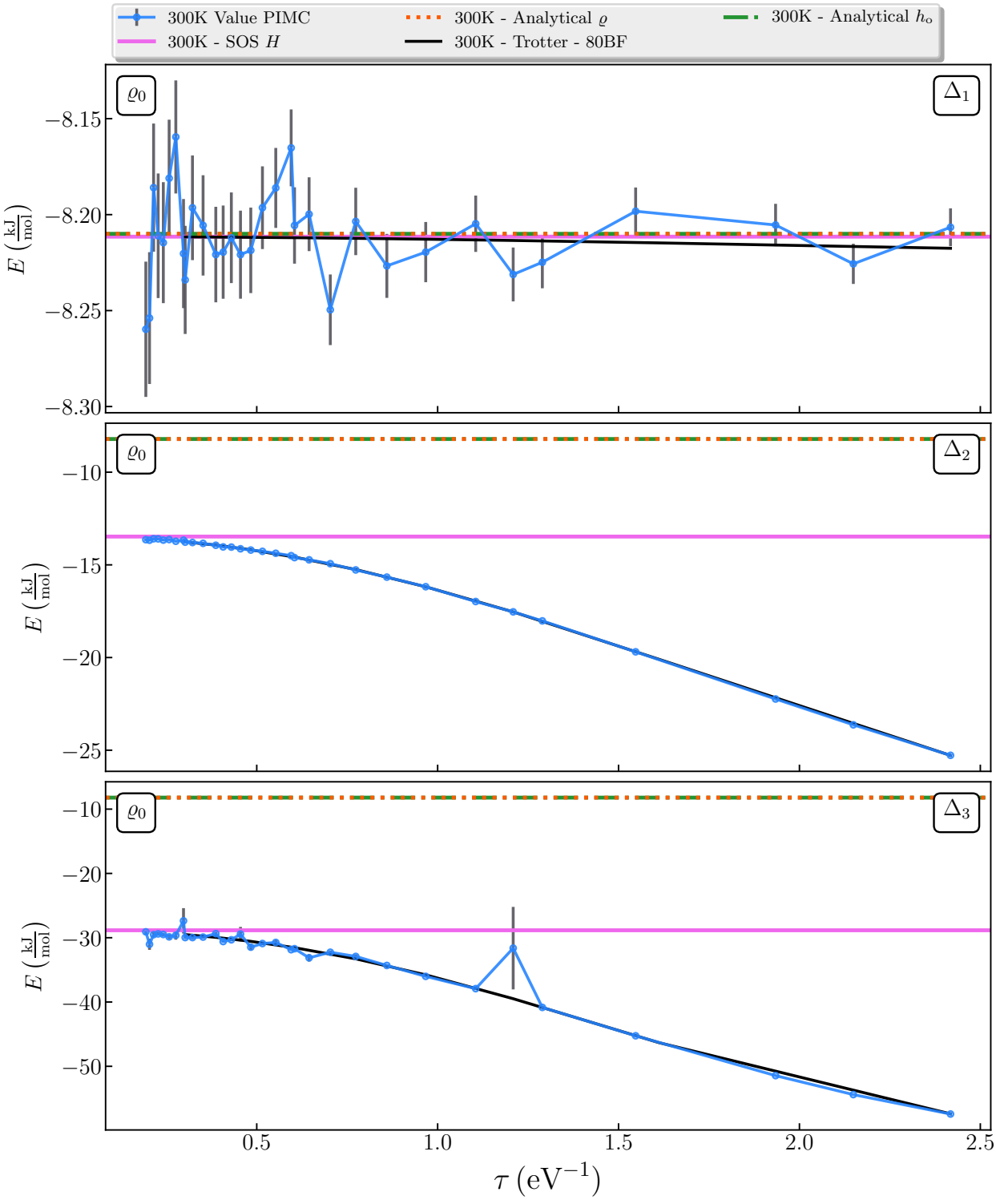


Figure 3.38: PIMC calculation of $E$ for Elevated system over $\Delta_1 - \Delta_3$ range

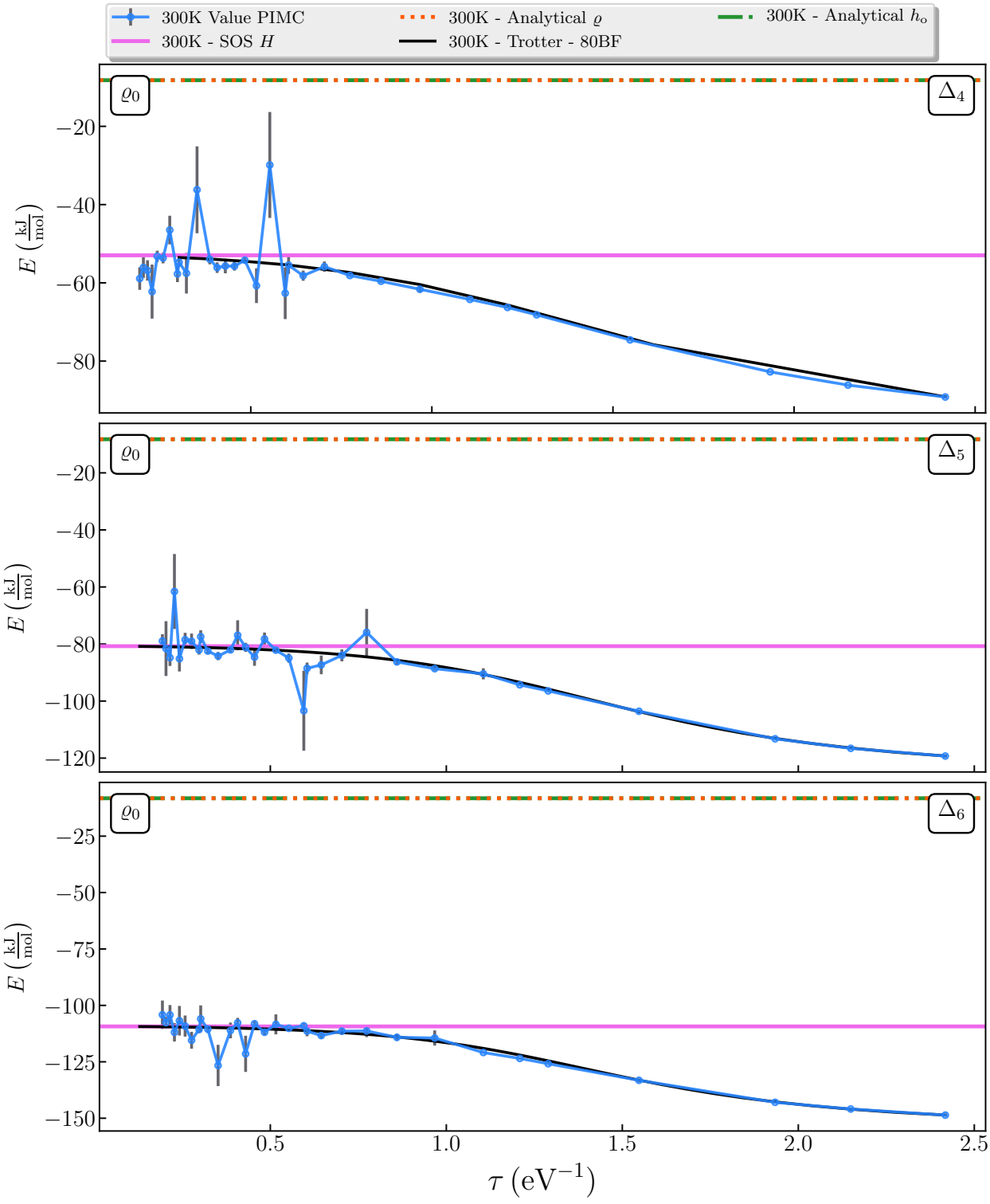


Figure 3.39: PIMC calculation of $E$ for Elevated system over $\Delta_4 - \Delta_6$ range

### Alternative sampling distributions

The default choice of $\varrho$

$$\begin{bmatrix} E^a + \mathbf{ho} + \lambda\hat{q}_1 & 0 \\ 0 & E^b + \mathbf{ho} + \lambda\hat{q}_1 \end{bmatrix} \tag{3.12}$$

is a fairly good description for the Elevated system over the entire range of $\Delta$. We are interested in how important the off-diagonal terms are in this system. Does increasing the energy shift parameter $\Delta$ push the system into a nonadiabatic regime? In the previous systems, adding or replacing a term was sufficient to generate significant improvement. However, here the oscillators are already placed in reasonable locations. So we consider a new distribution where we include the weak $\hat{q}_2$ effects:

$$\begin{bmatrix} E^a + \mathbf{ho} + \lambda\hat{q}_1 + k\hat{q}_2 & 0 \\ 0 & E^b + \mathbf{ho} - \lambda\hat{q}_1 - k\hat{q}_2 \end{bmatrix} \tag{3.13}$$

$\lambda$, $k$ and $\omega$ have the same values, but we choose $E^a = 0.53$ eV, $E^b = 0.31$ eV. The energy shifts are chosen so that the zero of energy of the distribution is $0$ eV. Our new distribution for $\Delta_5$ and $\Delta_6$ is shown in Figure 3.40. The inclusion of the $q_2$ mode appears to have made no significant change. When examining **??** and **??** we seen similar miniscule effects. We expect that the PIMC results for $Z$ and $U$ should be similar for both distributions $\varrho_0$ and $\varrho_1$. This is what we see when comparing Figure 3.43 and Figure 3.44 as well as Figure 3.45 and Figure 3.46. Again, we see a energy shift discrepency in our PIMC results. What we see here is that simply modifying the H.O.s that comprise $\varrho$ is not always effective.

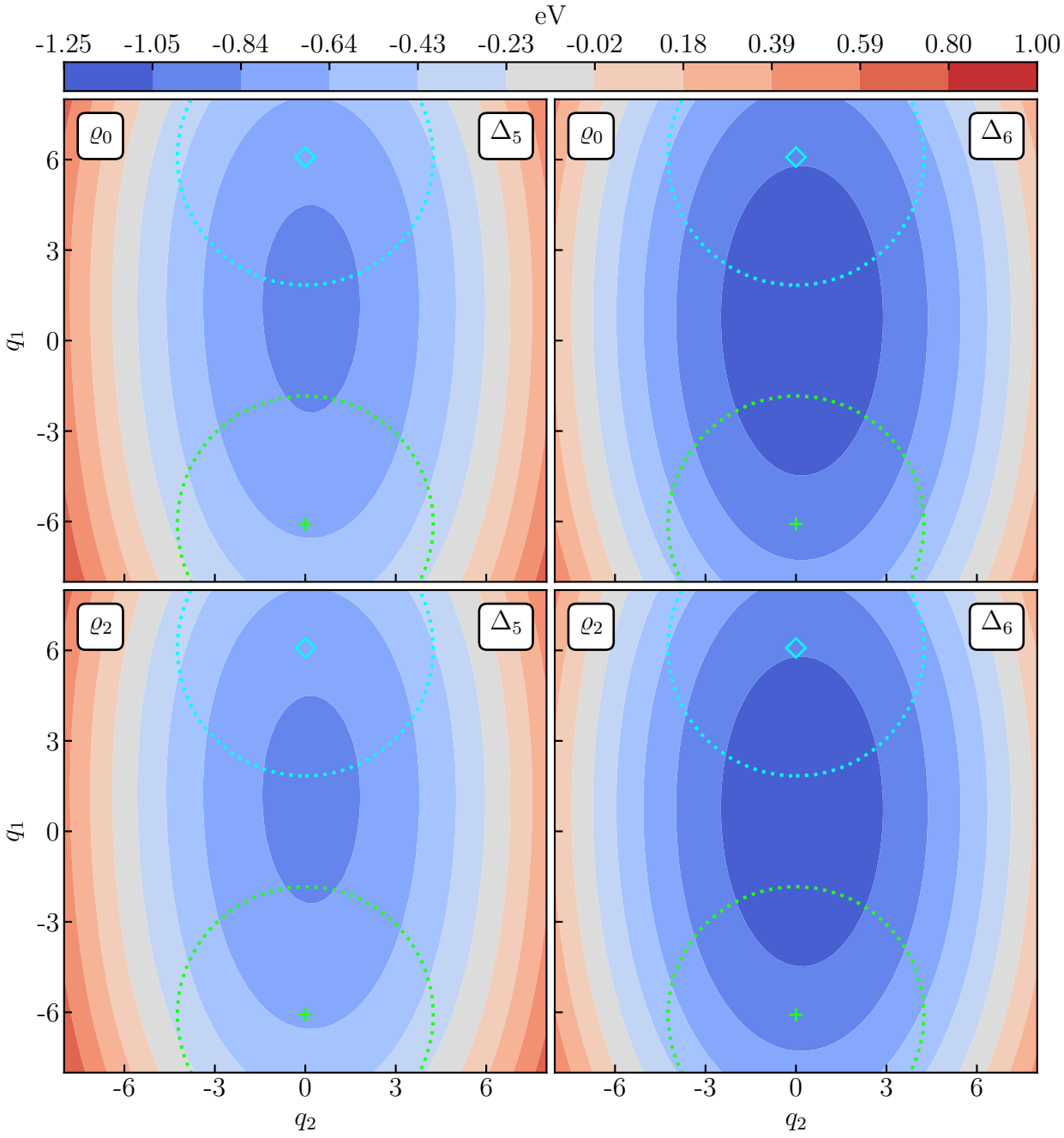


Figure 3.40: Elevation map of lower surface of Elevated system for two choices of $\varrho$

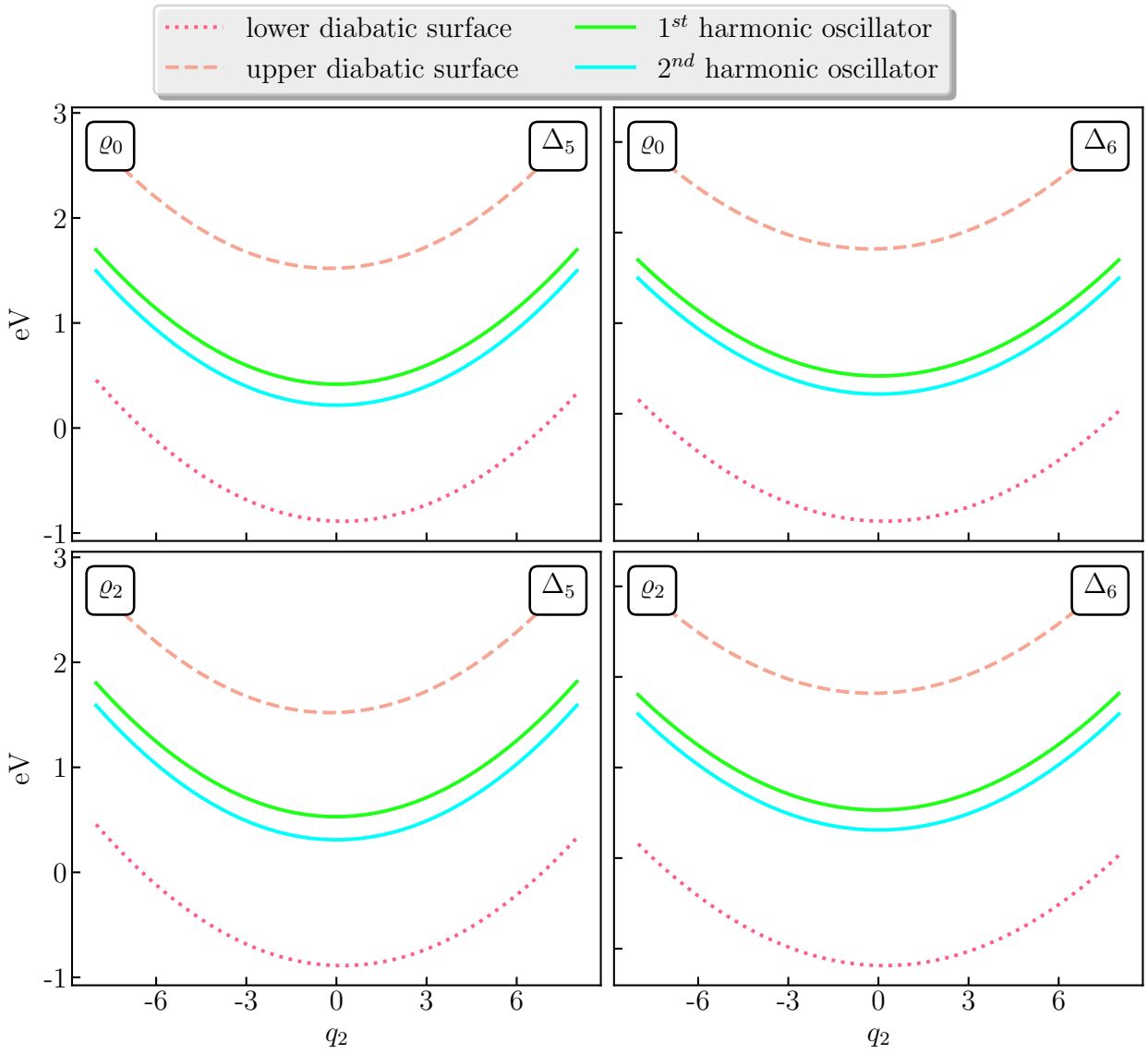


Figure 3.41: $q_2$ slices of Elevated system for two choices of $\varrho$

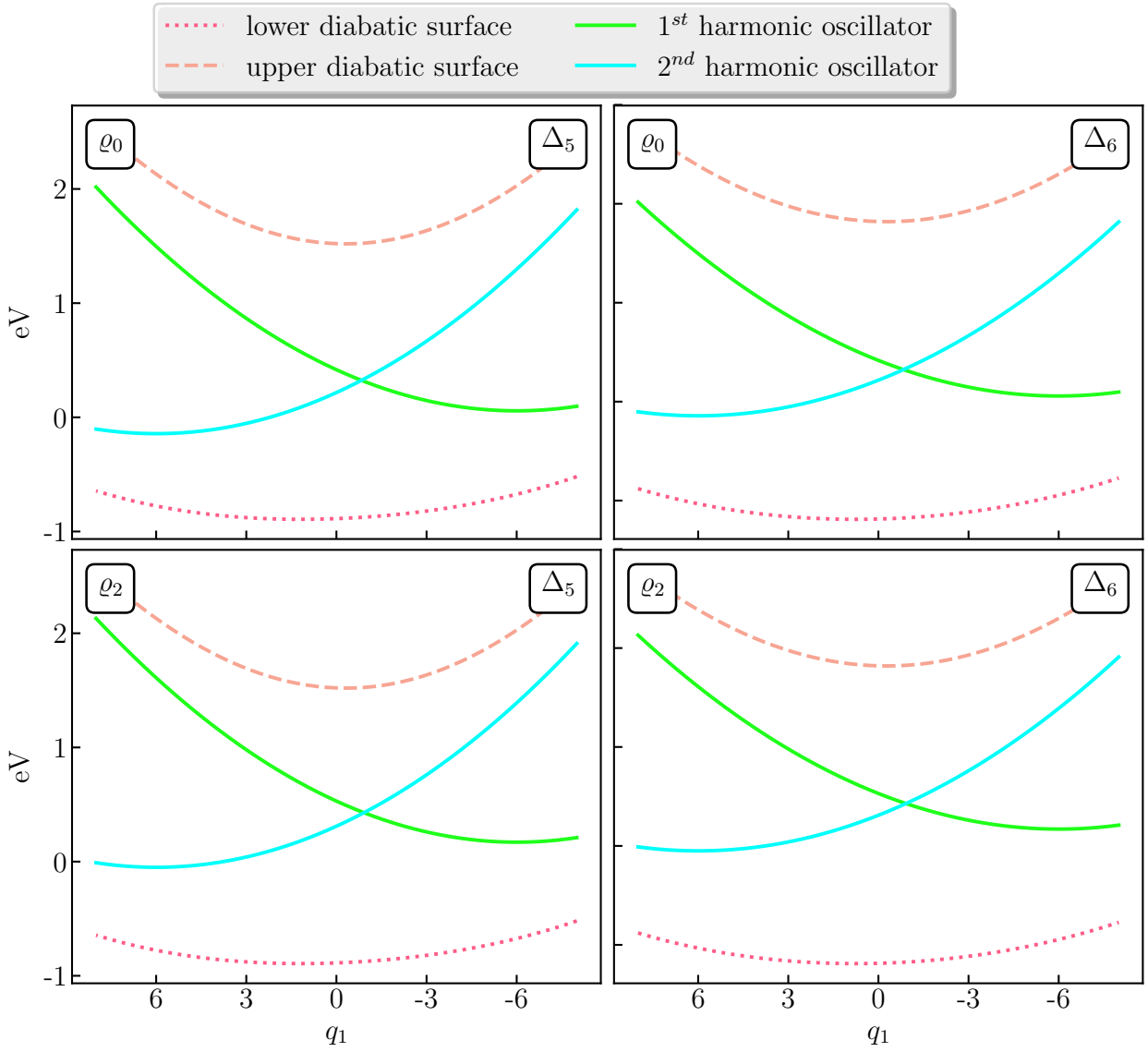


Figure 3.42: $q_1$ slices of Elevated system for two choices of $\varrho$

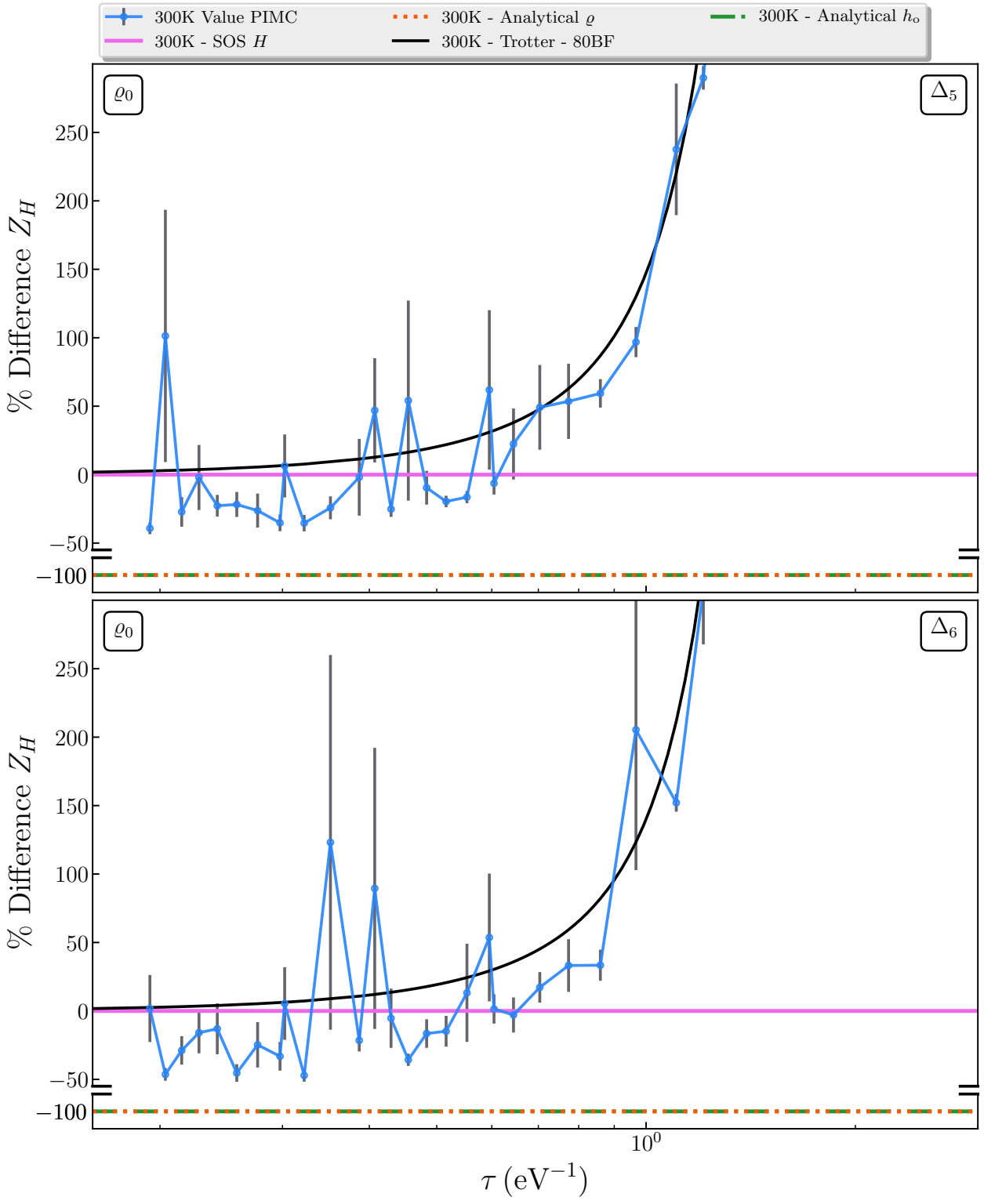


Figure 3.43: PIMC calculation of $Z$ using $\varrho_0$ for Elevated system over $\lambda_5 - \lambda_6$ range

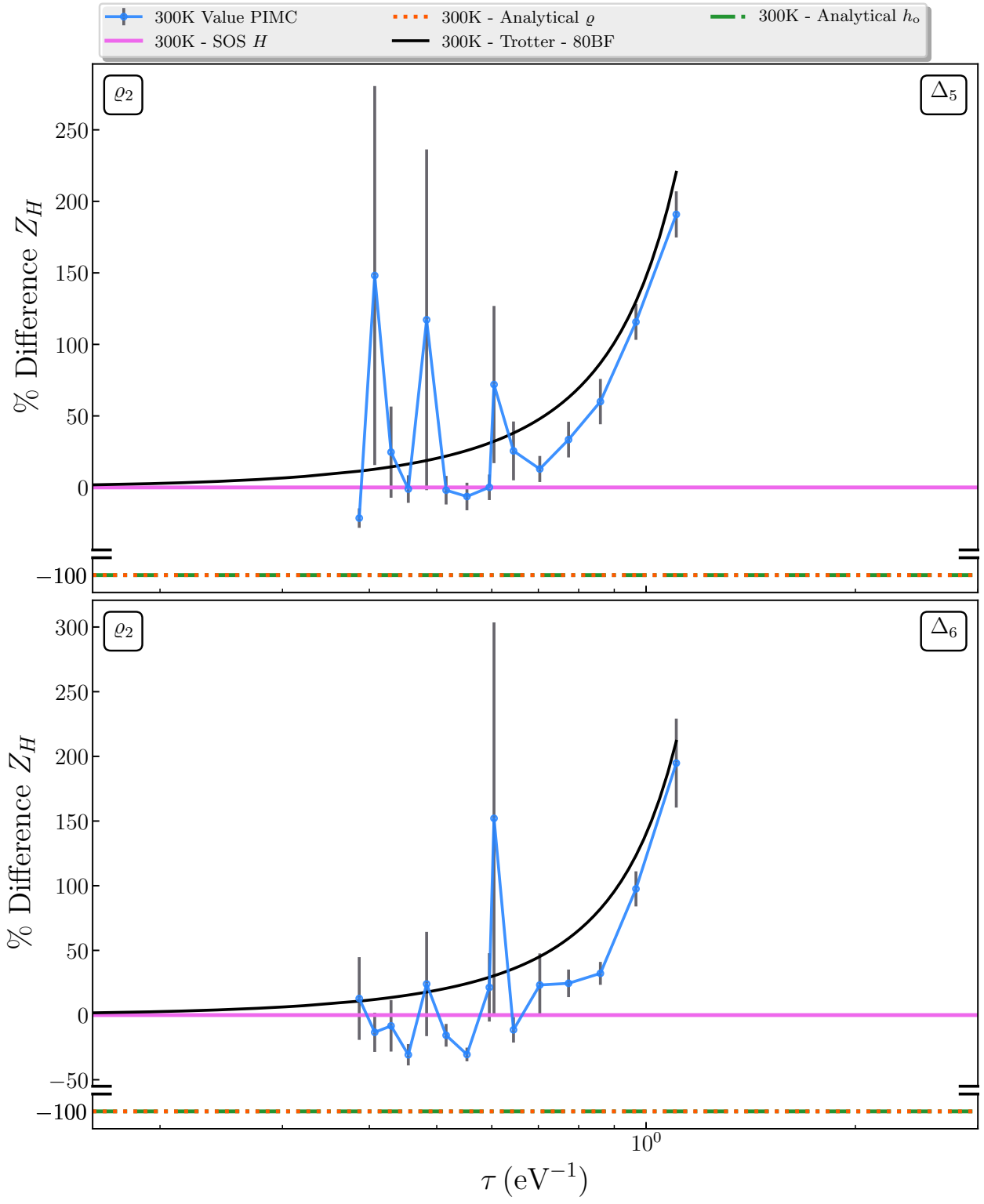


Figure 3.44: PIMC calculation of $Z$ using $\varrho_2$ for Elevated system over $\lambda_5 - \lambda_6$ range

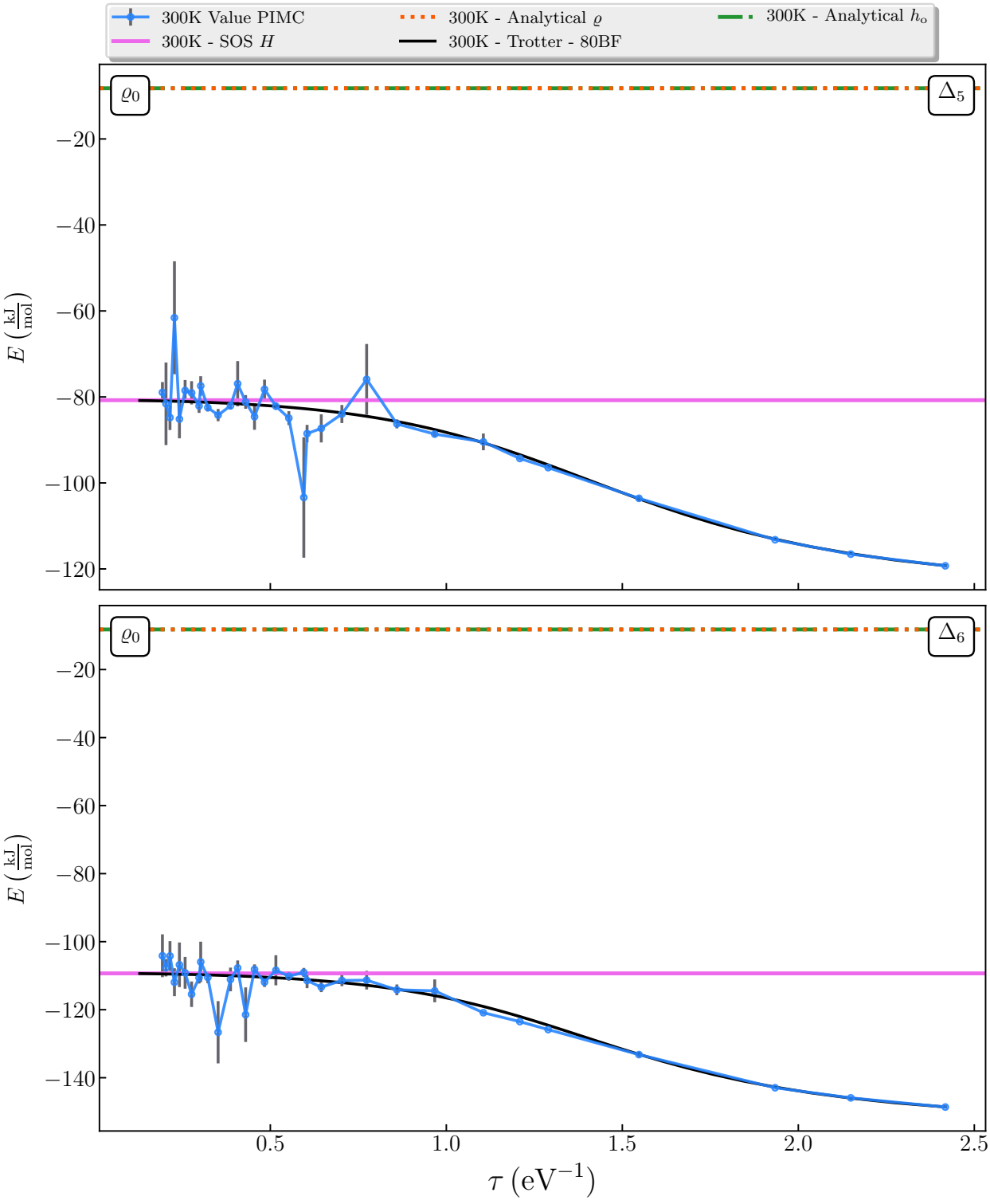


Figure 3.45: PIMC calculation of $E$ using $\varrho_0$ for Elevated system over $\lambda_5 - \lambda_6$ range

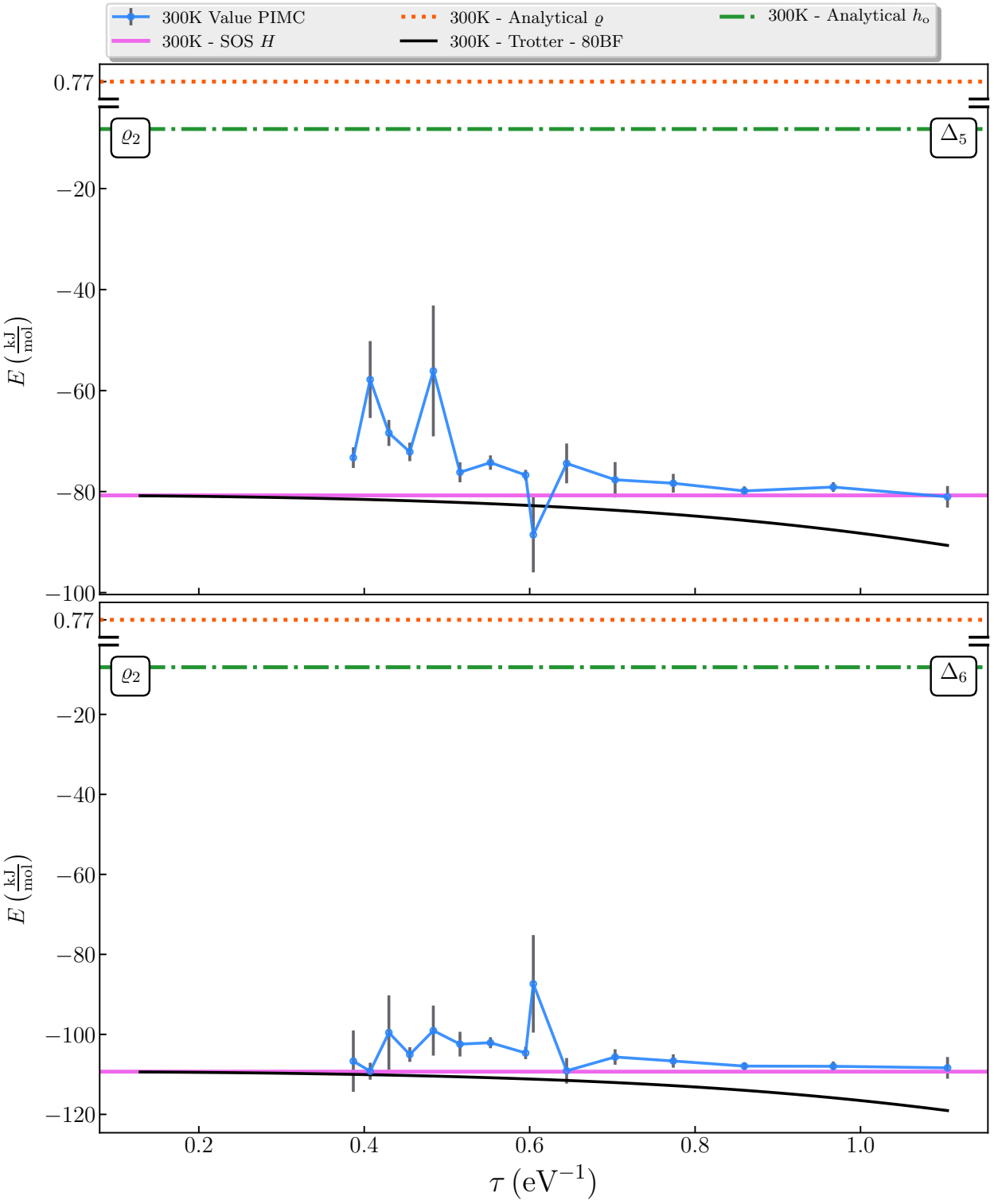


Figure 3.46: PIMC calculation of $E$ using $\varrho_2$ for Elevated system over $\lambda_5 - \lambda_6$ range

## 3.4 Jahn-Teller system

This system is described by the following Hamiltonian:

$$\hat{H} = \hat{h}_o + \hat{V} \tag{3.14}$$

$$= \begin{bmatrix} E + \mathbf{ho} + \lambda\hat{q}_1 & 0 \\ 0 & E + \mathbf{ho} - \lambda\hat{q}_1 \end{bmatrix} + \begin{bmatrix} 0 & \lambda\hat{q}_2 \\ \lambda\hat{q}_2 & 0 \end{bmatrix} \tag{3.15}$$

Table 3.4: Jahn-Teller system parameters

| Parameter | Value/eV | Parameter | Value/eV |
|---|---|---|---|
| $E_1$ | −0.029 99 | $\lambda_1$ | 0.00 |
| $E_2$ | −0.003 33 | $\lambda_2$ | 0.04 |
| $E_3$ | 0.076 66 | $\lambda_3$ | 0.08 |
| $E_4$ | 0.209 99 | $\lambda_4$ | 0.12 |
| $E_5$ | 0.396 67 | $\lambda_5$ | 0.16 |
| $E_6$ | 0.631 35 | $\lambda_6$ | 0.20 |
| $\omega_1$ | 0.03 | $\omega_2$ | 0.03 |

Results are analyzed as a function of $\lambda$, the linear term. $E$ was chosen so that the ground state energy $\approx 0$. For $\lambda_i$ where $i > 1$, this system has the form of an inverted second Hermitian polynomial rotated around the origin. As we increase $\lambda$, the curvature of the well increases, as shown in Figure 3.49 and Figure 3.50. Note that for $\lambda_2$ and $\lambda_3$ in Figure 3.48, the apparent lack of a well is a byproduct of the 2D projection and the choice of axes. In Figure 3.49 and Figure 3.50 the well is clearly present.

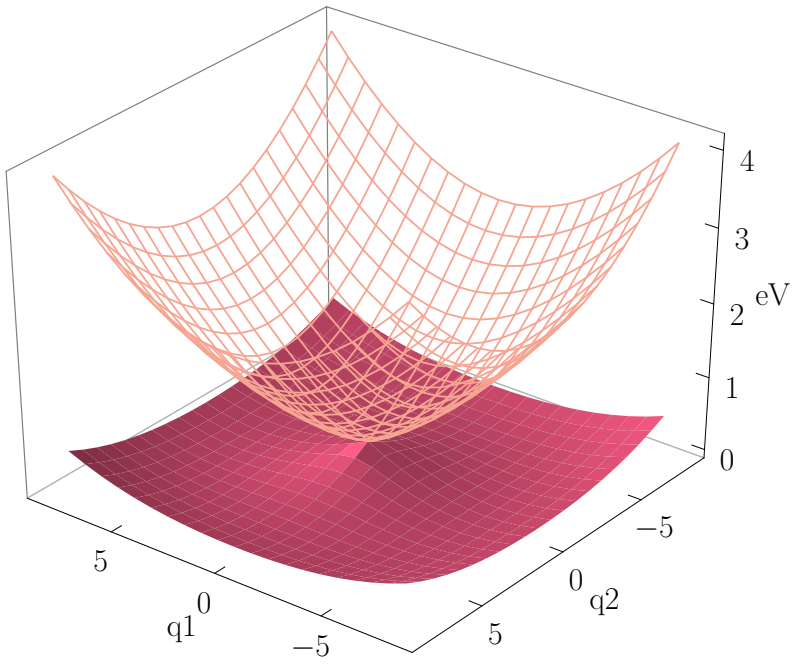


Figure 3.47: Static 3D image of Jahn-Teller system

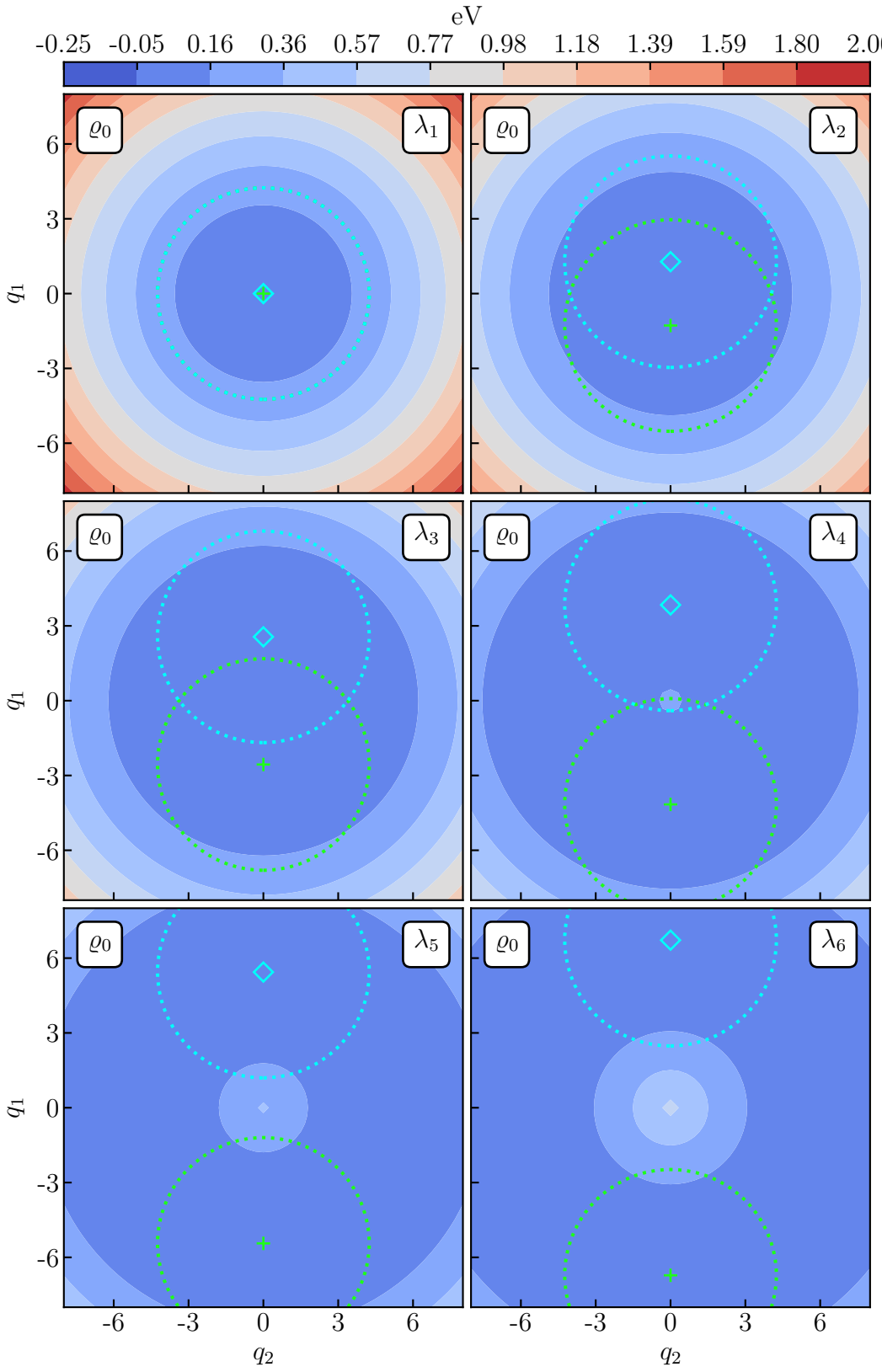


Figure 3.48: Elevation maps of lower surface for Jahn-Teller system

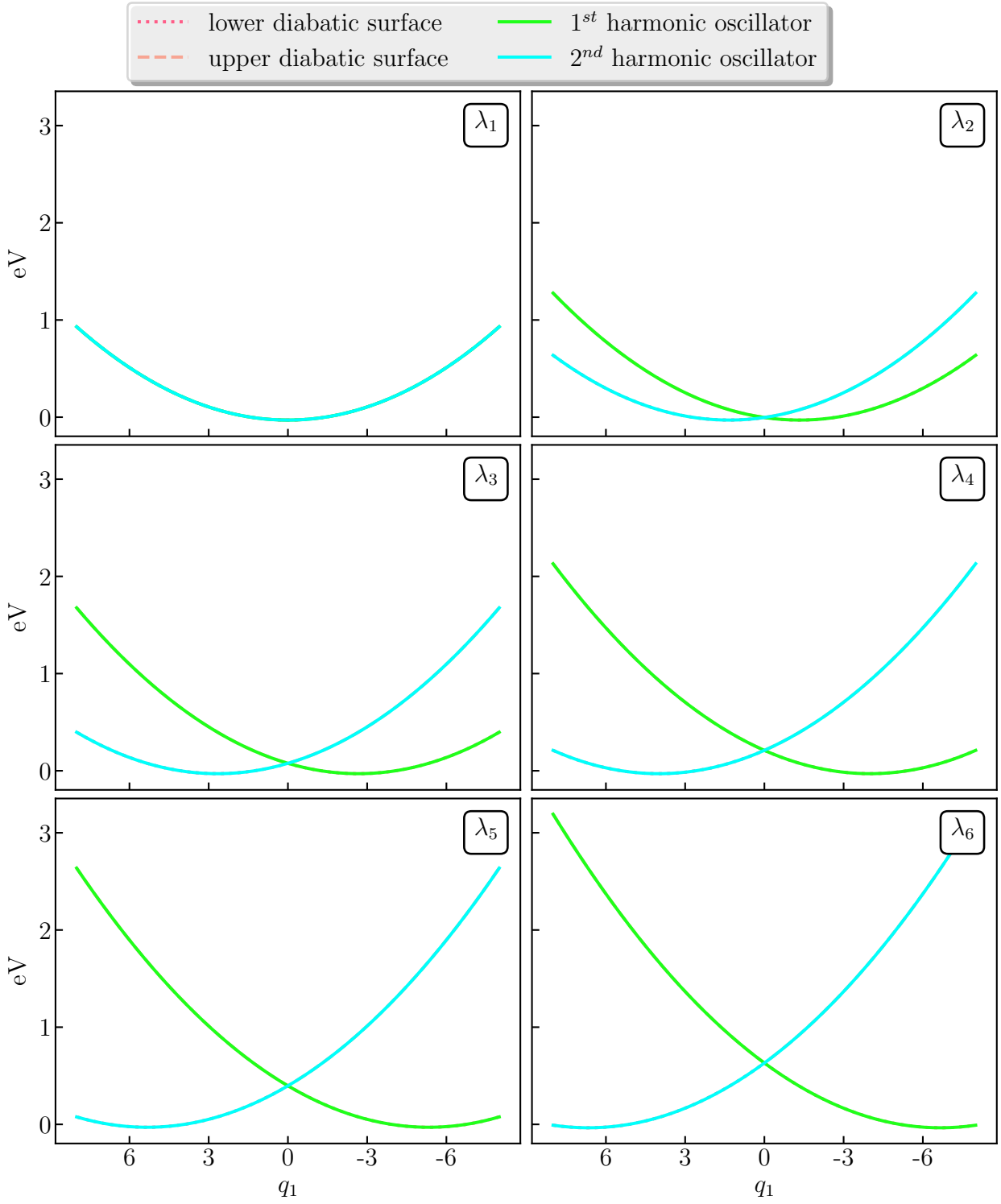


Figure 3.49: $q_1$ slices of Jahn-Teller system

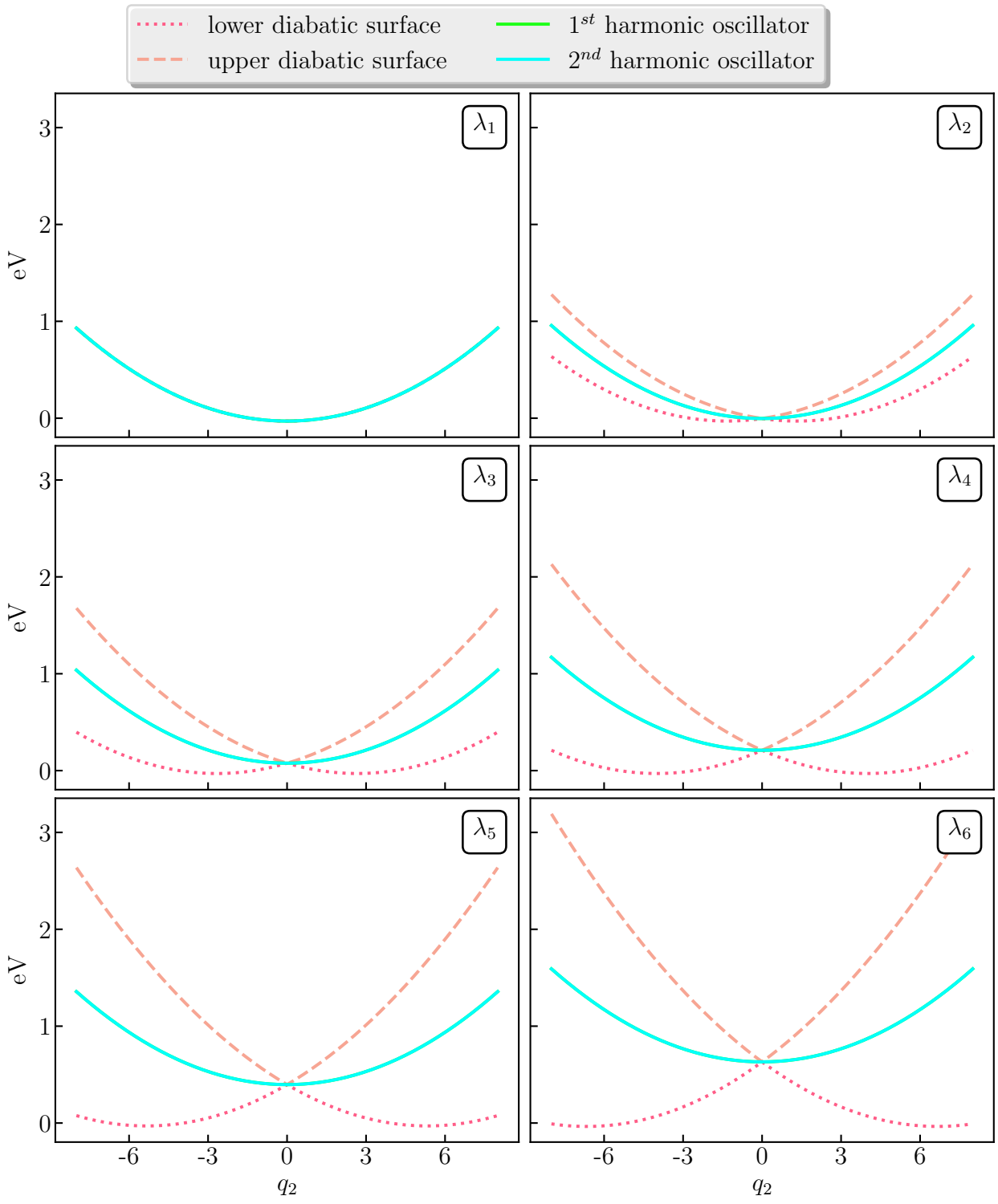


Figure 3.50: $q_2$ slices of Jahn-Teller system

### PIMC results

The Jahn-Teller system is purely harmonic for $\lambda_1$, therefore the analytical, SOS, and Trotter results should be equal in all $\tau$ regimes. This is what we observe in Figure 3.51. Again, there is a non-zero difference due to floating point error. The PIMC method exactly reproduces these results for all bead values.

The Trotter and PIMC results are a better approximation than the analytical results for $\lambda_2$, and their relative accuracy improves as the coupling term increases. This is shown by the discrepancy between the SOS and analytical lines.

For $\lambda_3$, the PIMC results begin to get noisy, but the overall convergence is appropriate. For $\lambda_4$ there are sizable discrepancies between the Trotter and PIMC results, and it appears to converge below the SOS result. Looking at Figure 3.48, the H.O.s comprising $\varrho_0$ are a very good model of the system in the $\{\lambda_1, \lambda_3\}$ range. In the $\lambda_4$ case, however, we see that $\approx 35\%$ of the lower well ($-0.1\ \mathrm{eV}$) is not covered by the $6\sigma$ of our oscillators. This matches the results we see in Figure 3.52. For $\lambda_5$ the H.O. system is less reasonable, and only gets worse for $\lambda_6$. As we saw before, a better choice of our distribution $\varrho$ is necessary.

The trend of the PIMC results for the energy are very similar to our previous models. One interesting difference is the discrepancy between the PIMC results and the Trotter results. For the previous systems they followed the same trend over the tunable parameter range, but in Jahn-Teller system this is not the case, as seen in Figure 3.54. It appears that the PIMC results are shifted slightly above the Trotter results. In general, we see the same effects on the energy as we did with the partition function. From $\lambda_1$ to $\lambda_2$ the PIMC results match the Trotter results, but they begin to suffer for $\lambda_3$ and they are very poor for $\lambda_4$ to $\lambda_6$.

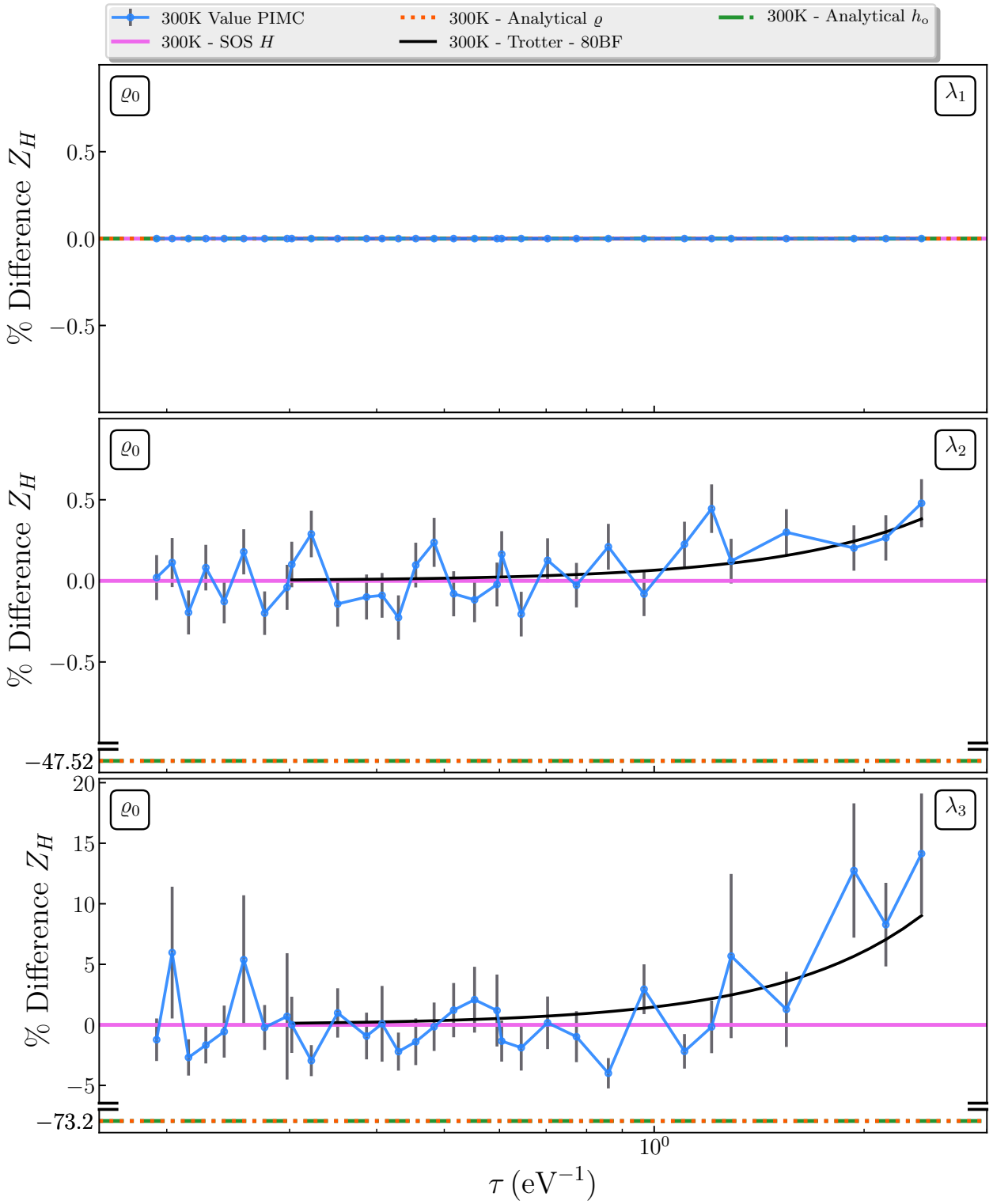


Figure 3.51: PIMC calculation of $Z$ for Jahn-Teller system over $\lambda_1 - \lambda_3$ range

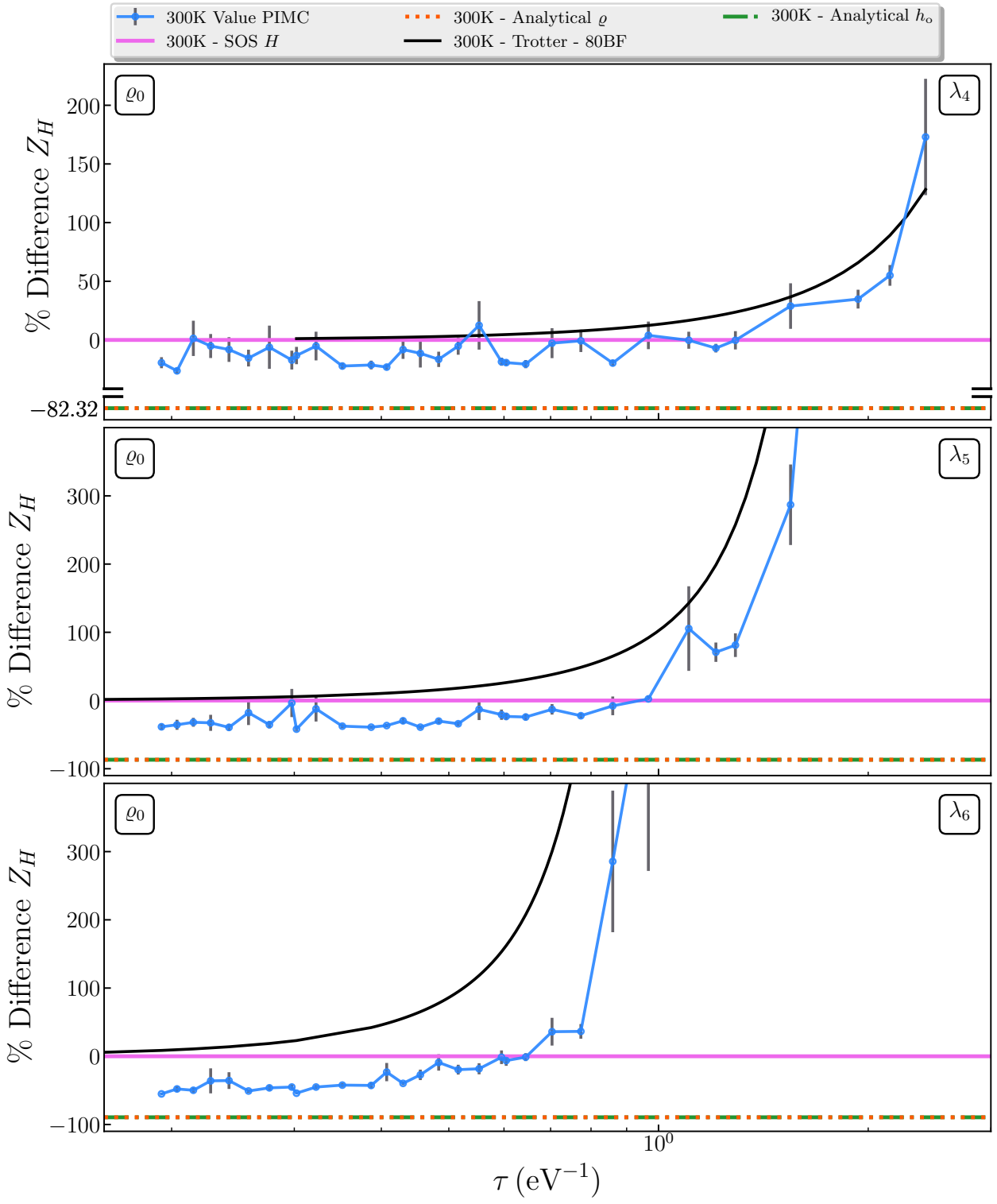


Figure 3.52: PIMC calculation of $Z$ for Jahn-Teller system over $\lambda_4 - \lambda_6$ range

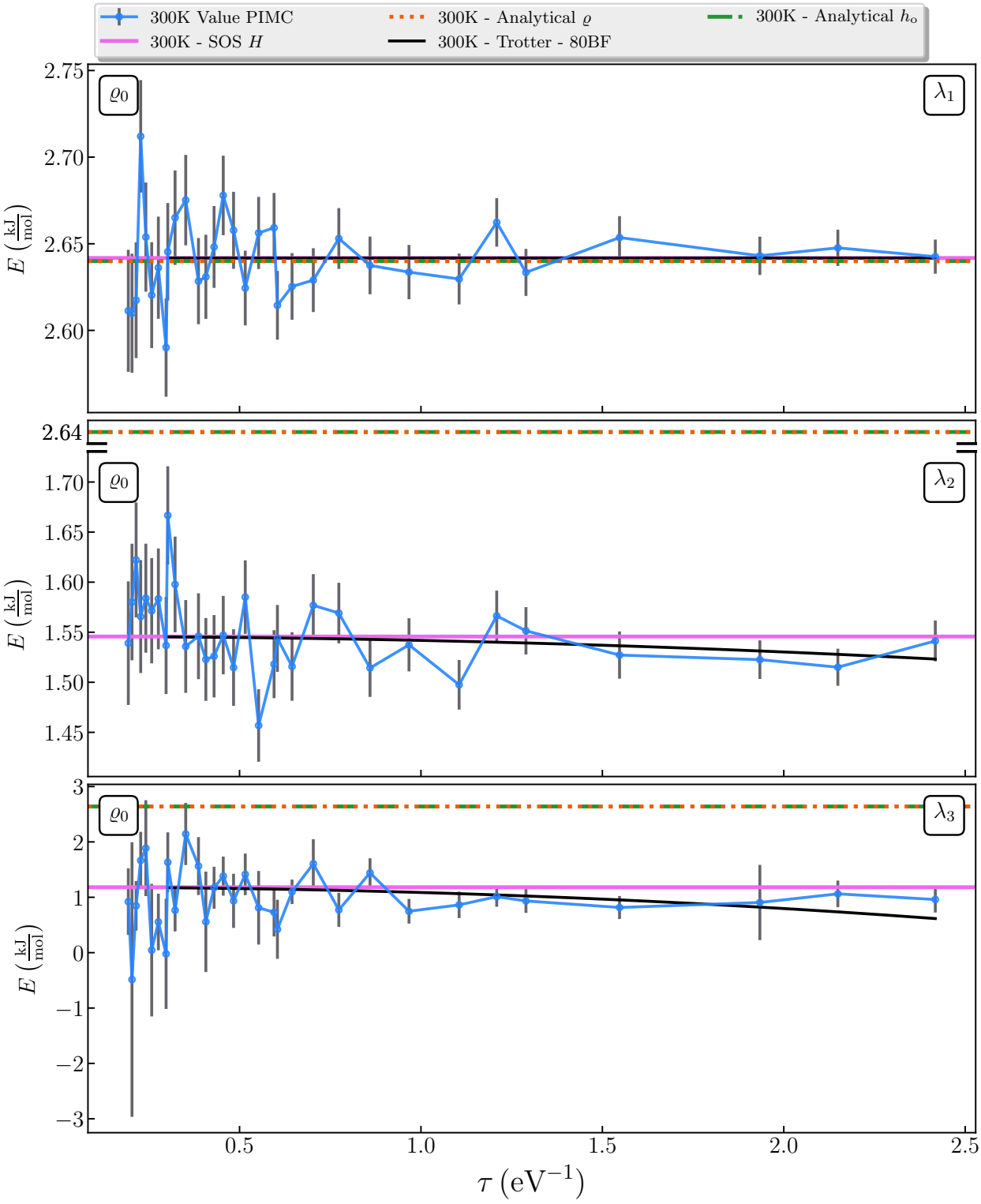


Figure 3.53: PIMC calculation of $E$ for Jahn-Teller system over $\lambda_1 - \lambda_3$ range

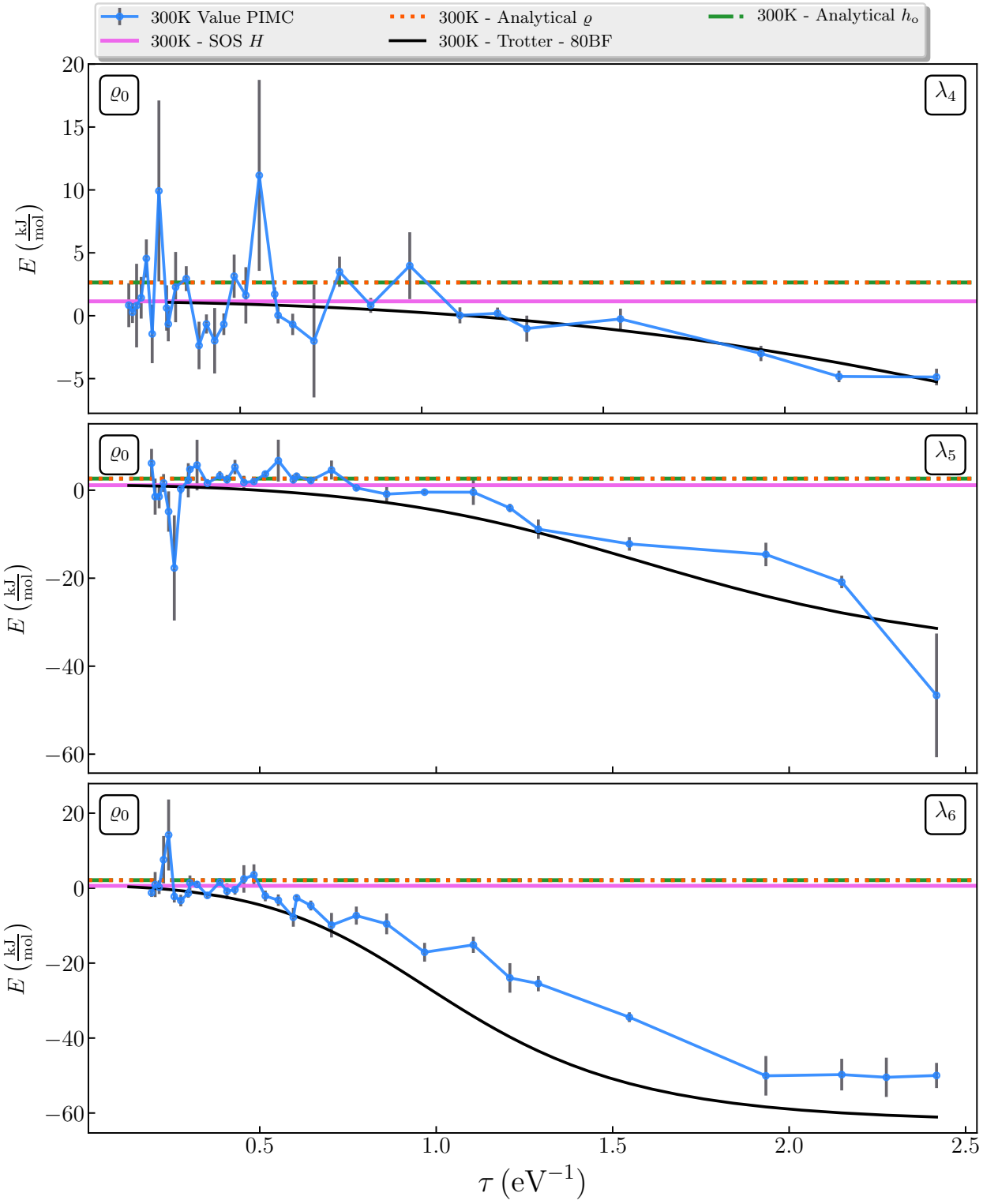


Figure 3.54: PIMC calculation of $E$ for Jahn-Teller system over $\lambda_4 - \lambda_6$ range

### Alternative sampling distributions

Our original choice of $\varrho$ is a poor description of the Jahn-Teller system for $\lambda_5$ and $\lambda_6$. The main problem with $\varrho_0$ is the lack of coverage of the lower surface. More than $50\%$ of the well for $\lambda_6$ can never be sampled. We therefore create two additional choices of $\varrho$ with increased coverage, using four surfaces, $\varrho_1$, and eight surfaces, $\varrho_2$. All energy, $\omega$, and $\lambda$ values are the same.

The matrix form for $\varrho_1$

$$\underline{\boldsymbol{E}} + \mathbf{ho} + \begin{bmatrix} +\lambda\hat{q}_1 & & & \\ & +\lambda\hat{q}_2 & & \\ & & -\lambda\hat{q}_1 & \\ & & & -\lambda\hat{q}_2 \end{bmatrix} \tag{3.16}$$

The matrix form for $\varrho_2$

$$\underline{\boldsymbol{E}} + \mathbf{ho} + \begin{bmatrix} \lambda\hat{q}_1 & & & & & & & \\ & \lambda\hat{q}_2 & & & & & & \\ & & -\lambda\hat{q}_1 & & & & & \\ & & & -\lambda\hat{q}_2 & & & & \\ & & & & \lambda\hat{\ell}_1 & & & \\ & & & & & \lambda\hat{\ell}_2 & & \\ & & & & & & -\lambda\hat{\ell}_1 & \\ & & & & & & & -\lambda\hat{\ell}_2 \end{bmatrix} \tag{3.17}$$

where

$$\hat{\ell}_1 = \frac{\hat{q}_1 + \hat{q}_2}{\sqrt{2}} \qquad \hat{\ell}_2 = \frac{\hat{q}_1 - \hat{q}_2}{\sqrt{2}} \tag{3.18}$$

Our new distributions for $\lambda_5$ and $\lambda_6$ are shown in Figure 3.55. We expect $\varrho_1$ to be an improvement over $\varrho_0$ due to the increased coverage of the lowest area of the well. Remember that the density of sampled points will decrease the farther we are from the minima of each oscillator. We therefore expect $\varrho_2$ to provide a significant improvement over $\varrho_1$. This is what we observe in Figure 3.59 and Figure 3.60. We see a significant decrease in the error of the energy in Figure 3.63. Again, we see a energy shift discrepency in out PIMC results.

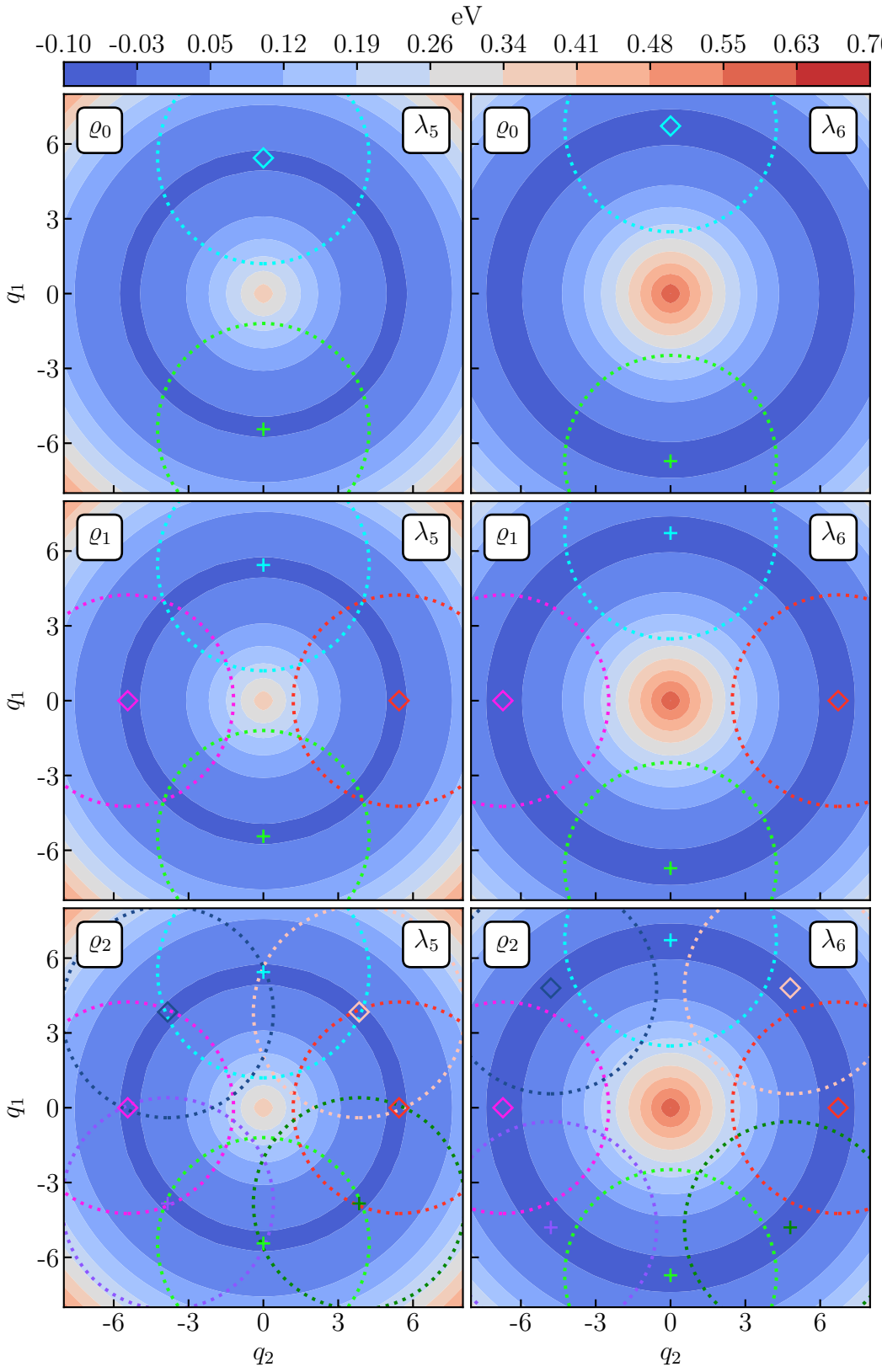


Figure 3.55: Elevation map of lower surface of Jahn-Teller system for three choices of $\varrho$

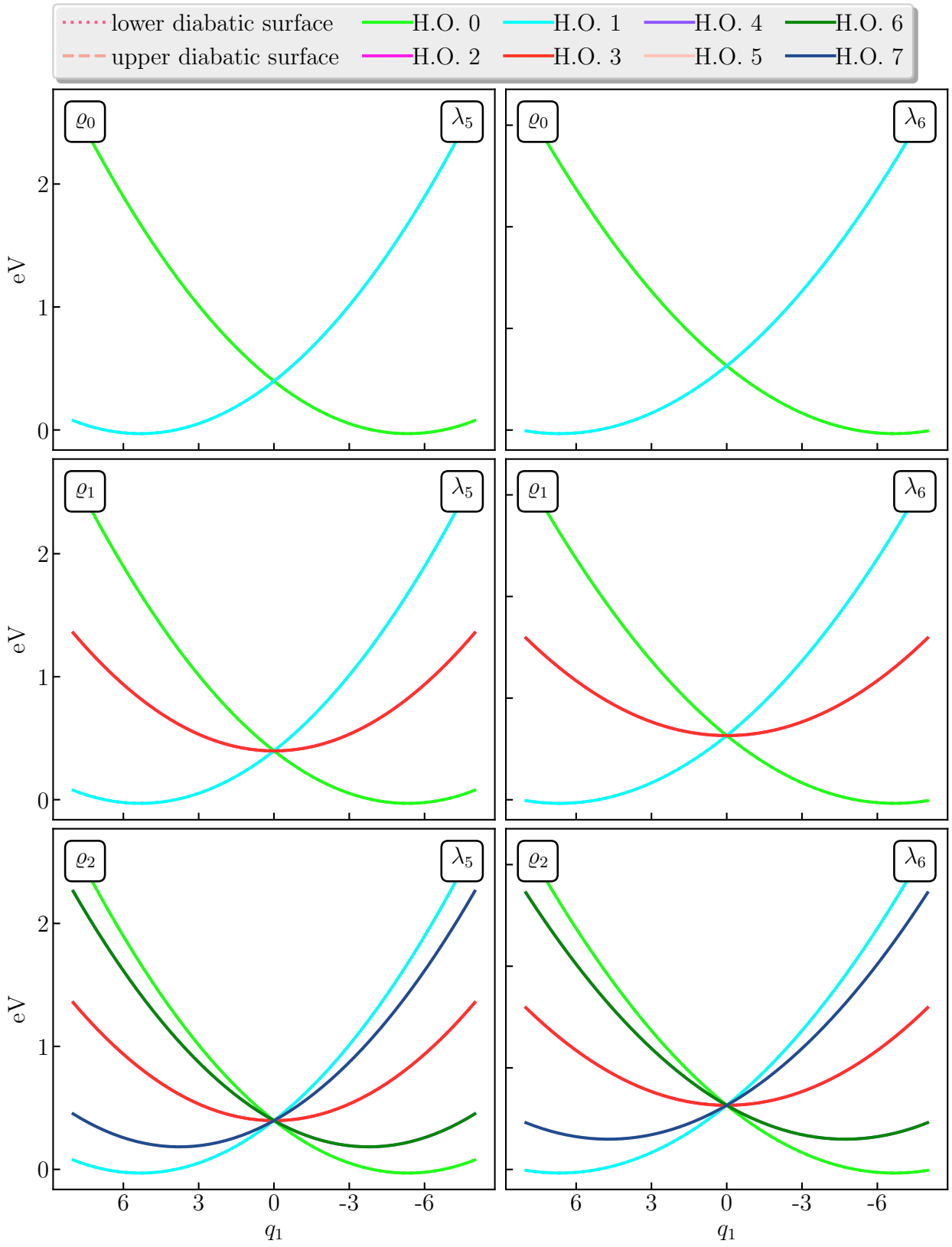


Figure 3.56: $q_1$ slices of Jahn-Teller system for three choices of $\varrho$

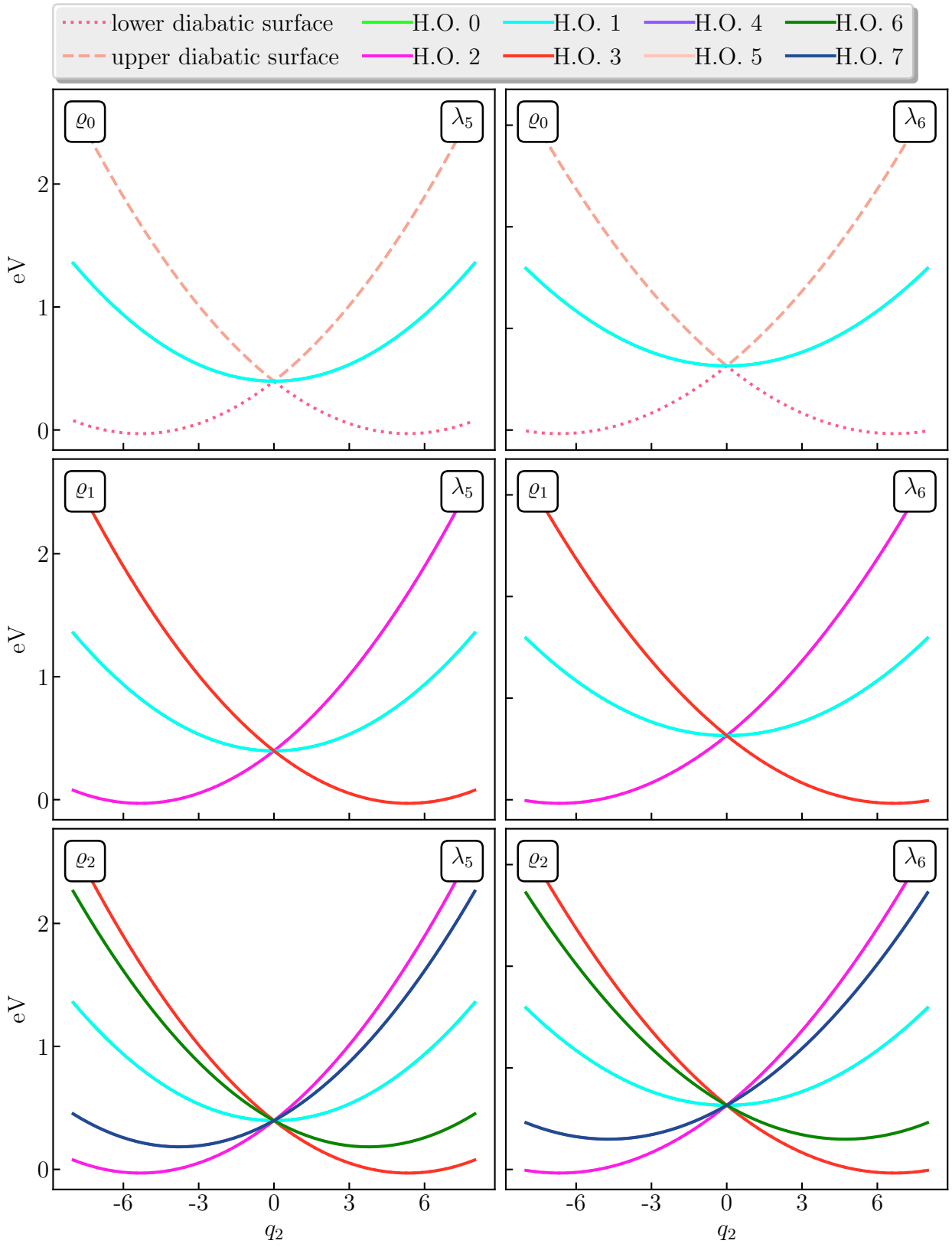


Figure 3.57: $q_2$ slices of Jahn-Teller system for three choices of $\varrho$

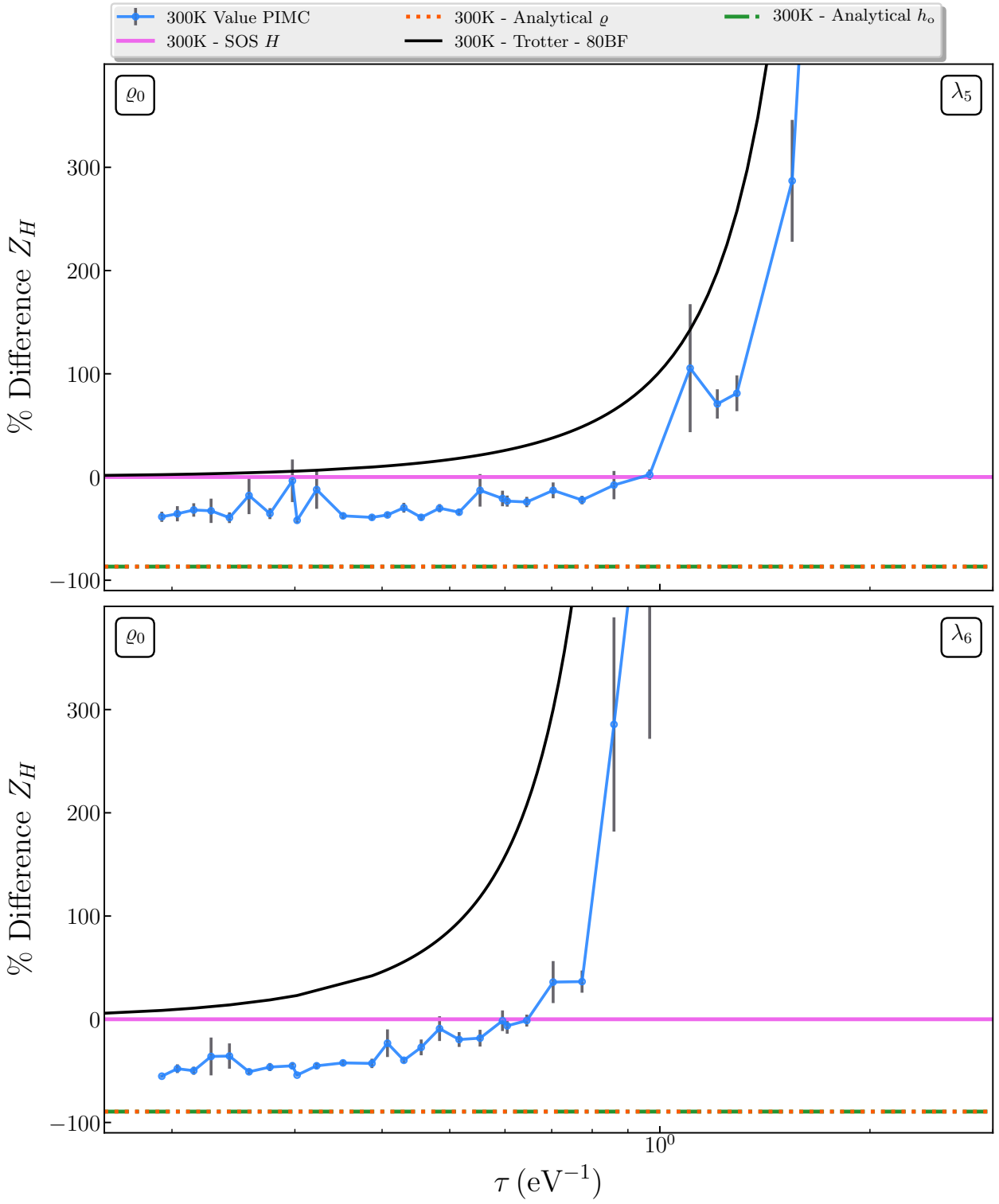


Figure 3.58: PIMC calculation of $Z$ with $\varrho_0$ for Jahn-Teller system over $\lambda_5 - \lambda_6$ range

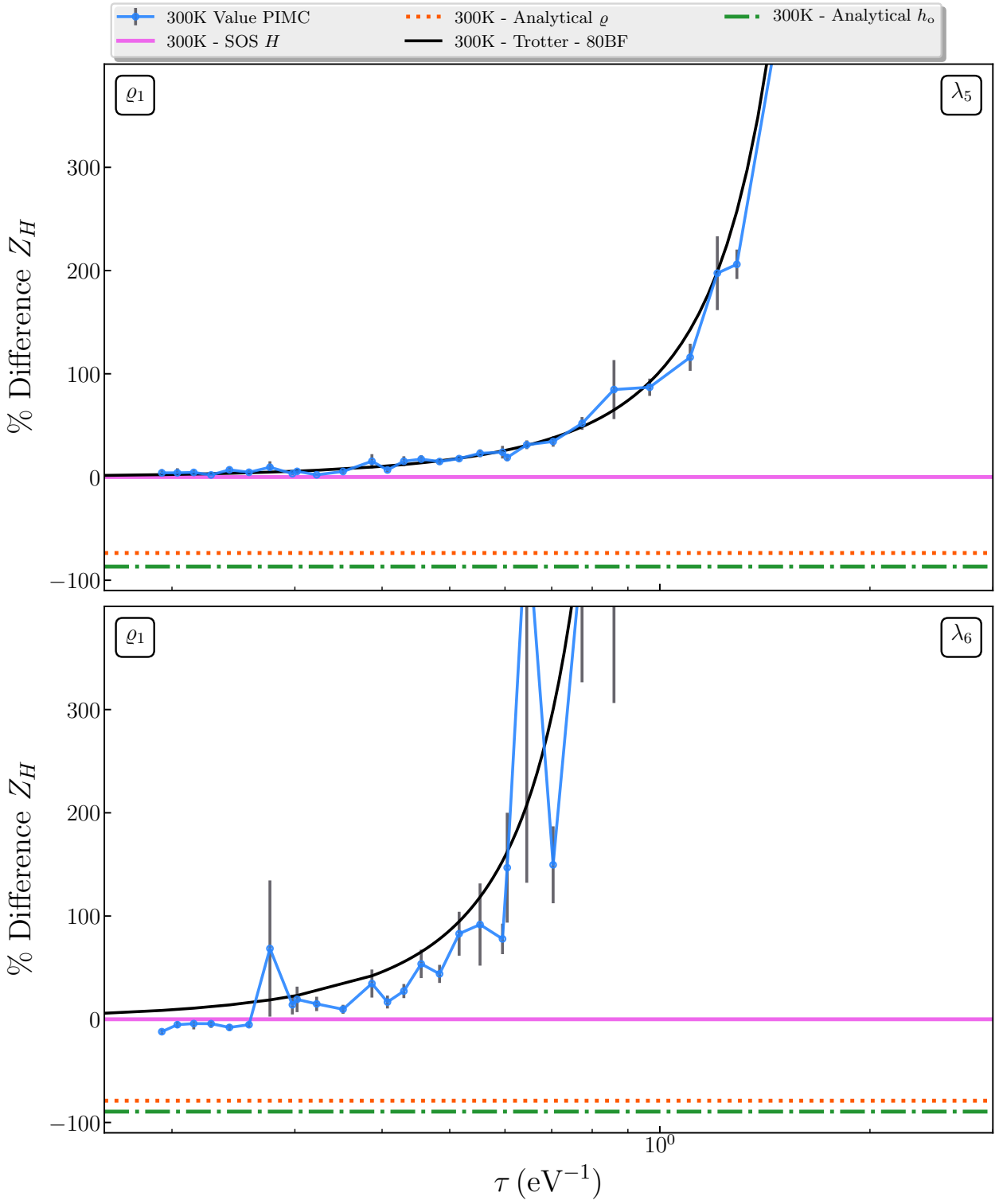


Figure 3.59: PIMC calculation of $Z$ with $\varrho_1$ for Jahn-Teller system over $\lambda_5 - \lambda_6$ range

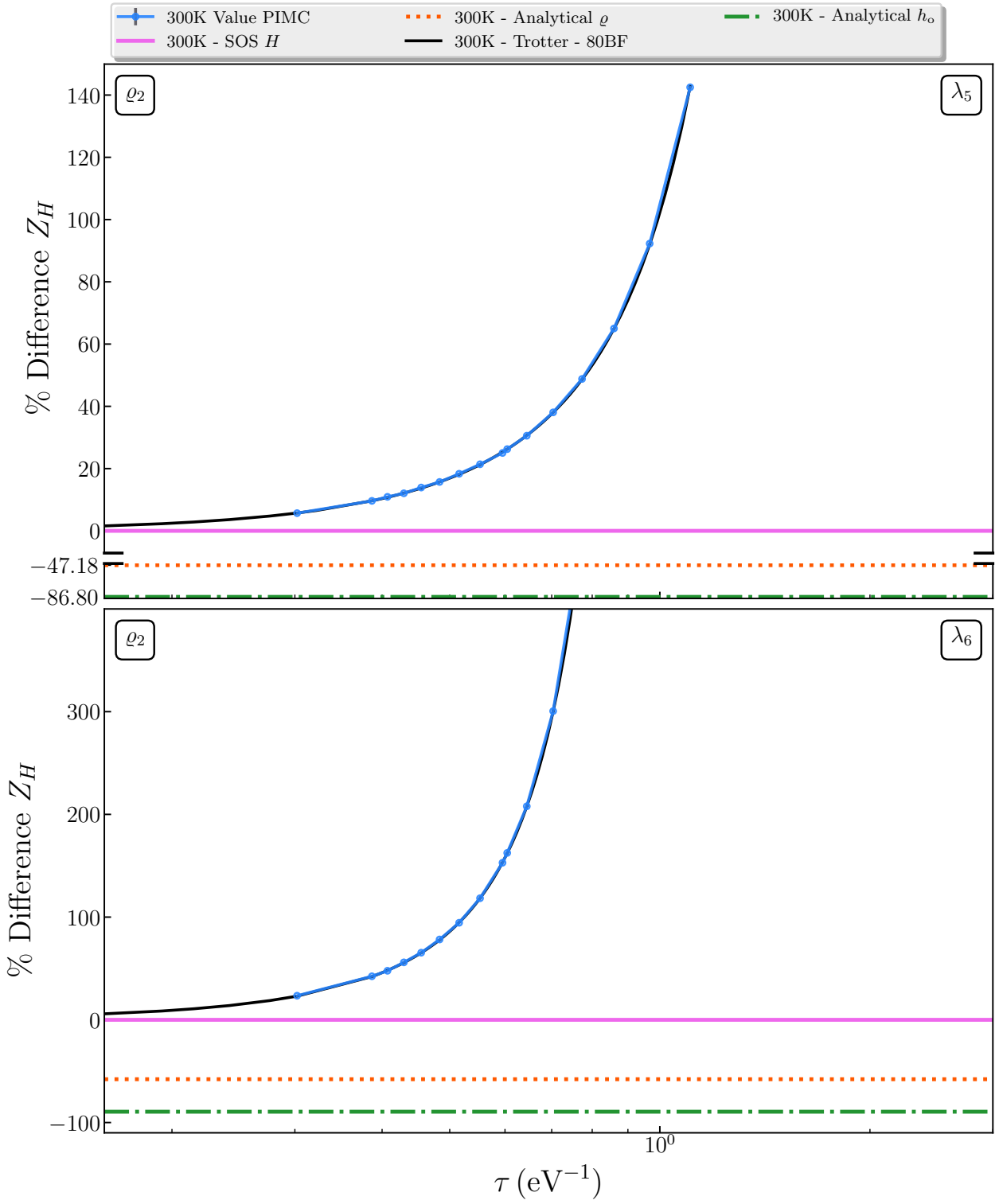


Figure 3.60: PIMC calculation of $Z$ with $\varrho_2$ for Jahn-Teller system over $\lambda_5 - \lambda_6$ range

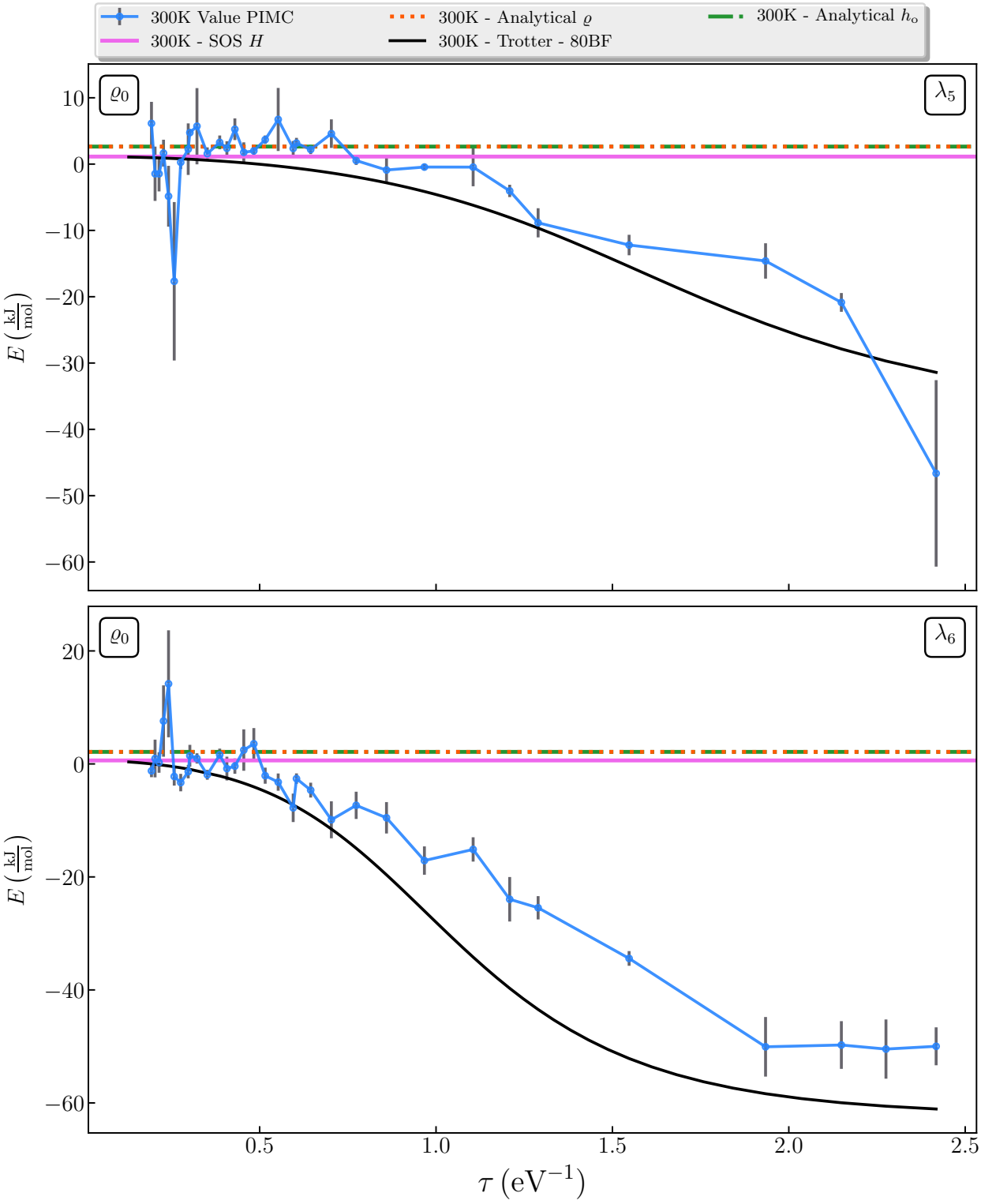


Figure 3.61: PIMC calculation of $E$ with $\varrho_0$ for Jahn-Teller system over $\lambda_5 - \lambda_6$ range

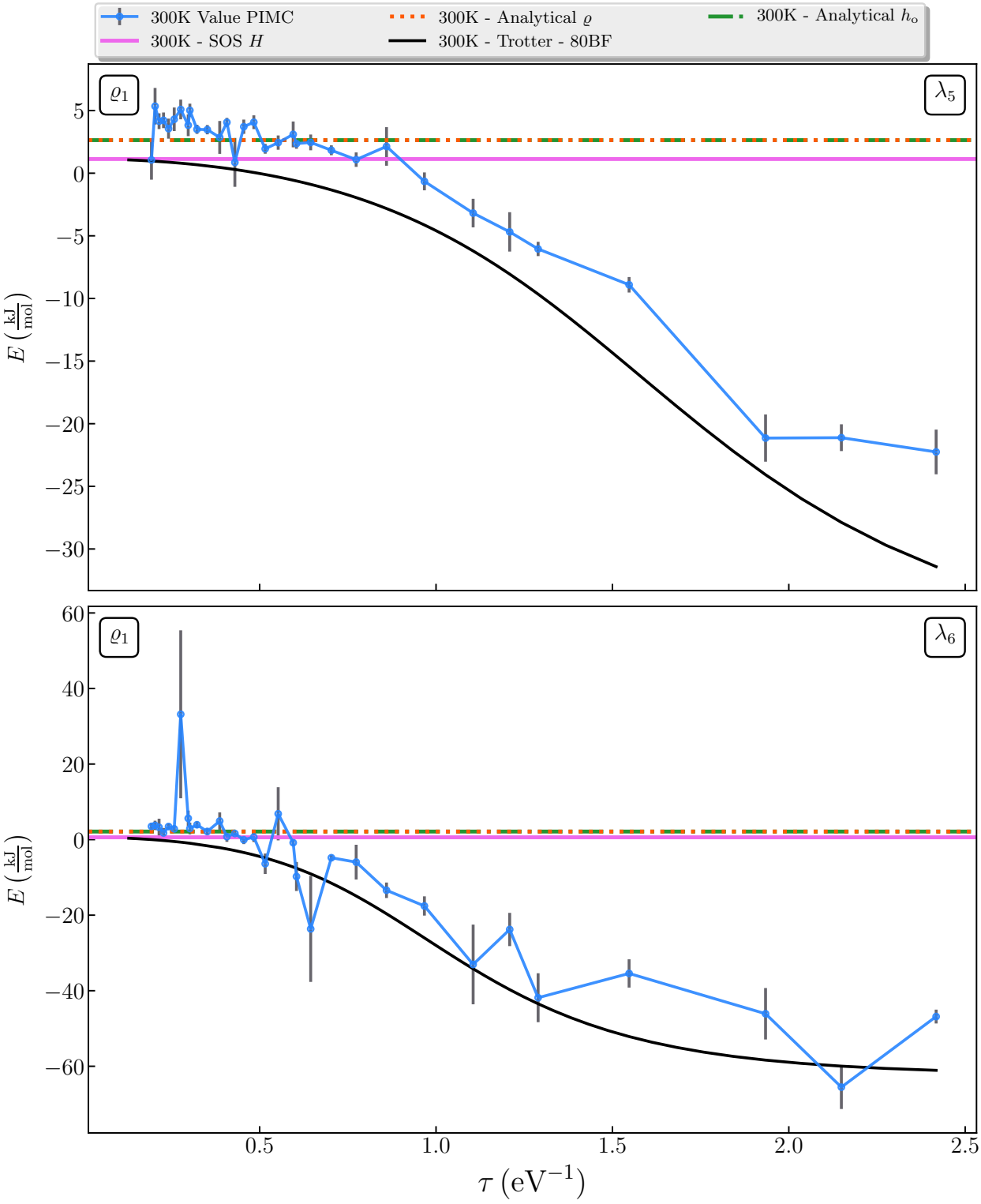


Figure 3.62: PIMC calculation of $E$ with $\varrho_1$ for Jahn-Teller system over $\lambda_5 - \lambda_6$ range

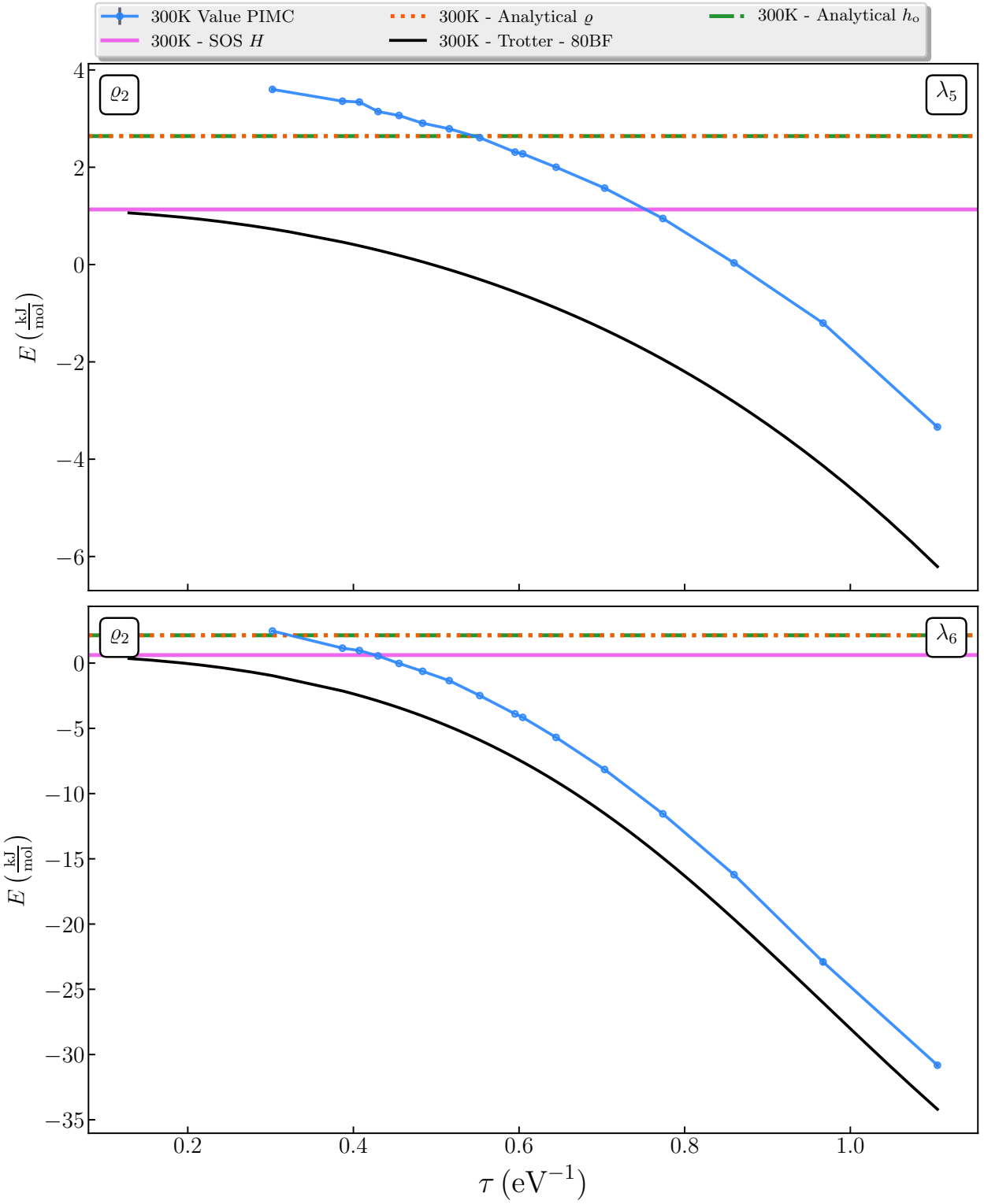


Figure 3.63: PIMC calculation of $E$ with $\varrho_2$ for Jahn-Teller system over $\lambda_5 - \lambda_6$ range

# Chapter 4

# Conclusions and Future work

The importance of choosing an appropriate $\varrho(\mathbf{R})$ was demonstrated repeatedly in Chapter 3. We showed that our PIMC method's deviation from finite basis Trotter calculations was systematic with respect to the choice of $\varrho(\mathbf{R})$. The accuracy of $\varrho(\mathbf{R})$ as a model of $g(\mathbf{R})$ has a greater effect on the accuracy of our method than the sample size. Increasing the accuracy of $\varrho(\mathbf{R})$ will allow for a reduction in number of samples drawn, making our method more computationally efficient. We saw extremely good results for the estimation of $Z$ with only simple improvements to our choice of $\varrho(\mathbf{R})$. Our results for the $U$ with improved $\varrho(\mathbf{R})$ showed a large reduction in the variance of our estimator. However, the presence of a unexpected energy shift raises some questions. Due to time constraints we were not able to determine the cause of these energy shifts. It is likely that this effect is an artefact resulting from our implementation of the PIMC method.

## Future Work

No work was done in this thesis on the construction of vibronic models. However, given that the average scientist does not know how to construct vibronic models, it would be useful if the software package we make available contains the tools for a scientist to construct a vibronic model using only their knowledge of their molecule. There are many technical aspects of our methodolgy which can be improved and provide valuable insight into the behaviour of our estimators. These aspects are primarily statistical or numerical in nature. Fortunately many of them are well-known problems in their respective fields; literature discussing approaches to these problems is plentiful.

Regarding plans for future work: first and foremost the energy shift will be investigated. This work will consist primarily of isolated unit tests to determine if the plot is representative of the data. If there is an issue with the data, it is likely that the error occurs in the calculation of $U_{\varrho}$. This can be determined by investigating a purely harmonic model system which includes quadratic terms where $\varrho(\mathbf{R})$ only contains linear terms.

A lot of research has been conducted on estimators, such as higher-order estimators and the virial estimator, to improve the variance of PI methods. It seems evident that we should utilize this work to improve our method. As previously mentioned in Section 3.1, deriving modified estimators that include our electronic DoF is of interest. A formulation for a virial-like estimator for the energy would hopefully reduce the erratic behaviour in the low $\tau$ regime.

In Chapter 3, we showed the convergence of our PIMC method using a dense range of $P$ values. In practice, the efficiency of such an approach should utilize fitting schemes and a sparse range of $P$ values to achieve similar results. A broad comparison of fitting schemes in high and low $\tau$ regimes would be useful.

Our current SOS implementation could be modified to calculate $\beta$ derivatives by finite difference. More insight into the behaviour of our method could be gained by separating the finite difference error from the sampling error. Analysis of the choice of $\Delta\beta$ as a function of temperature could be performed.

For larger and more complex systems where the PES is not fully known, single-point calculations of local minima and maxima could be used to determine the location of harmonic oscillators that comprise $\varrho(\mathbf{R})$.

The use of Graphics Processing Units (GPUs) in our implementation is highly desirable due to the highly parallel nature of our PIMC method. It is of interest to study the possible computational gains that can be realized through the use of GPUs.

# Bibliography


[1] D. A. McQuarrie and J. D. Simon, *Physical chemistry: a molecular approach*, 1 edition (University Science Books, Sausalito, Calif, July 1997) (cit. on p. 1).

[2] F. Jensen, *Introduction to computation chemistry* (Wiley, 1998) (cit. on p. 1).

[3] J. Baltrusaitis, T. Bučko, W. Michaels, M. Makkee, and G. Mul, "Catalytic methyl mercaptan coupling to ethylene in chabazite: DFT study of the first CC bond formation", Applied Catalysis B: Environmental **187**, 195–203 (2016) (cit. on p. 3).

[4] S. Thangavel, S. Boopathi, N. Mahadevaiah, P. Kolandaivel, P. B. Pansuriya, and H. B. Friedrich, "Catalytic oxidation of primary aromatic alcohols using half sandwich ir(III), rh(III) and ru(II) complexes: a practical and theoretical study", Journal of Molecular Catalysis A: Chemical **423**, 160–171 (2016) (cit. on p. 3).

[5] D. Geburtig, P. Preuster, A. Bösmann, K. Müller, and P. Wasserscheid, "Chemical utilization of hydrogen from fluctuating energy sources – catalytic transfer hydrogenation from charged liquid organic hydrogen carrier systems", International Journal of Hydrogen Energy **41**, 1010–1017 (2016) (cit. on p. 3).

[6] A. W. Hauser, P. R. Horn, M. Head-Gordon, and A. T. Bell, "A systematic study on pt based, subnanometer-sized alloy cluster catalysts for alkane dehydrogenation: effects of intermetallic interaction", Physical Chemistry Chemical Physics **18**, 10906–10917 (2016) (cit. on p. 3).

[7] L. Petitjean, R. Gagne, E. S. Beach, D. Xiao, and P. T. Anastas, "Highly selective hydrogenation and hydrogenolysis using a copper-doped porous metal oxide catalyst", Green Chemistry **18**, 150–156 (2016) (cit. on p. 3).

[8] G. Liang, X. Liu, X. Zhang, H. Xu, and B. Yan, "Accurate potential energy functions, nonadiabatic and spin–orbit couplings in the ZnH+ system", Spectrochimica Acta Part A: Molecular and Biomolecular Spectroscopy **156**, 9–14 (2016) (cit. on p. 4).

[9] J. C. Tully, "Perspective: nonadiabatic dynamics theory", The Journal of chemical physics **137**, 22A301 (2012) (cit. on p. 4).

[10] L. A. Peteanu, R. W. Schoenlein, Q. Wang, R. A. Mathies, and C. V. Shank, "The first step in vision occurs in femtoseconds: complete blue and red spectral studies", Proceedings of the National Academy of Sciences **90**, 11762–11766 (1993) (cit. on p. 5).

[11] J. I. Mendieta-Moreno, D. G. Trabada, J. Mendieta, J. P. Lewis, P. Gómez-Puertas, and J. Ortega, "Quantum mechanics/molecular mechanics free energy maps and nonadiabatic simulations for a photochemical reaction in DNA: cyclobutane thymine dimer", The Journal of Physical Chemistry Letters **7**, 4391–4397 (2016) (cit. on p. 5).

[12] A. Witt, S. D. Ivanov, and D. Marx, "Ab initio path integral simulations of floppy molecular systems", in *High performance computing in science and engineering, Garching/Munich* (Springer, Berlin, Heidelberg, 2010), pp. 675–686 (cit. on p. 6).

[13] X. Song, C. Lin, Z. Sheng, P. Liu, Z. Chen, W. Yang, S. Hu, C. D. Lin, and J. Chen, "Unraveling nonadiabatic ionization and coulomb potential effects in strong-field photoelectron holography", arXiv:1602.06019 [physics] (2016) (cit. on p. 6).

[14] J. Ryan Duke and N. Ananth, "Mean field ring polymer molecular dynamics for electronically nonadiabatic reaction rates", Faraday Discussions **195**, 253–268 (2016) (cit. on p. 6).

[15] M. K. Lee, P. Huo, and D. F. Coker, "Semiclassical path integral dynamics: photosynthetic energy transfer with realistic environment interactions", Annual Review of Physical Chemistry **67**, 639–668 (2016) (cit. on p. 6).

[16] J. S. Kretchmer and T. F. M. Iii, "Kinetically-constrained ring-polymer molecular dynamics for non-adiabatic chemistries involving solvent and donor–acceptor dynamical effects", Faraday Discuss. **195**, 191–214 (2017) (cit. on p. 6).

[17] W. H. Press, *Numerical recipes 3rd edition: the art of scientific computing* (Cambridge University Press, 2007) (cit. on p. 6).

[18] J. M. Restrepo, "A path integral method for data assimilation", Physica D: Nonlinear Phenomena **237**, 14–27 (2008) (cit. on p. 6).

[19] L. Martino and J. Miguez, "A generalization of the adaptive rejection sampling algorithm", Statistics and Computing **21**, 633–647 (2011) (cit. on p. 6).

[20] T. Van Voorhis, T. Kowalczyk, B. Kaduk, L.-P. Wang, C.-L. Cheng, and Q. Wu, "The diabatic picture of electron transfer, reaction barriers, and molecular dynamics", Annual review of physical chemistry **61**, 149–170 (2010) (cit. on p. 7).

[21] L. S. Schulman, *Techniques and applications of path integration* (Courier Corporation, Oct. 10, 2012), 434 pp. (cit. on pp. 7, 9).

[22] S. Weinzierl, "Introduction to monte carlo methods", arXiv:hep-ph/0006269, 11–17 (2000) (cit. on p. 7).

[23] K. E. Schmidt and M. A. Lee, "High-accuracy trotter-formula method for path integrals", Physical Review E **51**, 5495–5498 (1995) (cit. on p. 10).

[24] M. Tuckerman, *Statistical mechanics: theory and molecular simulation* (Oxford University Press, 2010) (cit. on pp. 11, 12).

[25] Frühwirth-Schnatter, Sylvia, *Finite mixture and markov switching models*, Springer Series in Statistics (Springer New York, 2006) (cit. on p. 13).

[26] W. Pauli, *Pauli lectures on physics [edited by Charles P. Enz. translated by S. Margulies and H. R. Lewis. foreword by Victor F. Weisskopf.* Vol. 1 (Cambridge, Mass, MIT Press-, 2000) (cit. on p. 14).

[27] P. Young, "Everything you wanted to know about data analysis and fitting but were afraid to ask", arXiv:1210.3781 [cond-mat, physics:physics] (2012) (cit. on pp. 18, 106).

[28] T. M. Yamamoto, "Path-integral virial estimator based on the scaling of fluctuation coordinates: application to quantum clusters with fourth-order propagators", The Journal of Chemical Physics **123**, 104101 (2005) (cit. on p. 26).

# Appendix

## Appendix A: Path Integral Formulation

We start with

$$Z = \mathrm{Tr}\left[e^{-\beta\hat{H}}\right] \tag{A.1}$$

$$= \int \mathrm{d}\mathbf{R}_1 \sum_{a_1=1}^{A} \langle \mathbf{R}_1, a_1 | \, e^{-\beta\hat{H}} \, | \mathbf{R}_1, a_1 \rangle \tag{A.2}$$

Add two resolutions of the identity

$$Z = \int \mathrm{d}\mathbf{R}_1 \sum_{a_1=1}^{A} \Bigg[ \langle \mathbf{R}_1, a_1 | \, e^{-\beta\hat{H}/3} \Bigg( \int \mathrm{d}\mathbf{R}_2 \sum_{a_2=1}^{A} |\mathbf{R}_2, a_2\rangle \langle \mathbf{R}_2, a_2| \Bigg) \times \Bigg( e^{-\beta\hat{H}/3} \Bigg) \Bigg( \int \mathrm{d}\mathbf{R}_3 \sum_{a_3=1}^{A} |\mathbf{R}_3, a_3\rangle \langle \mathbf{R}_3, a_3| \Bigg) e^{-\beta\hat{H}/3} \, |\mathbf{R}_1, a_1\rangle \Bigg] \tag{A.3}$$

Combine the integrals

$$Z = \int \mathrm{d}\mathbf{R}_1 \int \mathrm{d}\mathbf{R}_2 \int \mathrm{d}\mathbf{R}_3 \sum_{a_1=1}^{A} \Bigg[ \langle \mathbf{R}_1, a_1 | \, e^{-\beta\hat{H}/3} \Bigg( \sum_{a_2=1}^{A} |\mathbf{R}_2, a_2\rangle \langle \mathbf{R}_2, a_2| \Bigg) \times \Bigg( e^{-\beta\hat{H}/3} \Bigg) \Bigg( \sum_{a_3=1}^{A} |\mathbf{R}_3, a_3\rangle \langle \mathbf{R}_3, a_3| \Bigg) e^{-\beta\hat{H}/3} \, |\mathbf{R}_1, a_1\rangle \Bigg] \tag{A.4}$$

Combine the sums

$$Z = \int \mathrm{d}\mathbf{R}_1 \int \mathrm{d}\mathbf{R}_2 \int \mathrm{d}\mathbf{R}_3 \sum_{a_1}^{A} \sum_{a_2}^{A} \sum_{a_3}^{A} \Bigg[ \langle \mathbf{R}_1, a_1 | \, e^{-\beta\hat{H}/3} \Bigg( |\mathbf{R}_2, a_2\rangle \langle \mathbf{R}_2, a_2| \Bigg) \times \Bigg( e^{-\beta\hat{H}/3} \Bigg) \Bigg( |\mathbf{R}_3, a_3\rangle \langle \mathbf{R}_3, a_3| \Bigg) e^{-\beta\hat{H}/3} \, |\mathbf{R}_1, a_1\rangle \Bigg] \tag{A.5}$$

Condense the propagators

$$Z = \int \mathrm{d}\mathbf{R}_1 \int \mathrm{d}\mathbf{R}_2 \int \mathrm{d}\mathbf{R}_3 \sum_{a_1}^{A} \sum_{a_2}^{A} \sum_{a_3}^{A} \left[ \prod_{i=1}^{3} \langle \mathbf{R}_i, a_i | \, e^{-\beta \hat{H}/3} \, | \mathbf{R}_{i+1}, a_{i+1} \rangle \right] \tag{A.6}$$

Giving us the following general equation after inserting $P - 1$ resolutions of the identity where $P$ is the number of imaginary time-slices, also known as "beads", and $\tau = \beta/P$

$$Z = \int \mathrm{d}\mathbf{R}_1 \cdots \int \mathrm{d}\mathbf{R}_P \sum_{a_1}^{A} \cdots \sum_{a_P}^{A} \left[ \prod_{i=1}^{P} \langle \mathbf{R}_i, a_i | \, e^{-\tau \hat{H}} \, | \mathbf{R}_{i+1}, a_{i+1} \rangle \right] \tag{A.7}$$

In a more compact form

$$Z = \int \mathrm{d}\mathbf{R}^P \sum_{\mathbf{a}}^{A} \prod_{i=1}^{P} \langle \mathbf{R}_i, a_i | \, e^{-\tau \hat{H}} \, | \mathbf{R}_{i+1}, a_{i+1} \rangle \tag{A.8}$$

where we make use of the compact notation

$$\sum_{\mathbf{a}}^{A} = \sum_{a_1=1}^{A} \sum_{a_2=1}^{A} \cdots \sum_{a_P=1}^{A} \tag{A.9}$$

and

$$\int \mathrm{d}\mathbf{R}^P = \int \mathrm{d}\mathbf{R}_1 \int \mathrm{d}\mathbf{R}_2 \cdots \int \mathrm{d}\mathbf{R}_P \tag{A.10}$$

## Appendix B: Trotter Factorization

Now consider the following illustrative example:

$$\langle \mathbf{R}_1, a_1 | \, e^{-\frac{\tau}{2}\hat{h}_o} e^{-\tau \hat{V}} e^{-\frac{\tau}{2}\hat{h}_o} \, | \mathbf{R}_2, a_2 \rangle \tag{B.1}$$

Insert two resolutions of the identity

$$\begin{aligned} \langle \mathbf{R}_1, a_1 | \, e^{-\frac{\tau}{2}\hat{h}_o} & \left( \int \mathrm{d}\mathbf{R}_k \sum_{a_k=1}^{A} | \mathbf{R}_k, a_k \rangle \langle \mathbf{R}_k, a_k | \right) \\ & \times \left( e^{-\tau \hat{V}} \right) \left( \int \mathrm{d}\mathbf{R}_\ell \sum_{a_\ell=1}^{A} | \mathbf{R}_\ell, a_\ell \rangle \langle \mathbf{R}_\ell, a_\ell | \right) e^{-\frac{\tau}{2}\hat{h}_o} \, | \mathbf{R}_2, a_2 \rangle \end{aligned} \tag{B.2}$$

Pull out the integrals

$$\begin{aligned} \int \int \mathrm{d}\mathbf{R}_k \mathrm{d}\mathbf{R}_\ell \, \langle \mathbf{R}_1, a_1 | \, e^{-\frac{\tau}{2}\hat{h}_o} & \left( \sum_{a_k=1}^{A} | \mathbf{R}_k, a_k \rangle \langle \mathbf{R}_k, a_k | \right) \\ & \times \left( e^{-\tau \hat{V}} \right) \left( \sum_{a_\ell=1}^{A} | \mathbf{R}_\ell, a_\ell \rangle \langle \mathbf{R}_\ell, a_\ell | \right) e^{-\frac{\tau}{2}\hat{h}_o} \, | \mathbf{R}_2, a_2 \rangle \end{aligned} \tag{B.3}$$

Pull out the sums

$$\begin{aligned} \int \int \mathrm{d}\mathbf{R}_k \mathrm{d}\mathbf{R}_\ell \sum_{a_k=1}^{A} \sum_{a_\ell=1}^{A} & \langle \mathbf{R}_1, a_1 | \, e^{-\frac{\tau}{2}\hat{h}_o} \, | \mathbf{R}_k, a_k \rangle \langle \mathbf{R}_k, a_k | \, \delta_{a_1, a_k} \\ & \times \left( e^{-\tau \hat{V}} \right) | \mathbf{R}_\ell, a_\ell \rangle \langle \mathbf{R}_\ell, a_\ell | \, e^{-\frac{\tau}{2}\hat{h}_o} \, | \mathbf{R}_2, a_2 \rangle \, \delta_{a_\ell, a_2} \end{aligned} \tag{B.4}$$

By definition of $\hat{h}_o$: (diagonal in electronic surfaces $a$)

$$\begin{aligned} \int \int \mathrm{d}\mathbf{R}_k \mathrm{d}\mathbf{R}_\ell \sum_{a_k=1}^{A} \sum_{a_\ell=1}^{A} & \langle \mathbf{R}_1, a_1 | e^{-\frac{\tau}{2}\hat{h}_o} \, | \mathbf{R}_k, a_1 \rangle \langle \mathbf{R}_k, a_1 | \\ & \times \left( e^{-\tau \hat{V}} \right) | \mathbf{R}_\ell, a_2 \rangle \langle \mathbf{R}_\ell, a_2 | \, e^{-\frac{\tau}{2}\hat{h}_o} \, | \mathbf{R}_2, a_2 \rangle \end{aligned} \tag{B.5}$$

More compactly

$$\int \int \mathrm{d}\mathbf{R}_k \mathrm{d}\mathbf{R}_\ell \, \langle \mathbf{R}_1, a_1 | \, e^{-\frac{\tau}{2}\hat{h}_o} \, | \mathbf{R}_k, a_1 \rangle \langle \mathbf{R}_k, a_1 | \, e^{-\tau \hat{V}} | \mathbf{R}_\ell, a_2 \rangle \langle \mathbf{R}_\ell, a_2 | \, e^{-\frac{\tau}{2}\hat{h}_o} \, | \mathbf{R}_2, a_2 \rangle \tag{B.6}$$

By the definition of $\hat{V}$, (V is diagonal in $\mathbf{R}$)

$$\int\int \mathrm{d}\mathbf{R}_k \mathrm{d}\mathbf{R}_\ell \left\langle \mathbf{R}_1, a_1 \right| e^{-\frac{\tau}{2}\hat{h}_o} \left| \mathbf{R}_k, a_1 \right\rangle \left\langle \mathbf{R}_k, a_1 \right| e^{-\tau \hat{V}} \left| \mathbf{R}_\ell, a_2 \right\rangle \delta(\mathbf{R}_k - \mathbf{R}_\ell) \left\langle \mathbf{R}_\ell, a_2 \right| e^{-\frac{\tau}{2}\hat{h}_o} \left| \mathbf{R}_2, a_2 \right\rangle \quad \text{(B.7)}$$

$$= \int \mathrm{d}\mathbf{R}_k \left\langle \mathbf{R}_1, a_1 \right| e^{-\frac{\tau}{2}\hat{h}_o} \left| \mathbf{R}_k, a_1 \right\rangle \left\langle \mathbf{R}_k, a_1 \right| e^{-\tau \hat{V}} \left| \mathbf{R}_k, a_2 \right\rangle \left\langle \mathbf{R}_k, a_2 \right| e^{-\frac{\tau}{2}\hat{h}_o} \left| \mathbf{R}_2, a_2 \right\rangle \quad \text{(B.8)}$$

And we can relabel $\mathbf{R}_k \to \mathbf{R}_1^{'}$

$$= \int \mathrm{d}\mathbf{R}_1^{'} \left\langle \mathbf{R}_1, a_1 \right| e^{-\frac{\tau}{2}\hat{h}_o} \left| \mathbf{R}_1^{'}, a_1 \right\rangle \left\langle \mathbf{R}_1^{'}, a_1 \right| e^{-\tau \hat{V}} \left| \mathbf{R}_1^{'}, a_2 \right\rangle \left\langle \mathbf{R}_1^{'}, a_2 \right| e^{-\frac{\tau}{2}\hat{h}_o} \left| \mathbf{R}_2, a_2 \right\rangle \quad \text{(B.9)}$$

Giving us the following general formula

$$Z \approx \lim_{P\to\infty} \int \mathrm{d}\mathbf{R}^P \sum_{\mathbf{a}}^{A} \prod_{i=1}^{P} \left\langle \mathbf{R}_i, a_i \right| e^{-\frac{\tau}{2}\hat{h}_o} \left| \mathbf{R}_i^{'}, a_i \right\rangle \left\langle \mathbf{R}_i^{'}, a_i \right| e^{-\tau \hat{V}} \left| \mathbf{R}_i^{'}, a_{i+1} \right\rangle \left\langle \mathbf{R}_i^{'}, a_{i+1} \right| e^{-\frac{\tau}{2}\hat{h}_o} \left| \mathbf{R}_{i+1}, a_{i+1} \right\rangle$$

(B.10)

$$\equiv \lim_{P\to\infty} \int \mathrm{d}\mathbf{R}^P \sum_{\mathbf{a}}^{A} \prod_{i=1}^{P} \left\langle \mathbf{R}_i, a_i \right| e^{-\tau \hat{h}_o} \left| \mathbf{R}_{i+1}, a_i \right\rangle \left\langle \mathbf{R}_{i+1}, a_i \right| e^{-\tau \hat{V}} \left| \mathbf{R}_{i+1}, a_{i+1} \right\rangle \quad \text{(B.11)}$$

## Appendix C: Nondimensionalization of the H.O.

The Schrodinger Equation for a one-dimensional time-independent H.O. is

$$\hat{H}\psi(x) = E\psi(x) \tag{C.1}$$

$$\left(-\frac{\hbar^2}{2m}\frac{\mathrm{d}^2}{\mathrm{d}x^2} + \frac{1}{2}m\omega^2 x^2\right)\psi(x) = E\psi(x) \tag{C.2}$$

We can reformulate equation eq. (C.2) in dimensionless coordinates $\tilde{x}$:

$$\text{let} \quad \tilde{x} \equiv \frac{x}{x_c} \quad \text{then} \quad \psi(x) = \psi(\tilde{x}x_c) = \psi(x(x_c)) = \tilde{\psi}\left(\tilde{x}\right)$$

$$\left(-\frac{\hbar^2}{2m}\frac{1}{x_c^2}\frac{\mathrm{d}^2}{\mathrm{d}\tilde{x}^2} + \frac{1}{2}m\omega^2 x_c^2\tilde{x}^2\right)\tilde{\psi}\left(\tilde{x}\right) = E\tilde{\psi}\left(\tilde{x}\right) \tag{C.3}$$

$$\left(-\frac{\mathrm{d}^2}{\mathrm{d}\tilde{x}^2} + \frac{m^2\omega^2 x_c^4}{\hbar^2}\tilde{x}^2\right)\tilde{\psi}\left(\tilde{x}\right) = \frac{2mx_c^2 E}{\hbar^2}\tilde{\psi}\left(\tilde{x}\right) \tag{C.4}$$

Define

$$\frac{m^2\omega^2 x_c^4}{\hbar^2} = 1 \implies x_c = \sqrt{\frac{\hbar}{m\omega}} \tag{C.5}$$

eq. (C.4) becomes

$$\left(-\frac{\mathrm{d}^2}{\mathrm{d}\tilde{x}^2} + \tilde{x}^2\right)\tilde{\psi}\left(\tilde{x}\right) = \tilde{E}\tilde{\psi}\left(\tilde{x}\right) \qquad \text{where} \quad E \equiv \frac{\hbar\omega}{2}\tilde{E} \tag{C.6}$$

Our final equation for the H.O. with energy in units of $\hbar\omega$ and distance in units of $\sqrt{\hbar/m\omega}$

$$\frac{\hbar\omega}{2}\left(-\frac{\mathrm{d}^2}{\mathrm{d}\tilde{x}^2} + \tilde{x}^2\right)\tilde{\psi}\left(\tilde{x}\right) = E\tilde{\psi}\left(\tilde{x}\right) \tag{C.7}$$

The following form is more commonly used when discussing normal mode coordinates

$$\frac{\hbar\omega}{2}\left(\hat{p}^2 + \hat{q}^2\right)\psi = E\psi \tag{C.8}$$

**Aside**

It is straightforward to show

$$\frac{\hbar\omega_0}{2}q^2 + \frac{\hbar\omega_1}{2}p^2 \tag{C.9}$$

can be re-expressed in the form of a dimensionless H.O.

$$\frac{\hbar\omega_3}{2}\left(\overline{p}^2+\overline{q}^2\right) \tag{C.10}$$

We define

$$\overline{q}^2 = q^2\left(\frac{\sqrt{\omega_1}}{\sqrt{\omega_0}}\right) \quad \Longrightarrow \quad \overline{p}^2 = -\frac{\mathrm{d}^2}{\mathrm{d}\overline{q}_2^2} = -\frac{\mathrm{d}^2}{\mathrm{d}q_2^2}\left(\frac{\sqrt{\omega_0}}{\sqrt{\omega_1}}\right) \tag{C.11}$$

Choose $\omega_3 = \sqrt{\omega_1\omega_0}$

$$\frac{\hbar\omega_0}{2}q^2 + \frac{\hbar\omega_1}{2}p^2 = \frac{\hbar\omega_3}{2}\left(\overline{q}^2+\overline{p}^2\right) \tag{C.12}$$

## Appendix D: Energy estimator

Evaluate the $\beta$ derivative using first order symmetric difference

$$\frac{\partial}{\partial\beta}Z_f \approx \left(\frac{1}{2\Delta\beta}\right)\left[Z_f\left(\beta+\Delta\beta\right)-Z_f\left(\beta-\Delta\beta\right)\right] \tag{D.1}$$

$$= \left(\frac{1}{2\Delta\beta}\right)\left[\frac{Z_H(\beta+\Delta\beta)}{Z_\varrho(\beta+\Delta\beta)}-\frac{Z_H(\beta-\Delta\beta)}{Z_\varrho(\beta-\Delta\beta)}\right] \tag{D.2}$$

Supposing we multiply eq. (D.2) by $\mathbb{1}=\dfrac{Z_\varrho}{Z_\varrho}$

$$= \left(\frac{1}{2\Delta\beta}\right)\left[\frac{Z_\varrho}{Z_\varrho(\beta+\Delta\beta)}\frac{Z_H(\beta+\Delta\beta)}{Z_\varrho(\beta)}-\frac{Z_\varrho(\beta)}{Z_\varrho(\beta-\Delta\beta)}\frac{Z_H(\beta-\Delta\beta)}{Z_\varrho(\beta)}\right] \tag{D.3}$$

For convenience we define

$$\alpha^+=\frac{Z_\varrho(\beta)}{Z_\varrho(\beta+\Delta\beta)} \qquad\qquad \alpha^-=\frac{Z_\varrho(\beta)}{Z_\varrho(\beta-\Delta\beta)} \tag{D.4}$$

Rewriting eq. (D.3)

$$= \left(\frac{1}{2\Delta\beta}\right)\left(\frac{1}{Z_\varrho}\right)\left[(\alpha^+)Z_H(\beta+\Delta\beta)-(\alpha^-)Z_H(\beta-\Delta\beta)\right] \tag{D.5}$$

$$= \left(\frac{1}{2\Delta\beta}\right)\left(\frac{1}{Z_\varrho}\right)\left[\int \mathrm{d}\mathbf{R}^P\,(\alpha^+)g\left(\mathbf{R},\beta+\Delta\beta\right)-(\alpha^-)g\left(\mathbf{R},\beta-\Delta\beta\right)\right] \tag{D.6}$$

$$= \left(\frac{1}{2\Delta\beta}\right)\left(\frac{1}{Z_\varrho}\right)\left[\int \mathrm{d}\mathbf{R}^P\,\varrho\left(\mathbf{R},\beta\right)\frac{(\alpha^+)g\left(\mathbf{R},\beta+\Delta\beta\right)-(\alpha^-)g\left(\mathbf{R},\beta-\Delta\beta\right)}{\varrho\left(\mathbf{R},\beta\right)}\right] \tag{D.7}$$

$$= \left(\frac{1}{2\Delta\beta}\right)\left\langle\frac{(\alpha^+)g\left(\mathbf{R},\beta+\Delta\beta\right)-(\alpha^-)g\left(\mathbf{R},\beta-\Delta\beta\right)}{\varrho\left(\mathbf{R},\beta\right)}\right\rangle_\varrho \tag{D.8}$$

$$= \left(\frac{1}{2\Delta\beta}\right)\left\langle\frac{(\alpha^+)g\left(\mathbf{R},\beta+\Delta\beta\right)}{\varrho\left(\mathbf{R},\beta\right)}\right\rangle_\varrho-\left(\frac{1}{2\Delta\beta}\right)\left\langle\frac{(\alpha^-)g\left(\mathbf{R},\beta-\Delta\beta\right)}{\varrho\left(\mathbf{R},\beta\right)}\right\rangle_\varrho \tag{D.9}$$

We define

$$Z_f^\pm=\left\langle\frac{(\alpha^\pm)g\left(\mathbf{R},\beta\pm\Delta\beta\right)}{\varrho\left(\mathbf{R},\beta\right)}\right\rangle_\varrho \tag{D.10}$$

Simplifying eq. (D.9)

$$\frac{\partial}{\partial\beta}Z_f \approx \left(\frac{Z_f^+-Z_f^-}{2\Delta\beta}\right) \tag{D.11}$$

Finally

$$U_H = U_f + U_\varrho \tag{D.12}$$

$$= \left(\frac{-1}{Z_f}\right) \frac{\partial}{\partial \beta} Z_f + U_\varrho \tag{D.13}$$

$$\approx \left(\frac{-1}{Z_f}\right) \left(\frac{Z_f^+ - Z_f^-}{2\Delta\beta}\right) + U_\varrho \tag{D.14}$$

## Appendix E: Heat capacity estimator

Where

$$C_v^f = \left(\frac{1}{k_B T^2}\right)\left[\left(\frac{1}{Z_f}\right)\frac{\partial^2}{\partial\beta^2}Z_f - (U_f)^2\right] \tag{E.1}$$

Evaluate the $\beta$ derivative using second order symmetric difference

$$\frac{\partial^2}{\partial\beta^2}Z_f \approx \left(\frac{1}{\Delta\beta^2}\right)\left[Z_f\left(\beta+\Delta\beta\right) - 2Z_f\left(\beta\right) + Z_f\left(\beta-\Delta\beta\right)\right] \tag{E.2}$$

Applying the same approach as the energy estimator gives us

$$\frac{\partial^2}{\partial\beta^2}Z_f \approx \left(\frac{1}{\Delta\beta^2}\right)\left(\frac{1}{Z_\varrho}\right)\int \mathrm{d}\mathbf{R}^P\,\varrho\left(\mathbf{R},\beta\right)\left[\frac{(\alpha^+)g\left(\mathbf{R},\beta+\Delta\beta\right) - 2g\left(\mathbf{R},\beta\right) + (\alpha^-)g\left(\mathbf{R},\beta-\Delta\beta\right)}{\varrho\left(\mathbf{R},\beta\right)}\right] \tag{E.3}$$

Which simplifies to

$$\frac{\partial^2}{\partial\beta^2}Z_f \approx \left(\frac{Z_f^+ - 2Z_f + Z_f^-}{\Delta\beta^2}\right) \tag{E.4}$$

Finally

$$\begin{aligned} C_v^H &= C_v^f + C_v^\varrho && \text{(E.5)}\\ &= \left(\frac{1}{k_B T^2}\right)\left[\left(\frac{1}{Z_f}\right)\frac{\partial^2}{\partial\beta^2}Z_f - (U_f)^2\right] + C_v^\varrho && \text{(E.6)}\\ &\approx \left(\frac{1}{k_B T^2}\right)\left[\left(\frac{1}{Z_f}\right)\left(\frac{Z_f^+ - 2Z_f + Z_f^-}{\Delta\beta^2}\right) - (U_f)^2\right] + C_v^\varrho && \text{(E.7)} \end{aligned}$$

## Appendix F: Jackknife estimators

For this derivation I attempt to use similar notation as in [27, p. 10] so that the reader may reference that document and gain a better understanding of the approach.

We define three expectation values:

$$\mu_Z \equiv \langle Z \rangle \qquad \mu_{\partial Z} \equiv \left\langle \frac{\partial Z(\beta)}{\partial \beta} \right\rangle \qquad \mu_{\partial^2 Z} \equiv \left\langle \frac{\partial^2 Z(\beta)}{\partial \beta^2} \right\rangle$$

We express the three desired quantities, ($Z$, $E$, $C_v$)

$$f^Z\left(\mu_Z\right) = \mu_Z\left(Z_\varrho\right) \tag{F.1}$$

$$f^E\left(\mu_{\partial Z}, \mu_Z\right) = \frac{-\mu_{\partial Z}}{\mu_Z} \tag{F.2}$$

$$f^{C_v}\left(\mu_{\partial^2 Z}, \mu_{\partial Z}, \mu_Z\right) = \frac{1}{k_B T^2}\left[\frac{\mu_{\partial^2 Z}}{\mu_Z} - \frac{\mu_{\partial Z}^2}{\mu_Z^2}\right] \tag{F.3}$$

The estimate of the *true* partition function $f^Z\left(\mu_Z\right)$ is clearly $f^Z\left(\overline{Z}\right)$, with error $\sqrt{\frac{\sigma^2}{N}}$. We need not use any statistical technique to obtain the standard error of the partition function. The energy $f^E$ and heat capacity $f^{C_v}$ are non-linear functions of averages and therefore require more care. Using the Jackknife approach detailed in [27, p.12 15] we can express the unbiased energy as

$$f^E\left(\mu_{\partial Z}, \mu_Z\right) = N\left\langle f(\overline{\partial Z}, \overline{Z})\right\rangle - (N-1)\left\langle \overline{f^{EJ}} \right\rangle + O\left(\frac{1}{N^2}\right) \tag{F.4}$$

$\left\langle \overline{f^{EJ}} \right\rangle$ is defined as $\frac{1}{N}\sum\limits_{i=1}^{N} f_i^{EJ}$ where

$$f_i^{EJ} = \left(\frac{-1}{2\Delta\beta}\right)\frac{\left(\frac{1}{N-1}\right)\sum\limits_{j\neq i}\delta_{\Delta\beta}\left[f\right]\left(\mathbf{R}_j, \beta, \beta'\right)}{\left(\frac{1}{N-1}\right)\sum\limits_{j\neq i} f\left(\mathbf{R}_j, \beta\right)} \tag{F.5}$$

Therefore the energy $f^E\left(\mu_{\partial Z}, \mu_Z\right)$ is

$$(N)\frac{\left\langle \delta_{\Delta\beta}\left[f\right]\left(\mathbf{R},\beta,\beta'\right)\right\rangle_{\varrho}}{\left\langle f\left(\mathbf{R},\beta\right)\right\rangle_{\varrho}} - \left(\frac{N-1}{N}\right)\sum_{i=1}^{N} f_i^{EJ} \tag{F.6}$$

The expanded form looks like this:

$$(N)\left(\frac{\sum\limits_{j=1}^{N}\left[\delta_{\Delta\beta}\left[f\right]\left(\mathbf{R}_j,\beta,\beta'\right)\right]}{\sum\limits_{j=1}^{N} f\left(\mathbf{R}_j,\beta\right)}\right) - \left(\frac{N-1}{N}\right)\sum_{i=1}^{N}\left(\frac{\sum\limits_{j\neq i}\delta_{\Delta\beta}\left[f\right]\left(\mathbf{R}_j,\beta,\beta'\right)}{\sum\limits_{j\neq i} f\left(\mathbf{R}_j,\beta\right)}\right)$$

Similarly we express the unbiased heat capacity estimator

$$f^{C_v}\left(\mu_{\partial^2 Z},\mu_{\partial Z},\mu_Z\right) = N\left\langle f(\overline{\partial^2 Z},\overline{\partial Z},\overline{Z})\right\rangle - (N-1)\left\langle \overline{f^{CJ}}\right\rangle + O\left(\frac{1}{N^2}\right) \tag{F.7}$$

$\left\langle \overline{f^{CJ}}\right\rangle$ is defined as $\frac{1}{N}\sum\limits_{i=1}^{N}\left(\frac{1}{k_B T^2}\right) f_i^{CJ}$ where

$$f_i^{CJ} = \left[\frac{\left(\frac{1}{N-1}\right)\sum\limits_{j\neq i}\delta_{\Delta\beta}^2\left[f\right]\left(\mathbf{R}_j,\beta,\beta'\right)}{\left(\frac{1}{N-1}\right)\sum\limits_{j\neq i} f\left(\mathbf{R}_j,\beta\right)} - \frac{\left(\frac{1}{N-1}\right)^2\left(\sum\limits_{j\neq i}\delta_{\Delta\beta}\left[f\right]\left(\mathbf{R}_j,\beta,\beta'\right)\right)^2}{\left(\frac{1}{N-1}\right)^2\left(\sum\limits_{j\neq i} f\left(\mathbf{R}_j,\beta\right)\right)^2}\right] \tag{F.8}$$

Therefore our heat capacity estimator $f^{C_v}\left(\mu_{\partial^2 Z},\mu_{\partial Z},\mu_Z\right)$ is

$$\left(\frac{N}{k_B T^2}\right)\left[\frac{\left\langle \delta_{\Delta\beta}^2\left[f\right]\left(\mathbf{R},\beta,\beta'\right)\right\rangle_{\varrho}}{\left\langle f\left(\mathbf{R},\beta\right)\right\rangle_{\varrho}} - \frac{\left\langle \delta_{\Delta\beta}\left[f\right]\left(\mathbf{R},\beta,\beta'\right)\right\rangle_{\varrho}^2}{\left\langle f\left(\mathbf{R},\beta\right)\right\rangle_{\varrho}^2}\right] - \left(\frac{N-1}{N k_B T^2}\right)\sum_{i=1}^{N} f_i^{CJ} \tag{F.9}$$

The expanded form looks like this:

$$\left(\frac{N}{k_B T^2}\right)\left[\frac{\sum_{j=1}^{N}\delta^2_{\Delta\beta}\left[f\right]\left(\mathbf{R}_j,\beta,\beta'\right)}{\sum_{j=1}^{N}f(\mathbf{R}_j,\beta)}-\frac{\left(\sum_{j=1}^{N}\delta_{\Delta\beta}\left[f\right]\left(\mathbf{R}_j,\beta,\beta'\right)\right)^2}{\left(\sum_{j=1}^{N}f(\mathbf{R}_j,\beta)\right)^2}\right]$$
$$-\left(\frac{N-1}{Nk_B T^2}\right)\sum_{i=1}^{N}\left[\frac{\sum_{j\neq i}\delta^2_{\Delta\beta}\left[f\right]\left(\mathbf{R}_j,\beta,\beta'\right)}{\sum_{j\neq i}f\left(\mathbf{R}_j,\beta\right)}-\frac{\left(\sum_{j\neq i}\delta_{\Delta\beta}\left[f\right]\left(\mathbf{R}_j,\beta,\beta'\right)\right)^2}{\left(\sum_{j\neq i}f\left(\mathbf{R}_j,\beta\right)\right)^2}\right] \tag{F.10}$$